



**GIRAMOS: Gemini Infrared Multi-Object Spectrograph**

# **MOAO System**

**Preliminary Design**

**Document Number: GIRAMOS.MOAO.DD.0016.B**

## **Approvers List**

Prepared by	Scott Chapman, Uriel Conod, Paolo Turri	Signature
	MOAO lead, MOAO Postdoc, MOAO Postdoc,	
Reviewed by	Firstname Lastname	Signature
	Title	
Reviewed by	Firstname Lastname	Signature
	Title	
Approved by	Firstname Lastname	Signature
	Title	

## **Revisions**

<b>Revision</b>	<b>Change Description</b>	<b>Date</b>
A	Initial Draft	2020-12-31
B	Final draft	2022-04-11

## Table of Contents

1	Introduction .....	1
1.1	Purpose .....	1
1.2	Scope .....	1
1.3	Applicable Documents .....	1
1.4	Reference Documents .....	1
1.5	Acronyms/Abbreviations .....	2
2	Design Overview .....	3
2.1	Optical Design Overview .....	4
2.1.1	General Description and Functional Overview .....	4
2.2	Mechanical Design Overview .....	7
2.2.1	MOAO Function .....	7
2.2.2	MOAO General Assembly .....	7
2.2.3	Subassembly Description and Design .....	8
2.2.3.1	Deformable Mirror (DM) .....	8
2.2.3.2	WFS Corrector-Fold Subassembly .....	10
2.2.3.3	WFS Camera Assembly .....	12
2.2.3.4	Figure Source .....	15
2.3	Electrical Design Overview .....	18
2.3.1	MOAO subsystem electrical components .....	18
2.3.2	Subsystem components control chain .....	19
2.3.2.1	DM .....	19
2.3.2.2	WFS .....	19
2.3.2.3	FS .....	19
2.3.2.4	RTC .....	19
2.4	System Modeling Overview .....	25
2.4.1	GNAO .....	25
2.4.2	GIRMOS MOAO .....	25
2.5	Design Trade-Off Summary .....	27
2.5.1	MOAO architecture (GLAO + MOAO) .....	27
2.5.2	MOAO reconstructor (POL vs residual slopes) .....	28
2.5.3	GLAO (mean slopes vs tomography) .....	29
2.5.4	MOAO System order .....	29
2.5.5	DM (see Appendix C) .....	30
2.5.5.1	Dead actuators .....	30
2.5.6	WFS camera (see Appendix D) .....	32
2.5.7	PSF reconstruction (Appendix E) .....	32
2.6	RTC considerations and design .....	32
2.7	Manufacturability Assessment .....	34
2.8	Risks Retirement Activities .....	34
2.8.1	MOAO Testbed .....	34
2.8.1.1	Principle of operation .....	34
2.8.1.2	Hardware .....	36
2.8.1.3	Tests & Results .....	37
2.8.2	REVOLT Open-Loop .....	42
2.8.2.1	REVOLT .....	42
2.8.2.2	OL-WFS .....	44

2.8.2.3	CU .....	45
2.8.2.4	CL .....	46
2.8.2.5	OL .....	46
2.8.2.6	RTC .....	47
2.8.2.7	Time Schedule .....	47
3	Analysis .....	49
3.1	Optical Analysis .....	49
3.2	Mechanical Analysis .....	49
3.2.1	Sensitivity Analysis .....	49
3.2.2	Analysis of the Deformable Mirror (DM) Deflection Under Varying Gravity Vector .....	49
3.3	Electrical Analysis .....	51
3.3.1	Components Power Consumption .....	51
3.3.1.1	DM .....	51
3.3.1.2	WFS .....	52
3.3.1.3	FS .....	52
3.3.1.4	RTC .....	52
3.3.2	MOAO Power Requirement Summary .....	53
3.4	Performances Analysis .....	53
3.4.1	Baseline performance .....	53
3.4.2	Atmospheric conditions .....	54
3.4.3	LGS Asterisms .....	56
3.4.3.1	5LGS .....	56
3.4.3.2	4LGS-A, 4LGS-B, 4LGS-C .....	58
3.4.3.3	4LGS-T .....	59
3.4.3.4	Results .....	59
3.4.4	NCPA .....	60
3.4.5	Error Budget .....	60
4	Manufacturing, Assembly, Integration and Tests (MAIT) .....	61
4.1	Manufacturing .....	61
4.2	Preliminary MAIT flowchart .....	61
4.3	Long Lead Items List .....	62
4.4	Preliminary Integration Plan .....	62
4.4.1	Tools .....	62
4.4.2	WFS Sub-assembly Offline Alignment (Prior to integration) .....	63
4.4.3	AOVU Sub-assembly Offline Alignment .....	66
4.4.4	WFS Path Alignment Steps .....	66
4.4.5	Real DM integration .....	67
4.5	Preliminary Quality/PA Plan .....	68
4.6	Handling and Test Equipment (H&T) .....	69
5	Future Phases .....	70
Appendix A	Folded Figure Source Design .....	72
Appendix B	GIRMOS WFS Path .....	73
Appendix C	MOAO DM trade study .....	74
Appendix D	MOAO WFS trade study .....	81
Appendix E	Real-time PSF estimation with GIRMOS .....	87

## Table of Figures

Figure 1: GIRMOS instrument concept.....	3
Figure 2: <i>Left</i> : Exploded view of the GIRMOS instrument, showing the position of the MOAO system. <i>Right</i> : Assembled view of the GIRMOS instrument. ....	4
Figure 3: MOAO and OSEL opto-mechanical layout. ....	4
Figure 4: <i>Left</i> : Sketch of major optical components and conjugate planes in GIRMOS. The ray traced is the on-axis chief ray. Different colored rays exiting the volume phase holographic grating indicate the different wavelengths of light being dispersed, from [AD-01]. <i>Right</i> : MOAO functional block diagram (1 arm) showing the interfaces (light and telemetry) with GNAO.....	5
Figure 5: OSEL-MOAO optical layout. In yellow and green are respectively the Figure Source and the WFS light paths which are, in addition to the DM, part of the MOAO subsystem. ....	5
Figure 6: Figure Source path optical layout.....	6
Figure 7: WFS path optical layout. ....	6
Figure 8: AOVU optical layout.....	7
Figure 9: MOAO Components (*Optical bench omitted for clarity. Items shown transparent are not part of the MOAO subsystem – shown for reference only) .....	8
Figure 10: Deformable Mirror (DM) Assembly.....	9
Figure 11: Deformable mirror (DM) assembly – exploded view. ....	9
Figure 12: WFS Corrector plate-fold subassembly. ....	10
Figure 13: WFS Corrector plate-fold subassembly exploded view. ....	11
Figure 14: WFS Field stop with spacers (blue). ....	11
Figure 15: WFS Camera assembly exploded view. ....	12
Figure 16: WFS Lens tube assembly. ....	13
Figure 17: Lens and rotation tube assembly. ....	13
Figure 18: Rotation tube assembly exploded view. ....	14
Figure 19: Collimator lens mount (LA similar). ....	14
Figure 20: Figure source interface assembly. ....	15
Figure 21: Figure source interface assembly exploded view.....	16
Figure 22: Figure source assembly. ....	16
Figure 23: Figure source assembly exploded view.....	17
Figure 24: Figure source fold mirror and collimator optic (Items shown in transparent are not part of the MOAO subsystem- shown for reference only.).....	18
Figure 25: DM control chain.....	19
Figure 26: WFS control chain.....	19
Figure 27: FS control chain.....	19
Figure 28: RTC computer. ....	20
Figure 29: MOAO electrical diagram overview. ....	21
Figure 30: MOAO electrical diagram 1. ....	22
Figure 31: MOAO electrical diagram 2. ....	23
Figure 32: MOAO electrical diagram 3. ....	24
Figure 33: a) Optical principle used to modelized the GIRMOS MOAO system. The light collected within the 2 arcmin FOV passes through the GNAO system where a first GLAO correction is performed, the GIRMOS object selection system will then direct the scientific light (in red) into the GIRMOS MOAO system where an additional AO correction in the science direction is achieved. b) Instantaneous wavefronts as well as the DM shape computed at the different stages of the instrument (seeing-limited, GNAO and GIRMOS). c) Typical integrated H-band PSF, seeing-limited, GLAO-corrected and GLAO+MOAO-corrected. The red square represents a 0.1 arcsecond spaxel.....	26

Figure 34: EE <sub>01</sub> map over the 2 arcmin FOV. Left: POL based tomographic reconstructor. Right: Residual slopes only based tomographic reconstructor and assuming 0 ground layer turbulences. ....	28
Figure 35: EE <sub>01</sub> difference map between the POL based reconstructor and the residual slopes only reconstructor assuming 0 turbulence at ground layer. ....	29
Figure 36: GIRMOS open-loop DM order impact, GNAO order is fixed to 20. ....	30
Figure 37: DM292 actuator map in shown light blue, green is the “active” actuators map for GIRMOS (17x17 actuators), the pupil (white) is not centered on the DM but shifted of one actuator pitch in x and y. Dead actuators are shown in yellow. <i>Left</i> : DM BAX471 in configuration 1 (3 dead actuators in the pupil). <i>Center</i> : DM BAX471 in configuration 2 (2 dead actuators in the pupil). <i>Right</i> : DM BAX515 (2 dead actuators in the pupil).....	30
Figure 38: Residual wavefront (left) after closing the loop with on the GLAO-like residual wavefront and the corresponding PSF’s Ensquared Energy profiles for different DM. <i>Top</i> : DM BAX471 in configuration 1 (3 dead actuators in the pupil). <i>Center</i> : DM BAX471 in configuration 2 (2 dead actuators in the pupil). <i>Bottom</i> : DM BAX515 (2 dead actuators in the pupil).....	31
Figure 39: Optical principle for the GIRMOS MOAO testbed. The top of the figure illustrates the optical and telemetry paths. ....	35
Figure 40: a) Optical layout of the GIRMOS MOAO testbed. b) The testbed fully integrated in the HAA AO lab. ...	36
Figure 41: Image of the testbench real time display. From left to right (following the light path): The SLM shape, the OL-WFS spots, the DM shape, the CL-WFS spots and the science camera’s PSF.....	36
Figure 42: Bench NCPA estimation (100nm RMS), NCPA corrected PSF (Strehl = 92%).....	38
Figure 43: Example of in and out of focus PSFs. These images are used to run the phase diversity algorithm allowing to compute the NCPA. ....	39
Figure 44: Different interaction matrices used on the bench. a) DM / CL-WFS interaction matrix using the figure source and the DM. b) GNAO-DM0 / OL-WFS interaction matrix ( $S_1$ ) using the science source and the SLM as GNAO-DM0. c) GNAO-DM0 / CL-WFS interaction matrix ( $S_2$ ) using the science source and the SLM as GNAO-DM0. d) The matrix (TF) used to transform the OL-WFS slopes into CL-WFS slopes in order to control the DM. This matrix is generated with $S_1$ and $S_2$ as $TF = S_2 * S_1^T * (S_1 * S_1^T)^{-1}$ .....	39
Figure 45: a) Testbed simulation showing the GLAO injected (cyan) and measured (yellow) wavefront error and the GLAO+SCAO residual wavefront (green). b) Testbed measurement showing the GLAO injected (cyan) and measured (yellow) wavefront error and the GLAO+SCAO residual wavefront (green).....	40
Figure 46: Testbed measurement showing the GLAO injected and measured wavefront error, the GLAO+SCAO residual wavefront and the open-loop residual wavefront. ....	40
Figure 47: Testbed measurement showing the OL wavefront error measured using the FS and the CL-WFS. The magenta curve represents the wavefront error between the DM shape and the expected shape as measured by the figure source WFS (CL-WFS).....	41
Figure 48: Testbed measurement showing the OL wavefront error measured using the FS and the CL-WFS. The magenta curve represents the wavefront error between the DM shape and the expected shape as measured by the figure source WFS (CL-WFS). We manually injected some significant go-to-errors on the DM to test the FS closed-loop. ....	41
Figure 49: Optical design of REVOLT (CL mode).....	43
Figure 50: Optical design of the REVOLT CL-WFS. ....	43
Figure 51: Diagram of the light path in REVOLT.....	44
Figure 52: Simulation of the SNR of one spot in one frame of the OL-WFS, ....	45
Figure 53: Optical design of the REVOLT CU. ....	46
Figure 54: Pixel map of the SLM for a tilted wavefront. The vertical stripes inside the pupil are wrapped with a frequency of $2\pi$ radians to produce the tilt. ....	47
Figure 55: Conceptual model of DM assembly for FEA. ....	50
Figure 56: FEA results for DM assembly (gravity vector perpendicular to mirror face).....	50
Figure 57: Power consumption of the ALPAO DM468. ....	52
Figure 58: Expected mirror deformations from simulation. ....	52

Figure 59: H-band $EE_{0.1}$ ( <i>top</i> ) and SR maps ( <i>bottom</i> ). <i>Left</i> : GLAO mode with baseline parameters. <i>Right</i> : GLAO+MOAO mode with baseline parameters. ....	54
Figure 60: <i>Left</i> : Values of $EE_{0.1}$ and SR averaged over the FOR. <i>Right</i> : Ratio of the GIRMOS FOR where the requirement is reached for both $EE_{0.1} = 52\%$ and $SR = 22\%$ . ....	55
Figure 61: <i>Left</i> : Surface where $EE_{0.1} = 52\%$ for different $r_0$ values translated at zenith (color code). <i>Right</i> : Surface where $SR = 22\%$ for different $r_0$ values (color code). ....	55
Figure 62: GLAO+MOAO residual wavefront error in nm RMS for different $r_0$ (colors).....	56
Figure 63: Science (black), LGS (green, blue) and TT stars (magenta) positions within the GIRMOS FoV. <i>Left</i> : 5LGS configuration. <i>Center</i> : 4LGS-A, 4LGS-B and 4LGS-C configuration. <i>Right</i> : 4LGS-T configuration. ....	56
Figure 64: EE in 0.1" ( <i>left</i> ) and SR ( <i>right</i> ) performances in H-band for the 5LGS configuration.....	57
Figure 65: EE in 0.1" ( <i>left</i> ) and SR ( <i>right</i> ) performances in H-band for the 4LGS configuration, top line is for 4LGS-A, middle is 4LGS-B and bottom is 4LGS-C. ....	58
Figure 66: EE in 0.1" ( <i>left</i> ) and SR ( <i>right</i> ) contours corresponding to 57%EE and 27%SR in black and to 60%EE and 30%SR in blue. The line style is for the 3 different 4LGS configurations (A, B and C). ....	59
Figure 67: EE in 0.1" and SR (black) and Peak to Valley (blue) values over the 2 arcmin FoV for different 4LGS radial distance (4LGS-A, B, C).....	59
Figure 68: $EE_{0.1}$ (blue) and SR (red) for different NCPAs (insert) amplitudes, in H-band. ....	60
Figure 69: MOAO MAIT Flowchart. ....	61
Figure 70: OSEL-MOAO MAIT Flowchart. ....	62
Figure 71: Alignments tool required for MOAO. ....	63
Figure 72: A RAVEN cone enables interchangeability between Faro arm, Alignment Telescope and Point-Source Microscope.....	63
Figure 73: WFS assembly as designed for RAVEN (same concept than MOAO WFS). ....	64
Figure 74: Alignment source tool use for the internal alignment of the WFS assembly.....	64
Figure 75: AOVU path optical layout. with position of cones for alignment.....	66
Figure 76: The real DM must be shifted by half an actuator pitch (i.e., 0.75mm) in X and Y w.r.t. the optical axis in order to put an actuator on-axis and have 17 actuators across the beam. ....	68
Figure 77: ALPAO DM292 compliance list from the test report delivered for the first DM procurement on March 14, 2022.....	69
Figure 78: The AO schedule relative to other subsystems. ....	71
Figure 79: The MOAO budget in future phases from CDR to commissioning. ....	71
Figure 80: GIRMOS focal plane ensquared energy within 0.1" in function of AO system Order. From GIRMOS preliminary simulations presented in Chapman et al. 2018 [RD-07]. ....	75
Figure 81: Histogram of GIRMOS open loop PV DM deformations recorded from simulations given in wavefront space, which is the one generally used by DM manufacturers. ....	76
Figure 82: ALPAO off-the-shelf DM characteristics (datasheet link: pdf). ....	77
Figure 83: CILAS references for astronomy (datasheet link: pdf). ....	78
Figure 84: SPHERE Shack-Hartmann WFS image, we can distinguish the influence function of the SPHERE DM (made by CILAS with piezoelectric technology) dead actuators. ....	78
Figure 85: BOSTON off-the-shelf DM characteristics (datasheet link: pdf) ....	79
Figure 86: Cumulative distribution photons from WFS spots as a function of field radius for $r_0=10$ cm. ....	81
Figure 87: <i>Left</i> : Transmission of the system including the Ixon 860 camera QE. <i>Right</i> : Subaperture SNR per frame for different object I magnitude. The colors represent different frame rate. ....	83
Figure 88: <i>Left</i> : Transmission of the system including the OCAM2K camera QE. <i>Right</i> : Subaperture SNR per frame for different object I magnitude. The colors represent different frame rate. ....	83
Figure 89: <i>Left</i> : Transmission of the system including the Zyla 5.5 camera QE. <i>Right</i> : Subaperture SNR per frame for different object I magnitude. The colors represent different frame rate. ....	84

Figure 90: Left: Transmission of the system including the C-BLUE camera QE. Right: Subaperture SNR per frame for different object I magnitude. The colors represent different frame rate. ....	84
Figure 91: Left: Transmission of the system including the Zyla 4.2+ camera QE. Right: Subaperture SNR per frame for different object I magnitude. The colors represent different frame rate. ....	85
Figure 92: Left: Transmission of the system including the Marana 4.2 camera QE. Right: Subaperture SNR per frame for different object I magnitude. The colors represent different frame rate. ....	85

## Table of Tables

Table 1: System parameters (Gemini, GNAO, GIRMOS). ....	26
Table 2: Pixel scale and sampling measurement with tip. ....	37
Table 3: Pixel scale and sampling measurement with tilt. ....	38
Table 4: Characteristics of the C-BLUE ONE detector. ....	43
Table 5: MOAO Components mechanical sensitivity. ....	49
Table 6: Summary of the MOAO power budget. ....	53
Table 7: Reported GLAO-MOAO performance over the 2' FOV in H-band (1.65 $\mu$ m), assuming median seeing conditions at Mauna Kea and 30° zenith angle (1.5 Airmass). ....	60
Table 8: Ixon 860 specifications. ....	82
Table 9: OCAM2K specifications. ....	83
Table 10: Zyla 5.5 specifications. ....	83
Table 11: C-BLUE specifications. ....	84
Table 12: Zyla 4.2+ specifications. ....	84
Table 13: Marana 4.2 specifications. ....	85

# 1 Introduction

## 1.1 Purpose

Body text here

## 1.2 Scope

This document describes the design of the MOAO system only. It does not include specifications of interfaces with other GIRMOS subsystems. These are detailed in the GIRMOS Interface Control Documents (ICDs). Calibration, Acceptance and verification are discussed in the MOAO Integration and Test Plan (RD-13).

## 1.3 Applicable Documents

Applicable Documents are those documents containing information that is considered binding in the context of this document. Unless otherwise specified, the latest version of the Applicable Document shall be used. In case of conflict between an Applicable Document and this document, this document shall take precedent.

AD	Document #	Title
[AD-01]	GIRMOS.SYS.RS.0002	GIRMOS Instrument Requirements Document
[AD-02]	GIRMOS.SYS.0005	External Interface Definition Document
[AD-03]	GIRMOS.SYS.RS.0003	GIRMOS Design Guidelines
[AD-04]	GIRMOS.MOAO.RS.0001.B	MOAO Level 2 Requirements
[AD-05]	GIRMOS.MOAO.ICD.XXXX	MOAO to OSEL ICD
[AD-06]	GIRMOS.MOAO.ICD.XXXX	MOAO to ISTR ICD
[AD-07]	GIRMOS.OSEL.DD.XXXX.A	OSEL Design Document
[AD-08]	GIRMOS.MOAO.DD.XXXX.A	MOAO RTC design document

## 1.4 Reference Documents

Reference documents are those documents that are included for information purposes only. They may provide additional background or context, but are non-binding in the context of this document.

RD	Document #	Title
[RD-01]	Correia et al. (2015)	Spatio-angular minimum-variance tomographic controller for multi-object adaptive-optics systems
[RD-02]	Conan & Correia (2014)	Object-oriented Matlab adaptive optics toolbox
[RD-03]	Andersen et al. (2012)	Performance Modeling for the RAVEN Multi-Object Adaptive Optics Demonstrator
[RD-04]	Sivo et al. (2020)	GNAO: an MCAO facility for Gemini North
[RD-05]	Lamb et al. (2014)	
[RD-06]	Sivanandam et al. (2018)	Gemini Infrared Multi-Object Spectrograph: Instrument Overview.
[RD-07]	Chapman et al. (2018)	The multi-object adaptive optics system for the GIRMOS spectrograph on Gemini-South.
[RD-08]	Jackson et al. (2019)	AO Performance model and error budget for GIRMOS
[RD-09]	Morel et al. (2016)	
[RD-10]	Genron et al. (2016)	
[RD-11]	Morris et al. (2018)	
[RD-12]	Puech et al. (2005)	Deformable mirrors for the FALCON concept.



[RD-13]	Kellerer et al. (2012)	Deformable mirrors for open-loop adaptive optics.
[RD-14]	Bitenc et al. (2014)	Assessing the stability of an ALPAO deformable mirror for feed-forward operation.
[RD-15]	Le Bouquin et al. (2018)	Characterisation of ALPAO deformable mirrors for the NAOMI VLT Auxiliary Telescopes Adaptive Optics.

## 1.5 Acronyms/Abbreviations

<b>Acronym</b>	<b>Meaning</b>
ADC	Atmospheric Dispersion Compensator
AO	Adaptive Optics
AOVU	Adaptive Optics Verification Unit
CL	Closed-Loop
COTS	Commercially available Off-The-Shelf
DM	Deformable Mirror
FOV	Field of View
FWHM	Full Width at Half Maximum
FS	Figure Source
GIRMOS	Gemini Infra-Red Multi-Object Spectrograph
GLAO	Ground Layer Adaptive Optics
GNAO	Gemini North Adaptive Optics
IFU	Integral Field Unit
MCAO	Multi Conjugate Adaptive Optics
MOAO	Multi Object Adaptive Optics
NA	Numerical Aperture
OL	Open-Loop
OSEL	Object Selection subsystem
POL	Pseudo-Open Loop
PSF	Point Spread Function
PV	Peak-to-Valley
QSA	Quasi-Static Aberration
RTC	Real Time Controller
SCAO	Single Conjugate Adaptive Optics
WFE	Wave Front Error
WFS	Wave Front Sensor

## 2 Design Overview

GIRMOS is an AO-assisted near-infrared multi-object integral-field spectrometer. As shown in Figure 1, it is designed to take advantage of the new Gemini North Adaptive Optics System (GNAO), and is closely integrated with that system. It has four independent spectroscopic channels, each using a pick-off arm to access science targets within a 2-arcmin diameter field of view (FOV), and an optical train that includes multi-object adaptive optics (MOAO) and an image slicer integral field unit (IFU). GIRMOS also has an imaging camera that can operate simultaneously with spectroscopic observations. Both the spectroscopic and imaging channels employ infrared detectors and cover the wavelength range 0.9-2.4  $\mu\text{m}$ .

The MOAO system is a subsystem within the GIRMOS. As illustrated in Figure 2 and Figure 4, it is located inside the Object Selection (OSEL) subsystem. The MOAO subsystem is made of 5 different components (see, Figure 4 *right*): a deformable mirror (DM 17x17 actuators), a figure source (FS), a wavefront sensor (WFS Shack-Hartmann 16x16 subapertures), a real time controller (RTC) and a performance verification unit (AOVU) which will also be used as a telescope reference for alignment of all the GIRMOS subsystem together. In order to control MOAO system, the GIRMOS Real Time Controller (RTC) will receive telemetry from GNAO's RTC as illustrated in Figure 1 and Figure 4 *right*.

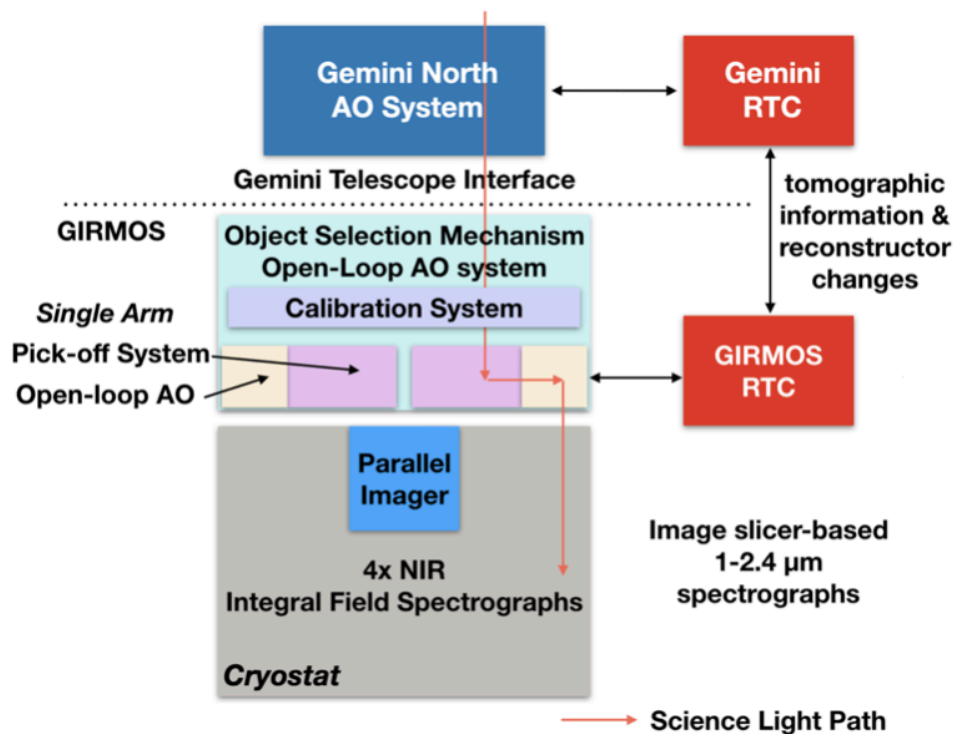
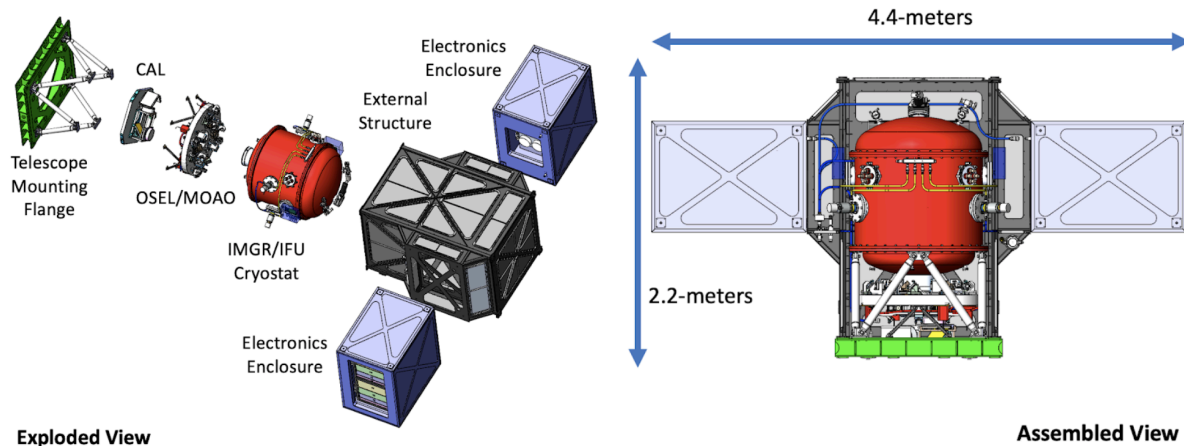
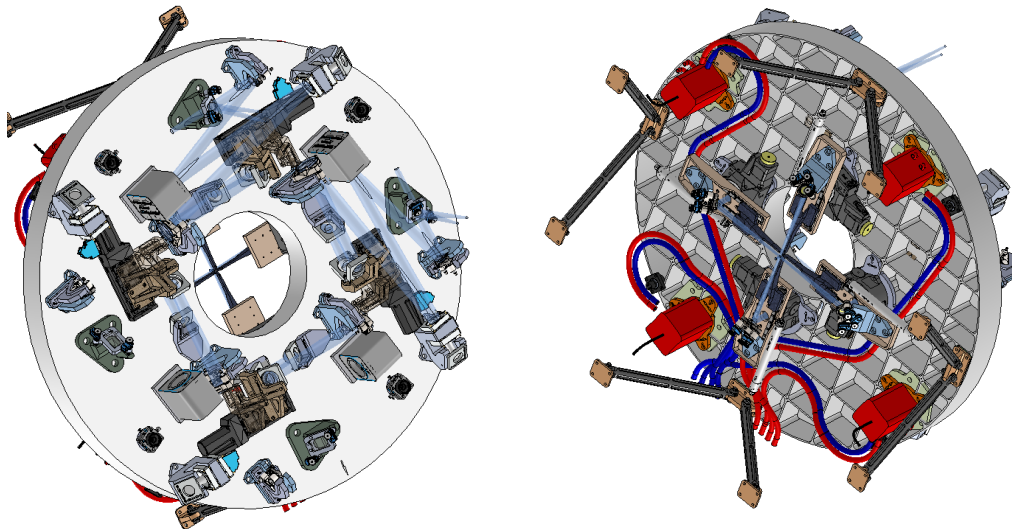


Figure 1: GIRMOS instrument concept.



**Figure 2: Left: Exploded view of the GIRMOS instrument, showing the position of the MOAO system. Right: Assembled view of the GIRMOS instrument.**



**Figure 3: MOAO and OSEL opto-mechanical layout.**

## 2.1 Optical Design Overview

Although the Multi-Object Adaptive Optics (MOAO) components make up a separate subsystem, due to its deep integration in to the OSEL subsystem and the symbiotic nature of the two, the Optical design Overview details can be found in the OSEL design document [AD-07].

### 2.1.1 General Description and Functional Overview

The optical component and the functional block diagram of MOAO can be found in Figure 4.

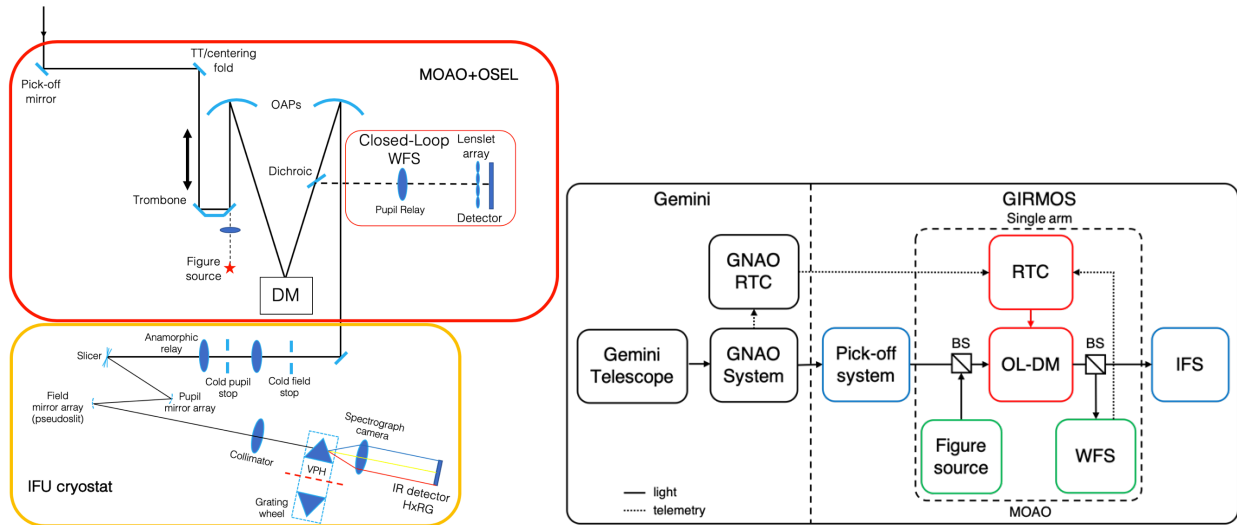


**Figure 4: Left: Sketch of major optical components and conjugate planes in GIRMOS. The ray traced is the on-axis chief ray. Different colored rays exiting the volume phase holographic grating indicate the different wavelengths of light being dispersed, from [AD-01]. Right: MOAO functional block diagram (1 arm) showing the interfaces (light and telemetry) with GNAO.**

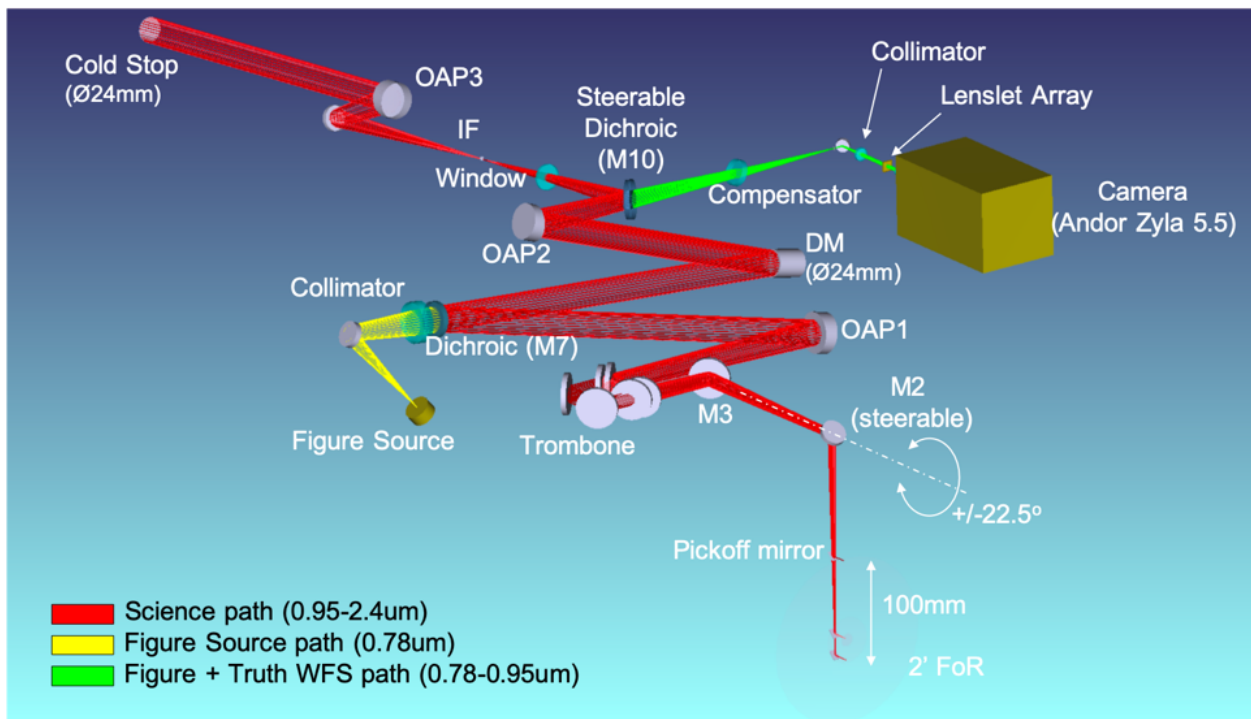


**Figure 5: OSEL-MOAO optical layout. In yellow and green are respectively the Figure Source and the WFS light paths which are, in addition to the DM, part of the MOAO subsystem.**

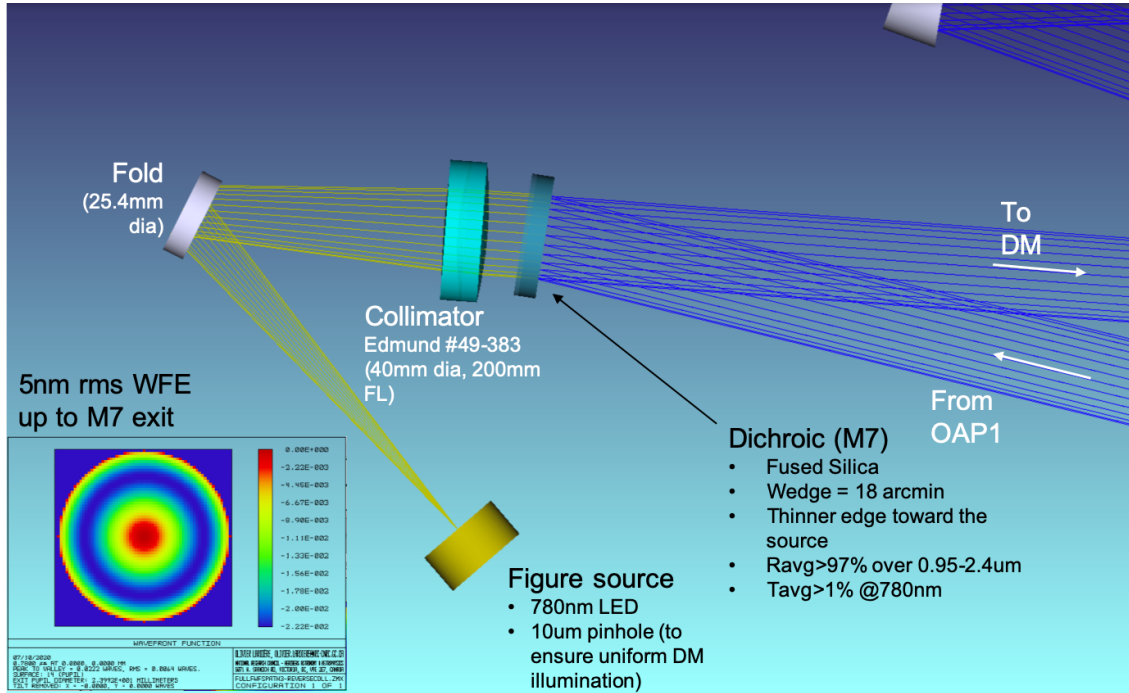


Figure 6: Figure Source path optical layout.

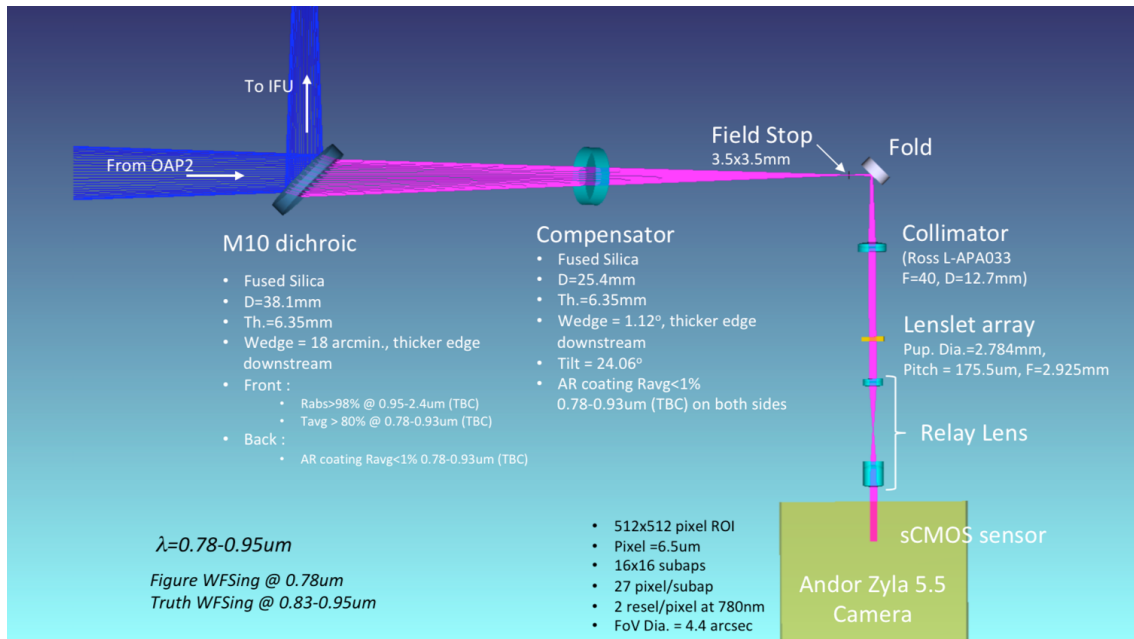
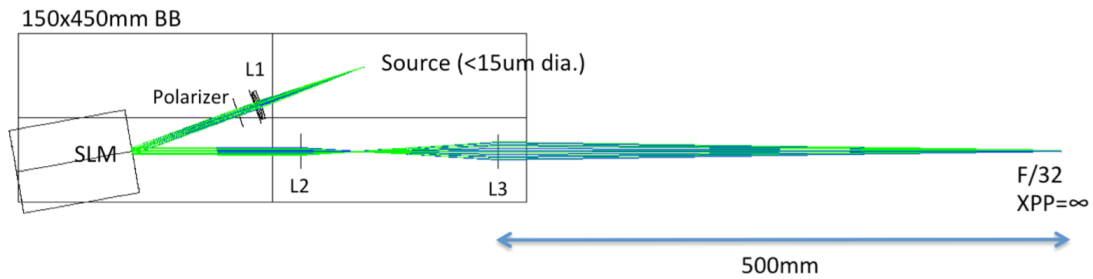


Figure 7: WFS path optical layout.



**Figure 8: AOVU optical layout.**

## 2.2 Mechanical Design Overview

Although the Multi-Object Adaptive Optics (MOAO) components make up a separate subsystem, due to its deep integration in to the OSEL subsystem and the symbiotic nature of the two, the MOAO mechanical design has been performed by NRC-HAA and is presented in this section. The brief overview of the MOAO subsystem given below explains how the two systems interact and the basis for the mechanical design but is not meant to cover all the nuances of the MOAO. For more in-depth description of the MOAO, please see the documentation of that specific subsystem.

### 2.2.1 MOAO Function

The MOAO subsystem provides feedback to the optical system which allows the DM to be reshaped in real-time to correct aberrations in the wavefront. As described in the OSEL section, light exiting the DM passes through the OSEL optical train to the final optic in the path at which point a portion of the light passes through the M10 dichroic mirror, continuing on into the MOAO wavefront sensor (WFS) path. The wavefront form is analyzed by the wavefront sensor (WFS) camera and correction is fed back to the DM, which is located near the middle of the relay stream of the OSEL subsystem.

The MOAO subsystem also includes a figure (light) source which allows calibration of the DM surface.

### 2.2.2 MOAO General Assembly

The MOAO subsystem consists of four components per channel, to be mounted on the OSEL optical bench, and integrated into the OSEL optical path (RELAY). Note there is (4) channels total to be arrayed rotationally around the centre of the optical bench. The components consist of:

1. The deformable mirror – located between fold mirror (M7) and the second off-axis parabola (OAP2).
2. The Wavefront Sensor corrector plate –fold mirror mount – located between the last fold mirror (M10) and the Wavefront Sensor camera (WFS camera), consisting of corrector plate, field stop and fold mirror.
3. The Wavefront Sensor (WFS) camera assembly, located at the end of the WFS path, consisting of the fore-optics (collimator, lenslet array, r and two relay lenses), WFS camera, fore-optics mounting structure and WFS interface stage.
4. The figure source – located “behind” the second fold mirror (M7), consisting of a light source and a collimating lens and cell.

The locations of these (4) components are per Figure 9 below.

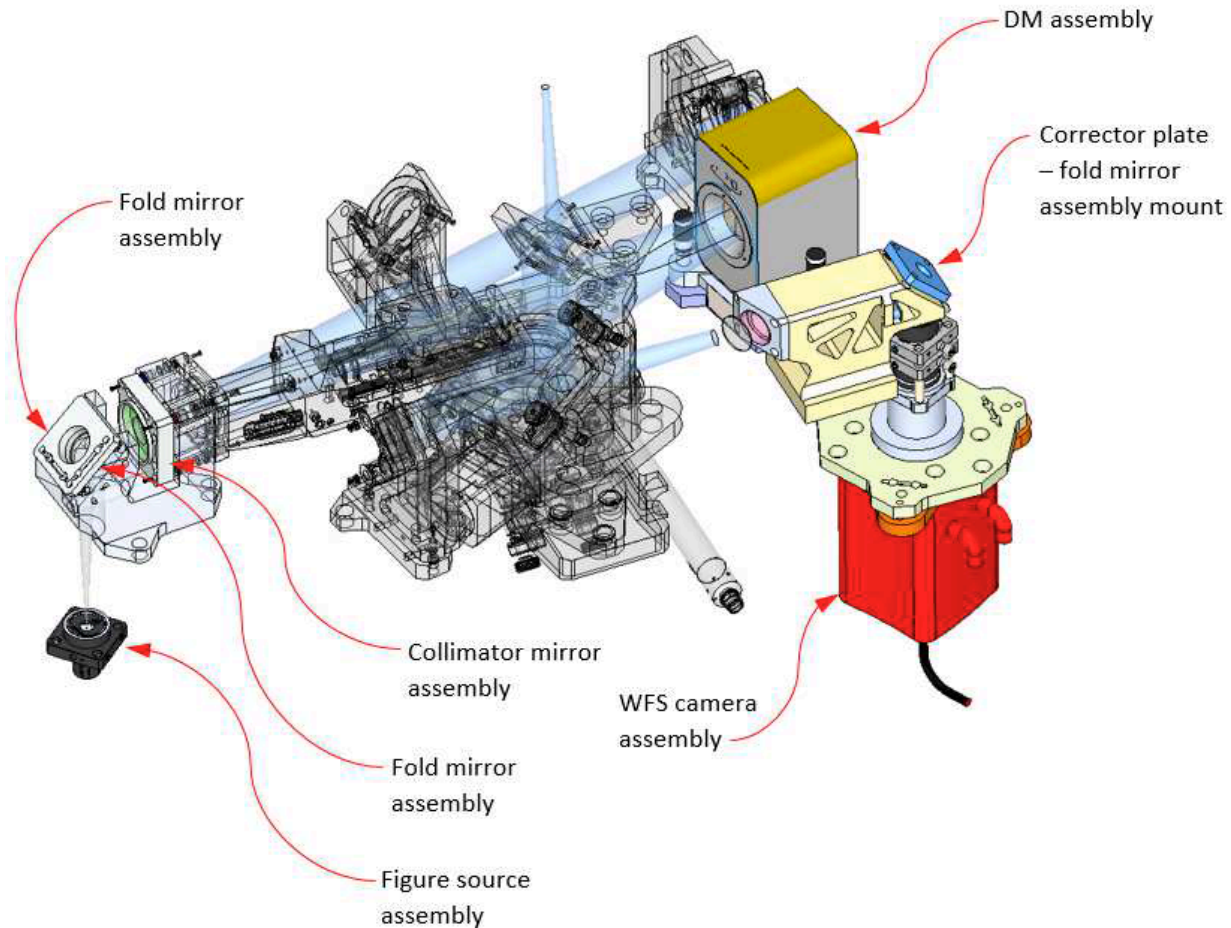


**Figure 9: MOAO Components (\*Optical bench omitted for clarity. Items shown transparent are not part of the MOAO subsystem – shown for reference only)**

## 2.2.3 Subassembly Description and Design

### 2.2.3.1 Deformable Mirror (DM)

The deformable mirror (DM), an “ALPAO” model no. DM-29215001AA, resides near the centre of the OSEL REALY path, between M7 and OAP2, as shown in Figure 5. The only supplied mounting feature of the DM is a set of (4) threaded mounting holes and 2 alignment pin slots in the bottom face of the DM housing. The DM is mounted to a tip-tilt plate which is attached to a base plate via tension springs and dowels. Similar to the mount plate for the OSEL pickoff arm rotation stage in OSEL, the tip-tilt plate uses 3 micrometer nudgers which interface to three inserts located in a base plate, allowing rotation of the DM body about the local ‘X and ‘Y’ axes as well as vertical translation about the local ‘Y’ axis. Rotation adjustment of the DM about a vertical (local ‘Y’ axis) and translation about the local ‘X-Y’ plane is performed using micrometer nudgers mounted on the optical bench. As with the OSEL pickoff arm rotation stage, once aligned the tip-tilt plate can be secured in place using lock plates.

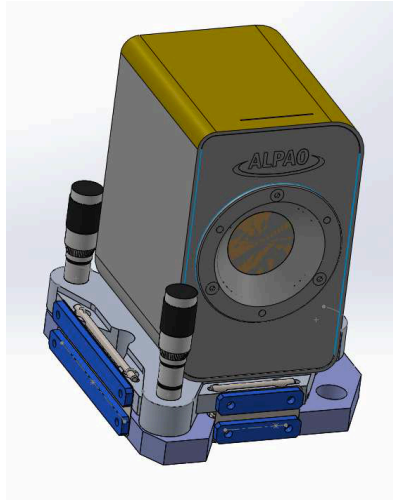


**Figure 10: Deformable Mirror (DM) Assembly.**

The mounting plate is affixed to the optical bench using bolts through eccentric washers in oversized mounting holes. The clearance holes allow 3mm of translation in the local 'X-Y' plane and TBD rotation about the local 'Y' axis which are controlled through micrometer nudgers. Once aligned, the mount is locked in place by tightening the bolts.

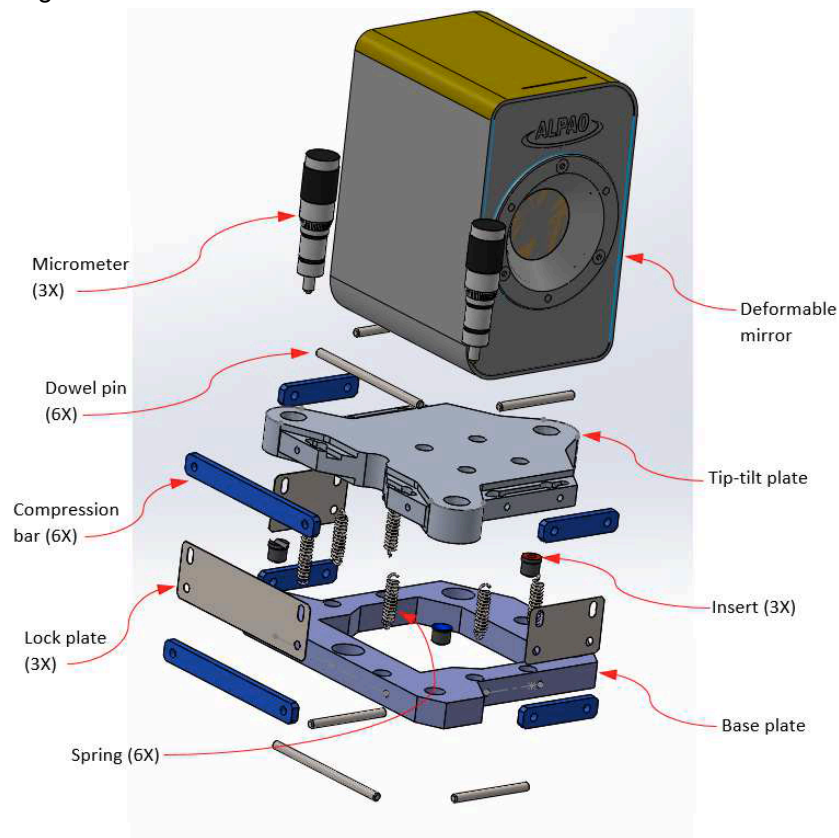


**Figure 11: Deformable mirror (DM) assembly – exploded view.**



### 2.2.3.2 WFS Corrector-Fold Subassembly

Light that passes through the M10 dichroic mirror continues along the WFS optical path. This path consists of a corrector plate, field stop and fold mirror which redirects the light into the WFS camera subassembly. Due to space limitations, the WFS camera and fore-optics are located vertically, with the WFS camera proper located below the optical bench. The corrector plate, field stop and fold mirror components mount to the WFS corrector-fold subassembly which consists of an aluminum base structure with provision for mounting of the corrector plate, field stop and fold mirror (Figure 12).

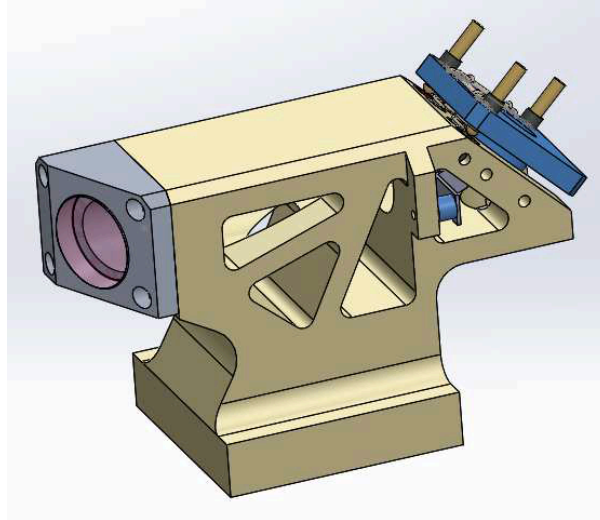


**Figure 12: WFS Corrector plate-fold subassembly.**

The base structure bolted to the optical bench through eccentric washers in oversized (TBD) mounting holes. The clearance holes allow TBD m of translation in the local 'X-Y' plane and TBD rotation about the local 'Y' axis which are controlled through micrometer nudgers. These degrees of freedom allow the base structure to be initially aligned such that the beam passing through the corrector plate travels concentrically through the horizontal bore in the base structure, through the field stop and onto the fold mirror. Once aligned, the mount is locked in place by tightening the bolts.

The optics in the subassembly are constrained as follows:

- The system focus is 237.5mm from the M10
- The fold mirror must not be coincident with the focus
- The fold mirror must be upstream of the WFS fore-optics collimator
- The field stop is to be positioned 10mm in front of the fold mirror vertex
- The field stop is to have a square aperture 3.5mm on a side

The corrector plate is a 1-inch (25.4mm) diameter flat optic (Edmunds optics no. 37-689) which realigns the beam after it is shifted while passing through the M10 dichroic. The corrector plate retaining cell, which is bolted to the front face of the base structure is machined to a predesignated angle conducive with the required tilt angle of the optic. The optic is bonded to the cell using XX (or retained with a 3-tab ring?). Although it has been determined the cell can be machine to tolerances I below those required for the corrector plate tilt angle, there is also the possibility of static adjustment (shimming) if required.

The rear face of the base structure is machined to provide the basic 45-degree angle required by the fold mirror to redirect the beam downward through the optical bench and into the WFS camera subassembly. The fold mirror is a 1/2-inch (12.7mm) diameter mirror (spec?) which is mounted in a custom rectangular

cell. The cell is adjustable in 3 DoF to allow steering of the beam such that it is parallel to the optical axis of the WFS fore-optics. The adjustment (rotation about the local 'X' and 'Y' axes and translation about the local 'Z' axis) is effected by (3) Newport fine thread adjusting screws (Newport **AS-XX**) seated in semi-kinematic mounts located in the base structure and retained by tension springs and dowel pins. As with the flat optics in the OSEL subsystem, the fold mirror is retained by a 3-tab compression ring with the tabs positioned across from 3 raised "buttons" on the base of the cell to reduce possible distortion of the optic.

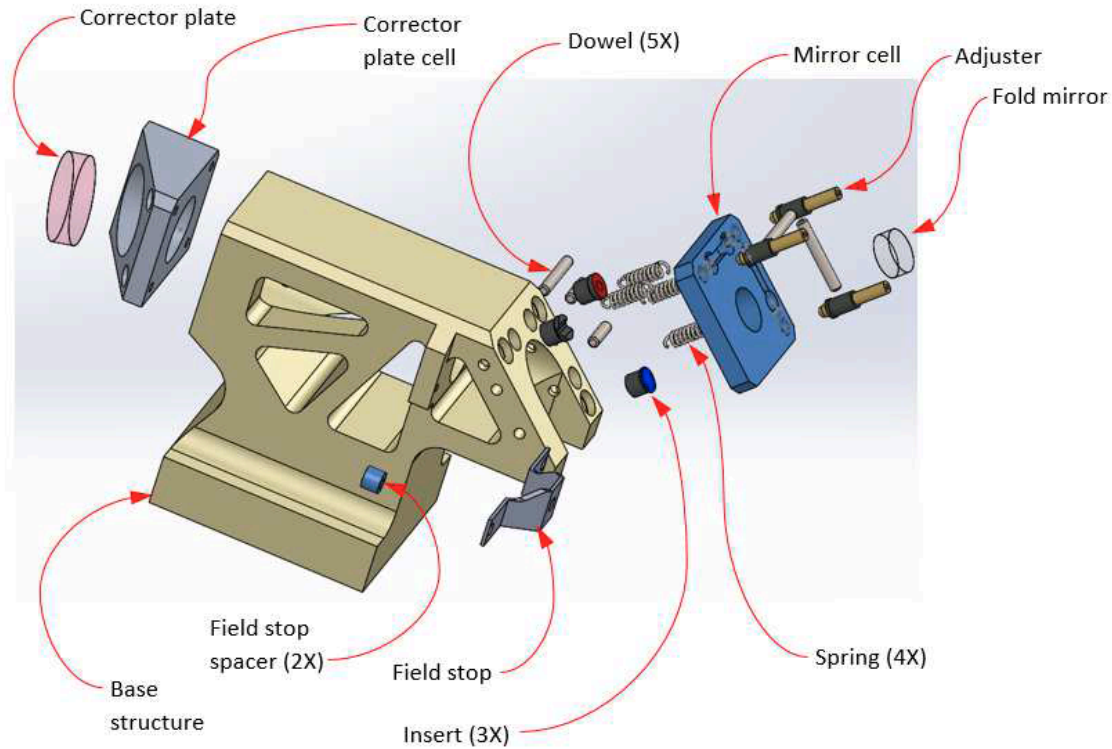


**Figure 13: WFS Corrector plate-fold subassembly exploded view.**

The field stop is formed from sheet aluminum with the aperture machined (EDM) into the sheet before forming. The field stop is bolted to the base structure using machined spacers to ensure the proper axial positioning with respect to the fold mirror and has sufficient clearance in the mounting holes to allow adjustment in the local 'X-Y' plane (Figure 14). Then field stop is not installed until after the fold mirror is aligned to the system and then is aligned to the beam passing from the corrector plate to the fold mirror.

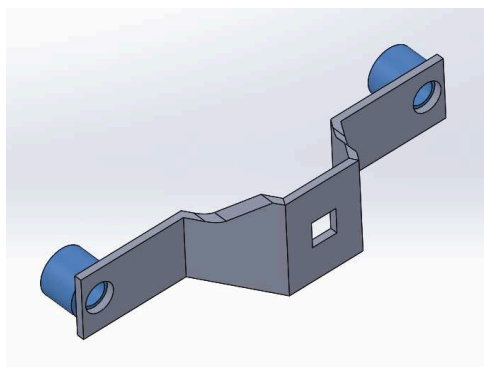


**Figure 14: WFS Field stop with spacers (blue).**

### 2.2.3.3 WFS Camera Assembly

The WFS camera subassembly consist of the Andor Zyla (5.5) camera, a set of fore optics which include a collimating lens, lenslet array and (2) relay doublets and an interface stage. Figure 15 below illustrates the (4) main subcomponents of the WFS camera assembly.

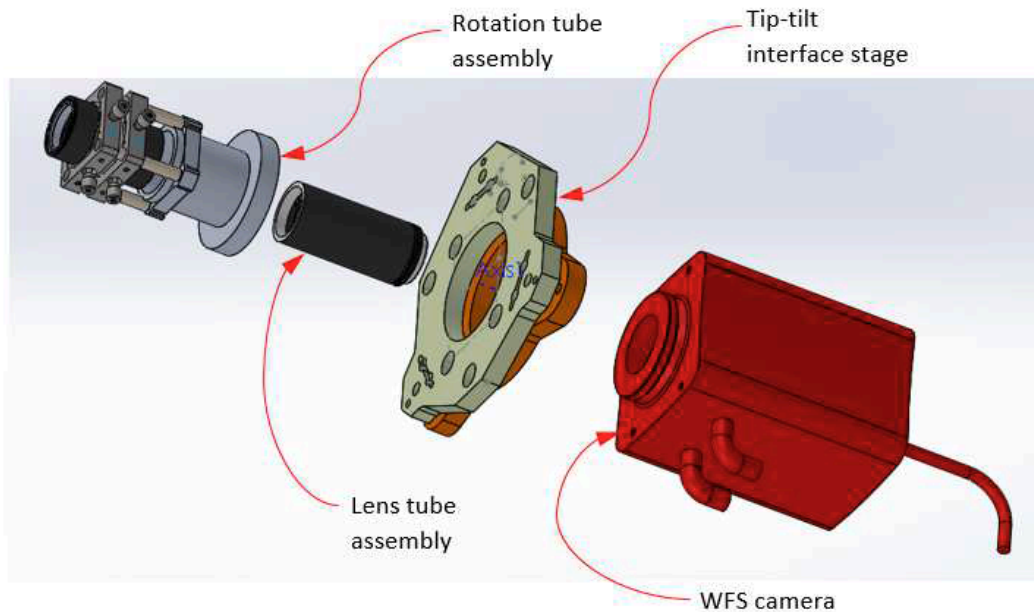


**Figure 15: WFS Camera assembly exploded view.**

The WFS camera is mounted to the **tip-tilt interface stage** via existing mounting holes in cameras (M4 x 4 - Figure 15) The interface stage allows the camera to be adjusted via micrometer “nudgers” in tip and tilt (rotation about the ‘X’ and ‘Y’ axes assuming the ‘X-Y’ plane parallel to the optical bench) and focus (direction perpendicular to the optical bench - Figure 9). The base plate of the interface stage is bolted into a dedicated recess in lower face of the optical bench through eccentric washers in oversized mounting holes. The clearance holes allow **TBD** of translation in the **local ‘X-Y’** plane and **TBD** rotation about the **local ‘Y’** axis which are controlled through micrometer nudgers. Once adjusted the stage can be locked in place using the bench mounting bolts for the base plate and lock plate system between the **motion/translation** plate and base plate.

The WFS camera is produced with a standard ‘C’ mount thread (1” dia. x 32 TPI) machined into camera housing just ahead of the detector plane. Threaded into mount is an internally threaded standard lens tube. The lens tube houses (2) adaptors (ThorLabs AD9T) which retain the (2) 9mm diameter relay lens doublets. Note that, while the doublets are both the same OD, they are optically dissimilar – see the optical design section (**Section 2.1**) for further information on relay lenses.

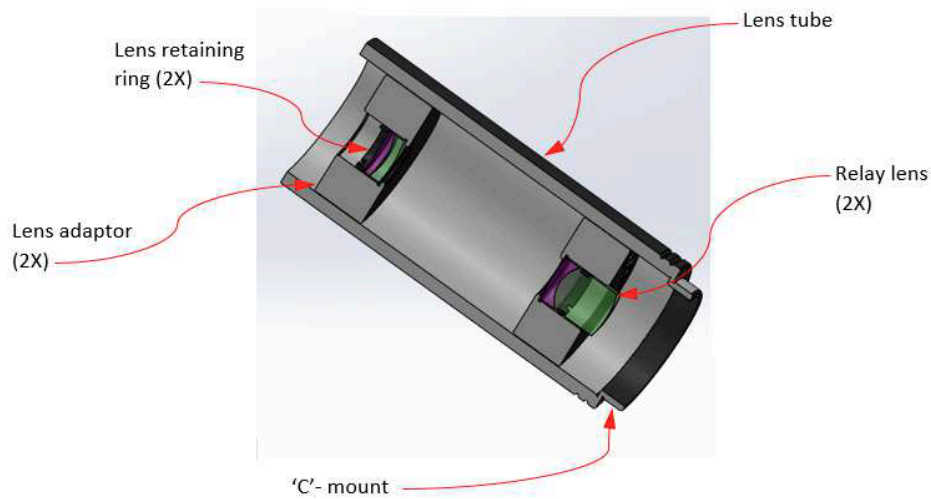


**Figure 16: WFS Lens tube assembly.**

The adaptors are internally threaded (M9.5 x 0.5) and have an integral seat at one end (7.9mm clear aperture). The doublet is therefore landed in the seat and retained axially at the opposite end with the supplied retaining ring (Figure 16). Retaining rings threaded into the lens tube are used to position the adaptors (and hence the doublets) axially. The required accuracy for concentricity and angularity of the two doublet is within that provided by mounting in the adaptors. As the doublets are axisymmetric, there is no consideration for rotation or “clocking” of these optics. [Appendix ‘B’](#) provides information on the position of the relay lenses.

A rotation tube assembly attached to the WFS camera [motion/translation](#) plate by a clamp ring. The rotation tube ID is approximately 2mm larger than the lens tube OD such that the lens tube assembly is housed inside but not attached to the rotation tube (Figure 17).

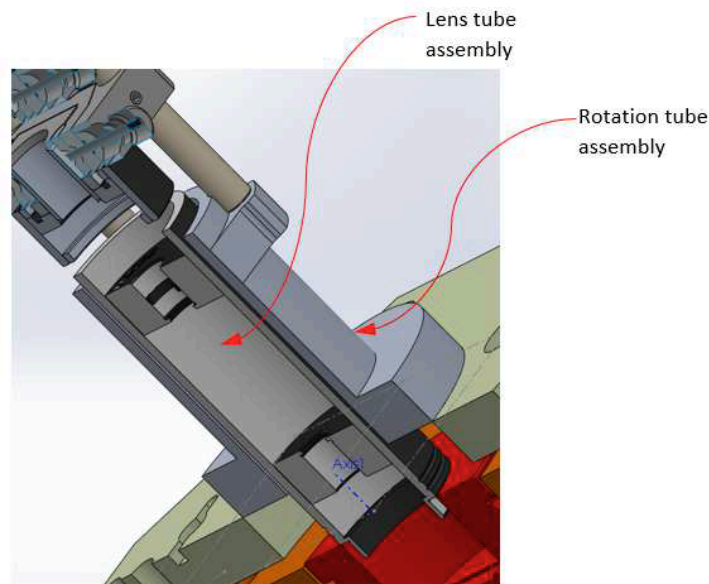


**Figure 17: Lens and rotation tube assembly.**

The lenslet array and collimating lenses are both mounted in cells set in 'X-Y' cage flexures (ThorLabs CP1XY) which allow adjustability of each optic in the local 'X-Y' plane. The previously discussed rotation tube is terminated with a rectangular flange with (4) threaded holes (M4) set on the same pitch as the mounting holes for the cage flexures. (4) Cage support posts threaded into the mounting flange of the rotation tube then allow attachment of the (2) cage flexures to the rotation tube (Figure 18 below).

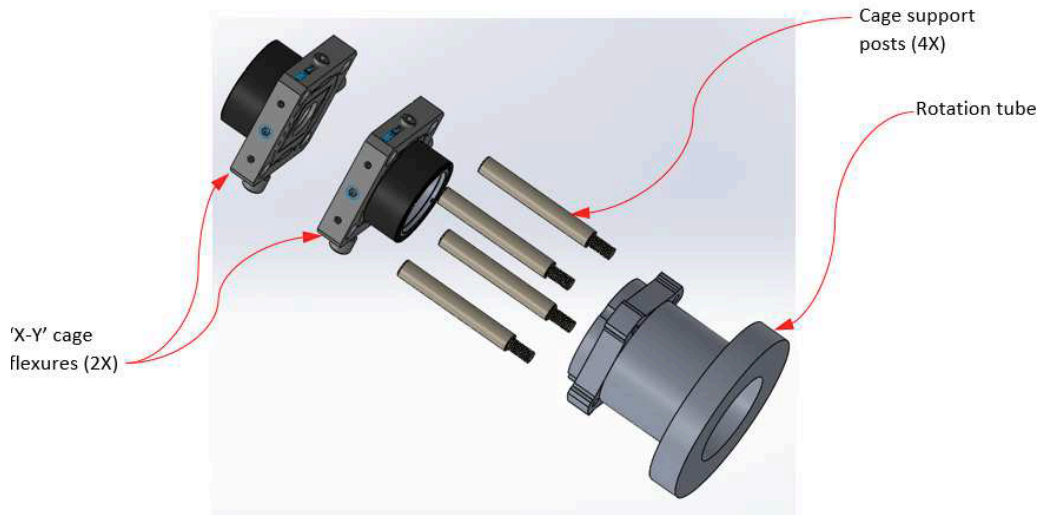


**Figure 18: Rotation tube assembly exploded view.**

A mounting collar (ThorLabs no. SM05T2) is threaded into each cage flexure and subsequently attached to lens tube (Thorlabs no. SM1M05) by way of an adaptor ring (Thorlabs no. SM1A6) per Figure 19.

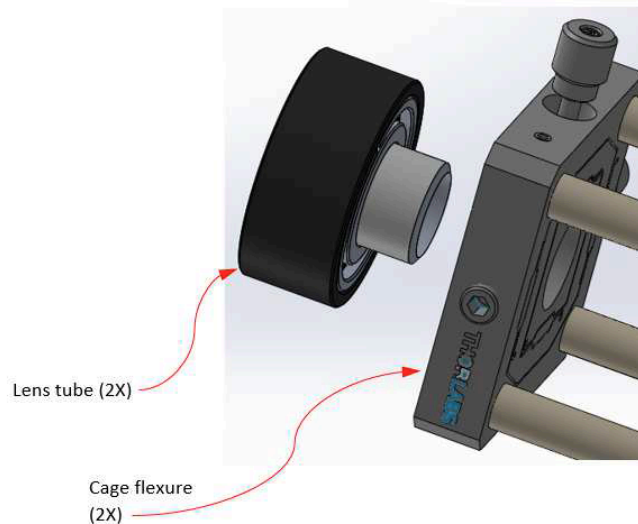


**Figure 19: Collimator lens mount (LA similar).**

In the case of the collimating lens, stock (ThorLabs TBD) adaptor rings are used to mount the optic in the lens tube. The lenslet array is mounted to a square substrate and will therefore be bonded to a circular glass substrate before being mounted to the lens tube. Once the optics are mounted in the flexure cages, axial positioning is effected by sliding them along the support posts, and once located, the flexure cages

are locked to the support posts using the integral set screws. (See [Appendix 'B'](#) for information on positioning of the collimating lens and lenslet array). It is noted that although the collimating lens does not require clocking, it uses the same flexure cage and mounting scheme as the lenslet array and thus is also set on the rotation tube.

With the rotation tube assembly completed and the clamp ring loosened, the tube is free to rotate about the optical axis thereby allowing the lenslet array to be clocked with respect to the columns and rows on the WFS camera detector. Once rotational alignment is achieved, the clamp ring is re-secured.

In order to minimize heat dissipation to the optical space, the WFS camera is cooled via glycol. The glycol is supplied by the telescope at the Cassegrain panel and routed to the instrument structure connector panel. From there dedicated supply and return lines run to a distribution manifold mounted on the lower surface of the OSEL optical bench. The manifold distributes the coolant to each camera via 1/4" nominal supply lines, and collects the return coolant again at the manifold to be returned to the telescope supply system. Connection to the instrument structure's connector panel is made through (TBD) "quick connect" hardware.

#### 2.2.3.4 Figure Source

The figure source directs a beam of light onto the DM which is then directed through the OSEL M10 dichroic mirror to the WFS camera. The figure source light is used in conjunction with the WFS camera to calibrate (flatten) the DM reflective surface. The figure source is made up of two physically separate subassemblies, specifically the light source and the fold/collimating elements (Figure 9).

Due to space constraints on the upper surface of the optical bench, the actual figure sources mounted on the lower face of the bench and use a fold mirror to redirect the light to the face of the DM. The figure source consists of the components shown in Figure 24 (and schematic in Appendix A).

In order to mount the figure source assembly to the optical bench a custom interface assembly is used. The interface assembly (Figure 20) consists of a tip-tilt-stage attached to a base plate by springs and dowels. (3) Newport fine thread adjusting screws (Newport AS-XX) set in the tip-tilt and seated in semi-kinematic mounts inserted into the base plate allow 3 DoF adjustability (rotation about the local 'X' and 'Y' axes and translation about the local 'Z' axis) to the figure source. The base plate also incorporated oversized holes to allow translational adjustment of the figure source assembly (in the local 'X-Z' plane).

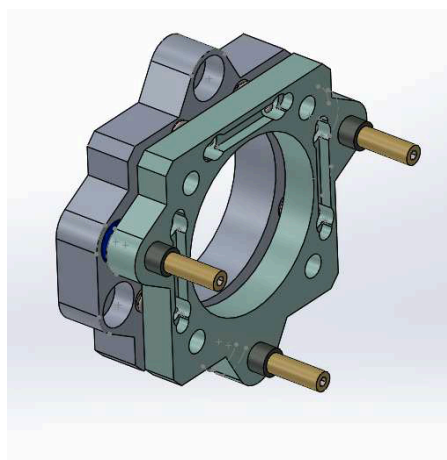


**Figure 20: Figure source interface assembly.**

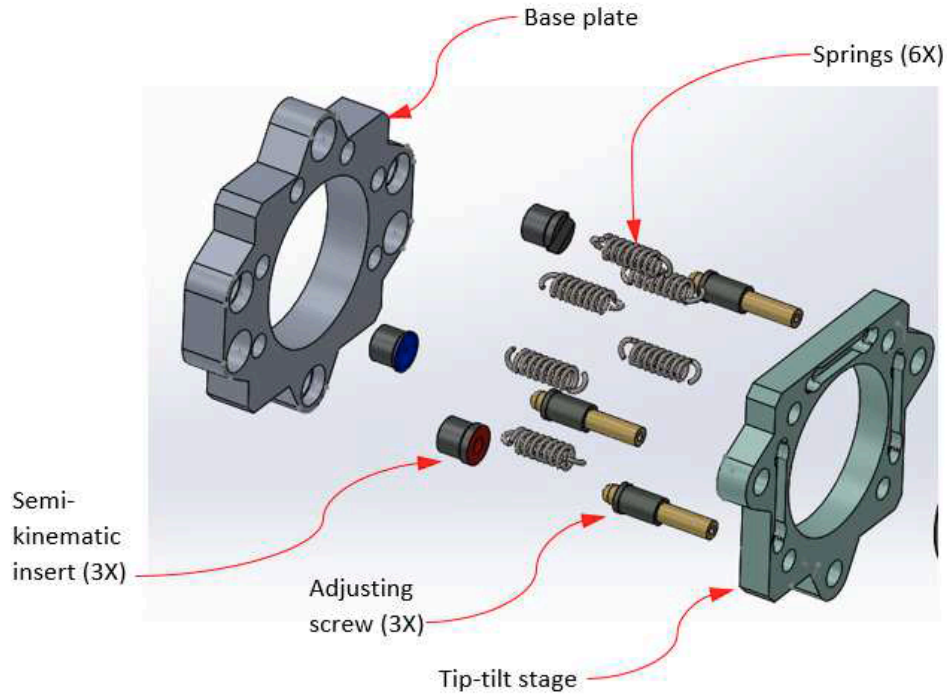


**Figure 21: Figure source interface assembly exploded view.**

The figure source proper is a ThorLabs LED780L LED light mounted in a ThorLabs LEDMT1E resistor module which threads into a ThorLabs SMS1 LED threaded mount. This assembly is subsequently threaded into the lower surface of a ThorLabs CP33M cage plate. A shortened Lens tube (0370-EOW) is also mounted to the upper surface of the same cage plate and is used to mount the precision 10  $\mu\text{m}$  pinhole (ThorLabs P10D).



**Figure 22: Figure source assembly.**



**Figure 23: Figure source assembly exploded view.**

After exiting the pinhole, the figure source beam passes through the optical bench and is then redirected by a fold mirror and through a collimating lens, both mounted on the M7 [base structure](#), on its way to the reflective surface of the DM. (Figure 9). (Note the M7 assembly is described in the OSEL section of this document.)

The fold mirror consists of a 1" (25.4mm) diameter flat mirror mounted in a rectangular cell. The is mounted on (3) Newport fine thread adjusting screws (Newport AS-XX) seated in semikinematic mounts inserted into the M7 [base structure](#) to effect 3 DoF adjustability (rotation about the local 'X' and 'Y' axes and translation about the local 'Z' axis) to the optic cell (Figure 24). The optic is mounted in the cell via a 3-tab compression ring with the tabs positioned across from 3 lands on the base of the cell to reduce possible distortion of the optic (similar to the M3 mounting scheme in the GIRMOS OSEL).



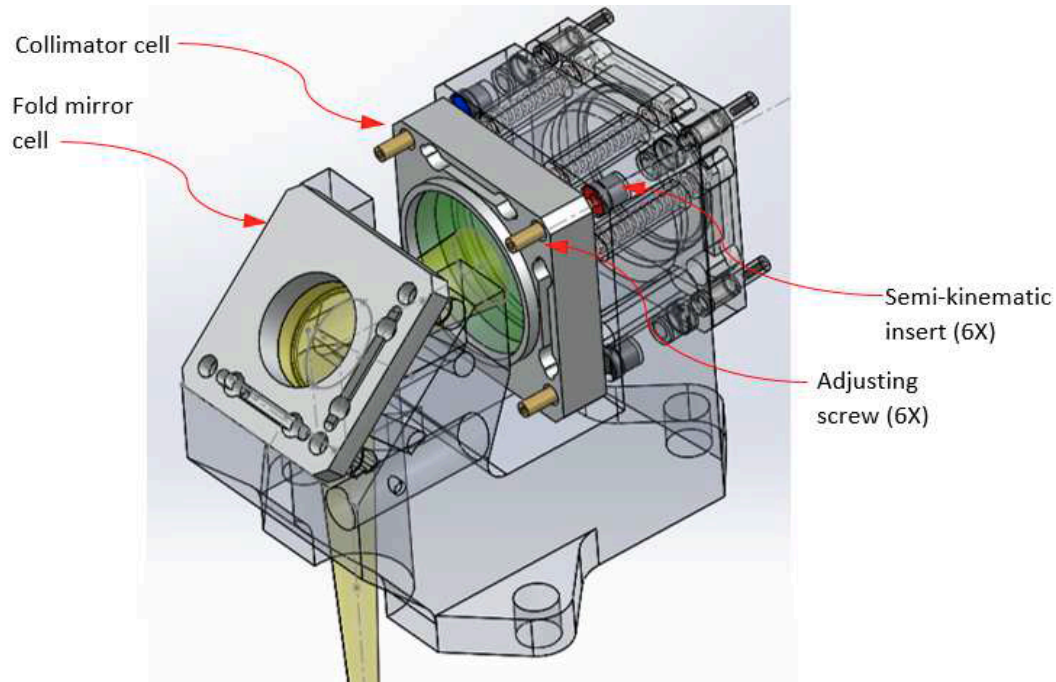


**Figure 24: Figure source fold mirror and collimator optic (Items shown in transparent are not part of the MOAO subsystem- shown for reference only.)**

From the fold mirror the diverging beam passes through a collimating lens also mounted in the M7 base structure. The collimator lens is a **double – check** (Edmund #49-383 - 40mm dia, 200mm FL) mounted in a custom square cell. Similar to flat mirror mounts, the cell is adjustable in 3 DoF to allow tip/tilt/focus adjustment of the collimator. The adjustment (rotation about the local 'X' and 'Y' axes and translation about the local 'Z' axis) is effected by (3) Newport fine thread adjusting screws (Newport **AS-XX**) seated in semi-kinematic mounts located in the M7base structure and is retained by the same tension springs used to retain the M7 dichroic mirror.

The collimator optic is retained by a 3-tab compression ring with the tabs positioned across from 3 lands machined to be conformal to the curved surface of the collimator lens to reduce possible distortion of the optic.

For reference, the aluminum base structure for M7 is bolted to the optical bench through eccentric washers in oversized mounting holes. The clearance holes allow 3mm of translation in the local 'X-Y' plane and TBD rotation about the local 'Y' axis which are controlled through micrometer nudgers. Once aligned, the mount is locked in place by tightening the bolts.

## 2.3 Electrical Design Overview

### 2.3.1 MOAO subsystem electrical components

The MOAO subsystem is divided into 5 products that comprise assemblies or groups of components that provide basic functions, with interfaces minimized:

- **Deformable mirror (DM): 4x ALPAO DM292**

- **Wavefront sensor (WFS): 4x Andor Zyla 5.5**
- **Figure source (FS): 4x LED**
- **Real Time Controller (RTC): 1x RAX QS12-22E2**
- *Adaptive Optics Verification Unit (AOVU): 1x*

For a precise description of each components we refer to [AD-03, section 4.0]. Note that the last component (AOVU) is not discussed in this section.

## 2.3.2 Subsystem components control chain

### 2.3.2.1 DM

The DM is connected to a drive Electronics box which is itself connected to the RTC via a PCIe board. For each of the 4 DMs an electronic box and a PCIe board is required. Note that ALPAO is exploring the possibility of combining two electronics boxes in one, in order to minimize the space in the cabinet.

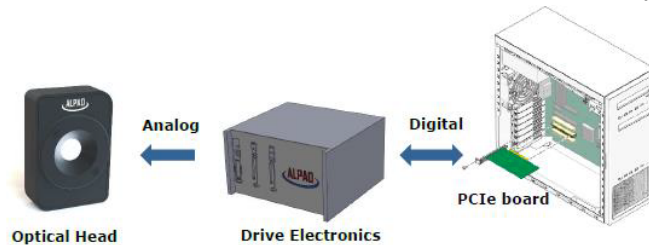


**Figure 25: DM control chain.**

### 2.3.2.2 WFS

Each of the 4 WFSs cameras are connected to the RTC via a camera link PCIe boards.

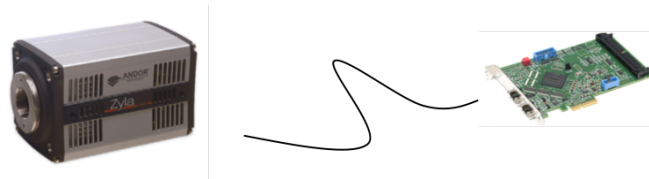


**Figure 26: WFS control chain.**

### 2.3.2.3 FS

The FS doesn't need to be connected to the RTC but only to the instrument software subsystem (TBC). The baseline is to control the 4 FS from the same electronic controller which is itself connected to the instrument workstation via USB.



**Figure 27: FS control chain.**

### 2.3.2.4 RTC

The RTC is connected the instrument workstation (TBC). The RTC is also connected to the DM electronic boxes and the WFS cameras via PCIe boards.



**Figure 28: RTC computer.**

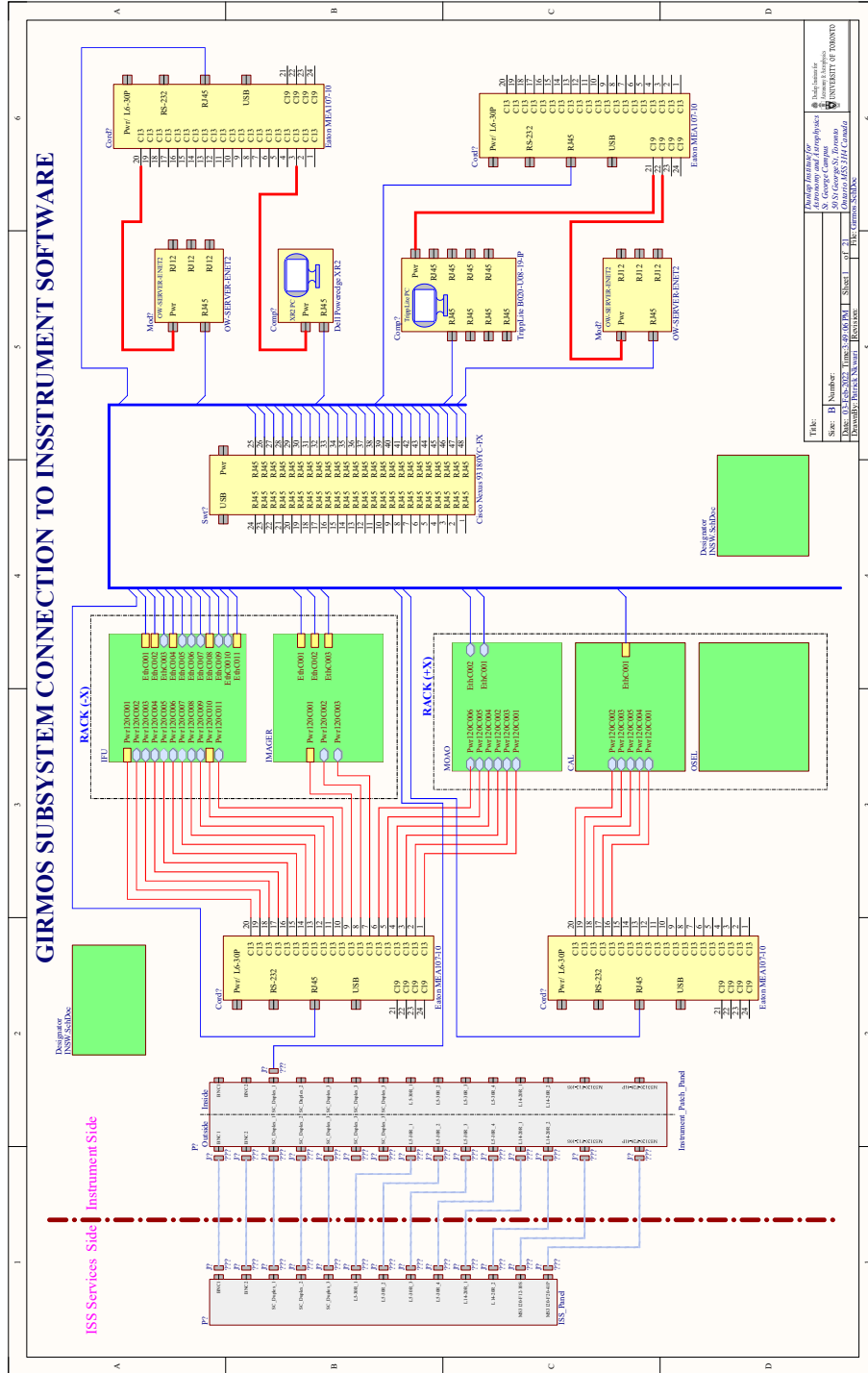


Figure 29: MOAO electrical diagram overview.

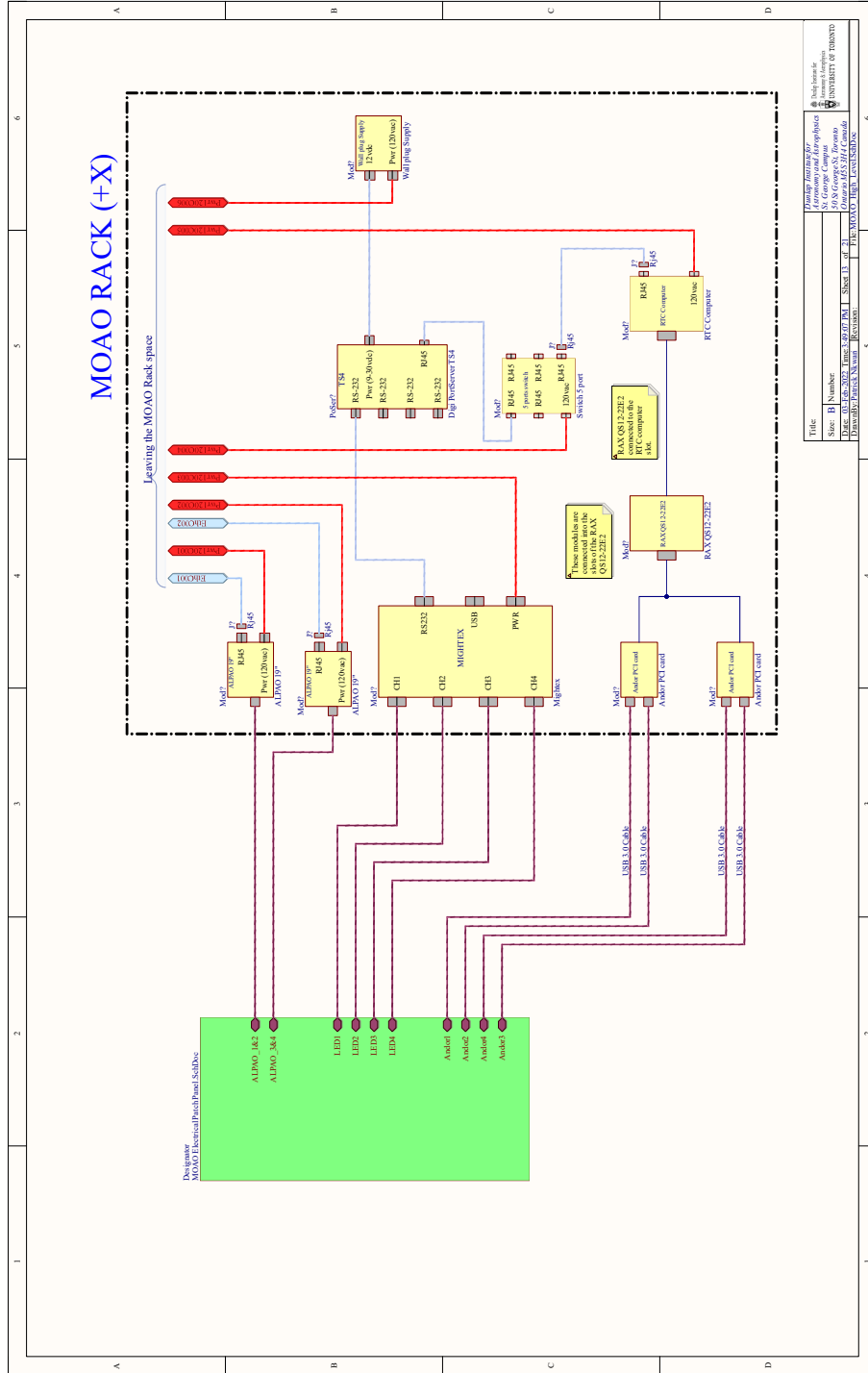


Figure 30: MOAO electrical diagram 1.

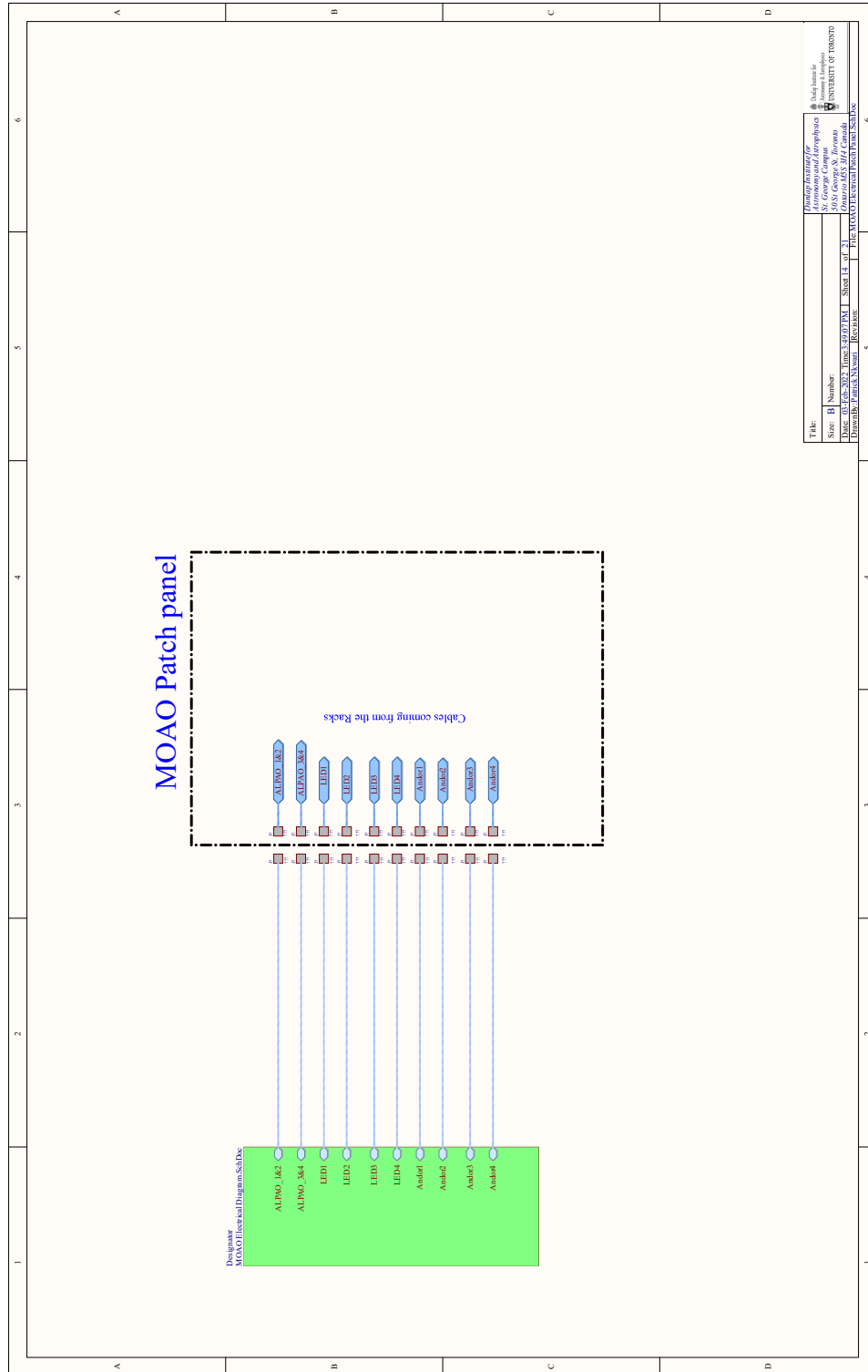


Figure 31: MOAO electrical diagram 2.

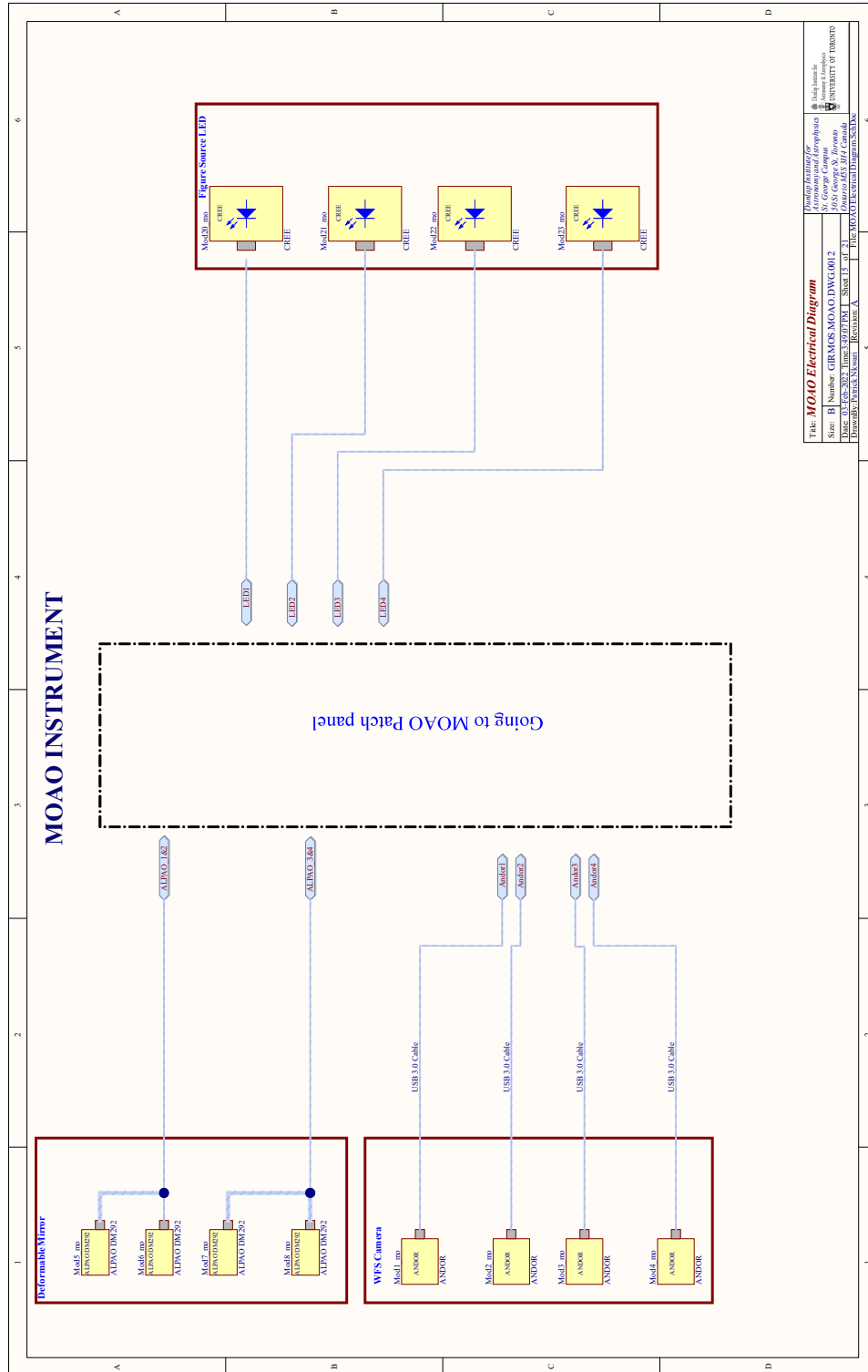


Figure 32: MOAO electrical diagram 3.

## 2.4 System Modeling Overview

Several instruments have explored MOAO technique and based on recent developments in the field and modeling explorations, the GIRMOS MOAO system proposes to use a high-order DM (17x17) controlled in open-loop. To compute the DM commands, the telemetry from the GNAO WFSs need to be processed. To mitigate the open-loop errors, the MOAO correction will be executed on top of a GLAO correction done by GNAO. In addition, a figure source and a Shack-Hartmann wavefront sensor (16x16) will be used to lock the DM shape. Finally, the interface with GNAO will simplify the architecture and relax the requirements on the MOAO wavefront correction.

### 2.4.1 GNAO

The design of GNAO being not completely frozen, we assumed for this work a baseline set of parameters to simulate this system. The main observing mode for GNAO is GLAO, using 4 LGSs and 3 NGSs located in the 2 arcmin FOR, see Figure 1 a). Each LGS has a magnitude of  $V=13$  and is coupled to a Shack-Hartmann WFS with 20x20 subapertures with 8x8 pixels per lenslet. The NGSs ( $V=17$ ) are coupled to a wavefront sensor consisting of an imager (Shack-Hartmann WFS with one lenslet) with 20x20 pixels. For both NGS and LGS WFSs we assumed a read-out-noise of  $0.5e^-$  rms. The GLAO correction is performed by a DM with 21x21 actuators. A summary of the GNAO parameters is shown in Table 1.

### 2.4.2 GIRMOS MOAO

The goal of the MOAO system is to provide an additional wavefront correction on top of the residual wavefront delivered by GNAO. We present the preliminary design of the GIRMOS MOAO [reference]. The MOAO system is relatively simple and consists in 4 essential components: an open-loop DM (OL-DM, 17x17 actuators), a figure source, a closed-loop WFS (CL-WFS, 16x16 subapertures) and a real-time controller (RTC). The CL-WFS can be used for different purposes: measure the shape of the DM using the figure source to correct the go-to errors, use the CL-WFS as a truth WFS to help calibrate or measure the MOAO performance in the case of compact and bright science targets. The RTC will process the different WFSs slopes (from GNAO and GIRMOS) and compute the OL-DM commands. A summary of the MOAO baseline parameters is presented in Table 1.



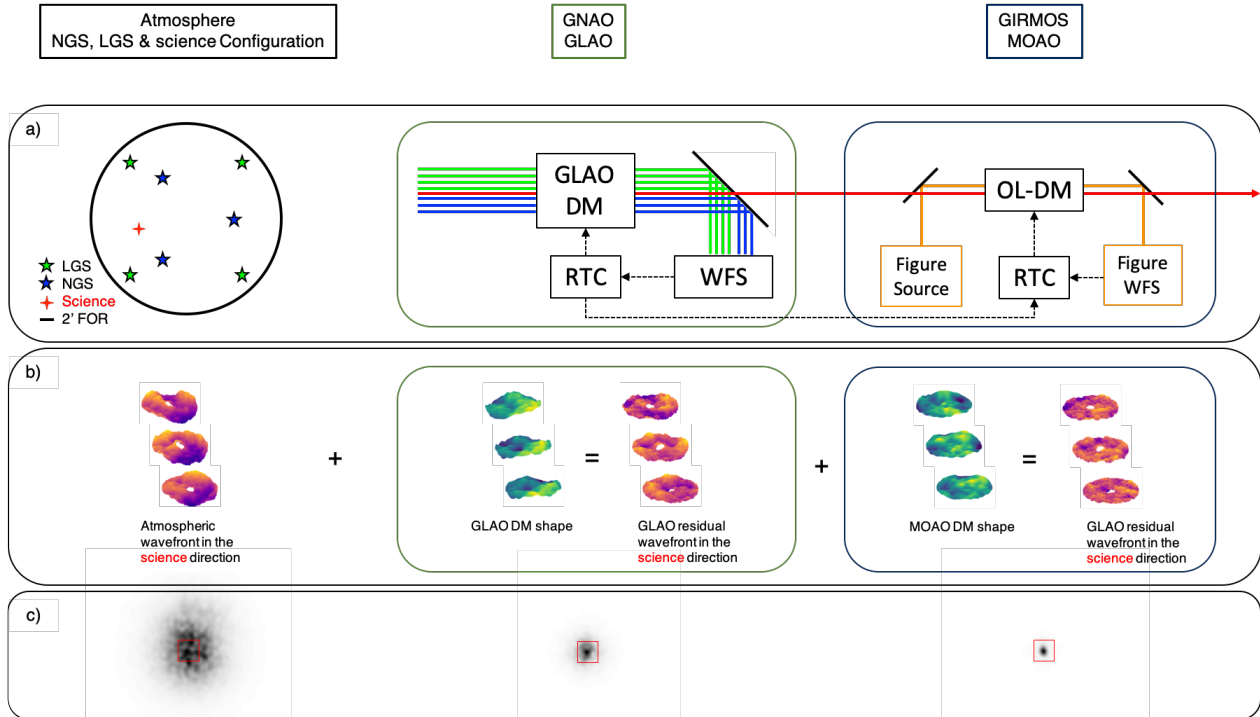


**Figure 33: a) Optical principle used to modelized the GIRMOS MOAO system. The light collected within the 2 arcmin FOV passes through the GNAO system where a first GLAO correction is performed, the GIRMOS object selection system will then direct the scientific light (in red) into the GIRMOS MOAO system where an additional AO correction in the science direction is achieved. b) Instantaneous wavefronts as well as the DM shape computed at the different stages of the instrument (seeing-limited, GNAO and GIRMOS). c) Typical integrated H-band PSF, seeing-limited, GLAO-corrected and GLAO+MOAO-corrected. The red square represents a 0.1 arcsecond spaxel.**

**Table 1: System parameters (Gemini, GNAO, GIRMOS).**

<b>Telescope</b>	<b>Gemini North</b>
Diameter	8 m
Central Obscuration ratio	0.14
Zenith Angle	30°
<b>Atmosphere</b>	<b>Mauna Kea 50%-tile</b>
$r_0$	0.186 m
Altitude	[0,0.5,1,2,4,8,16] km
Fractional $r_0$	[0.45,0.13,0.04,0.05,0.1,0.09,0.11]
Wind speed	[5.6,5.8,6.3,7.6,13.3,19.1,12.1] $\text{ms}^{-1}$
Wind direction	[190,255,270,350,17,29,66] °
<b>Deformable Mirror</b>	<b>GNAO: DMO</b>
Order	21x21
Pitch	0.4 m
Coupling	0.4
Conjugaison Altitude	0 m
<b>LGS Wavefront Sensor</b>	<b>GNAO: LGS-WFS</b>
Number	5
Order	20x20
Pixels per lenslets	8x8
Asterism position	(0,0) + 1.2' square

Framerate	500 Hz
Read-out Noise	0.5 e- rms
Wavelength	589 nm
<b>NGS Wavefront Sensor</b>	<b>GNAO: NGS-WFS</b>
Number	3
Order	1
Pixels per lenslets	20x20
Asterism position	30" circle
Framerate	500 Hz
Read-out Noise	0.5 e- rms
Wavelength	589 nm
<b>Open-Loop DM</b>	<b>GIRMOS: OL-DM</b>
Order	17x17
Pitch	0.5 m
Coupling	0.4
Conjugaison Altitude	0 m
<b>Figure Source</b>	<b>GIRMOS: FS</b>
Wavelength	780 nm
<b>Figure Wavefront Sensor</b>	<b>GIRMOS: CL-WFS</b>
Order	16x16
Pixels per lenslets	32x32
Framerate	200 Hz
Read-out Noise	0.5 e- rms
Wavelength	780 nm

## 2.5 Design Trade-Off Summary

The main driver of the MOAO design is the Image quality requirement to deliver [REQ-2-MOAO-0370] [AD-04]. The design of MOAO is built on heritage of the AO team at HAA-NRC using high fidelity simulations and experience. In particular, several members of the MOAO team were involved in VOLT and RAVEN, two Open-Loop on-sky demonstrator. Several trade studies were performed during the conceptual and preliminary design phases of GIRMOS. We highlight in this section the major trade-off which led to the design presented in this document.

### 2.5.1 MOAO architecture (GLAO + MOAO)

The idea of having a GLAO and MOAO system together is not new. It already has been identified in simulation that operating an MOAO system downstream a first GLAO or MCAO system, a woofer-tweeter MOAO system will significantly improve the image quality in the area of the MOAO correction, [RD-07], [RD-08] & [RD-09]. Note that a two-stage (GLAO+MOAO) correction has already been demonstrated on sky [RD-10] and is the baseline configuration for the future multi-object spectrograph MOSAIC planned for the European Extremely Large Telescope (E-ELT) as presented in [RD-11] (I think the current phase of the MOSAIC project descoped the MOAO).

Operating an MOAO system on top of GLAO residual offers several advantages. The wavefront is partially corrected by the GLAO system. Thus, the amplitude of correction (stroke on the DM) required on the MOAO system is small and the open-loop errors are reduced compared to an MOAO system only, correcting for full atmospheric turbulences. Note that the DM creep which contribute to the open-loop error is proportional in some degree to the amplitude of the DM actuators stroke.

The evident risk of such woofer-tweeter system is the operation and calibration complexity. In particular, the communications between the two RTCs (two different instruments in our case) is crucial. Hopefully for GNAO and GIRMOS the RTC are built on the same platform developed by HAA at NRC (HEARTS). The communication and the exchange of telemetry are included in the requirements, interfaces, and designs of both RTCs, allowing the operation of both AO systems as one.

## 2.5.2 MOAO reconstructor (POL vs residual slopes)

The tomographic reconstructor computes the OL-DM commands from the GNAO's WFS telemetry [RD-01]. To achieve the reconstruction of the wavefront in the science direction, we need to know the Cn2 profile of the atmosphere. Because GNAO will operate in closed loop with the WFS, only the residual wavefront can be reconstructed not the whole atmospheric one. This latter reconstruction is usually done using the DM commands telemetry in addition to the WFS and called pseudo-open loop (POL) telemetry. But, because the GNAO-DM0 is already correcting the ground layer, we need to remove its shape from the OL-DM. However, in baseline configuration, DM0 has not the same number of actuators than the OL-DM. Using a projection of the GNAO-DM0 shape into the OL-DM actuator space we can compute the commands we need to remove from the OL-DM. In order to avoid to remove the GNAO-DM0 shape, we are now considering the use of only the GNAO-LGS-WFSs' residual slopes. This implies a modification of the reconstructor and different approaches can be considered. Because the ground layer is corrected, the atmosphere is not the same and the reconstructor presented in [RD-01] has to be modified. Moreover, the ground layer correction is not perfect and difficult to evaluate. We are currently exploring the impact using an atmosphere with different ground layer residues of turbulences for the calculation of the optimal reconstructor. Figure 34 shows the EE performance assuming the two different reconstructors: POL based and residual slopes based with the assumption of a ground layer fully corrected by GLAO. Our results are showing very little difference between the two approaches (Figure 35). Note that a SLODAR is also considered to obtain the Cn2 profile needed to compute the reconstructor.

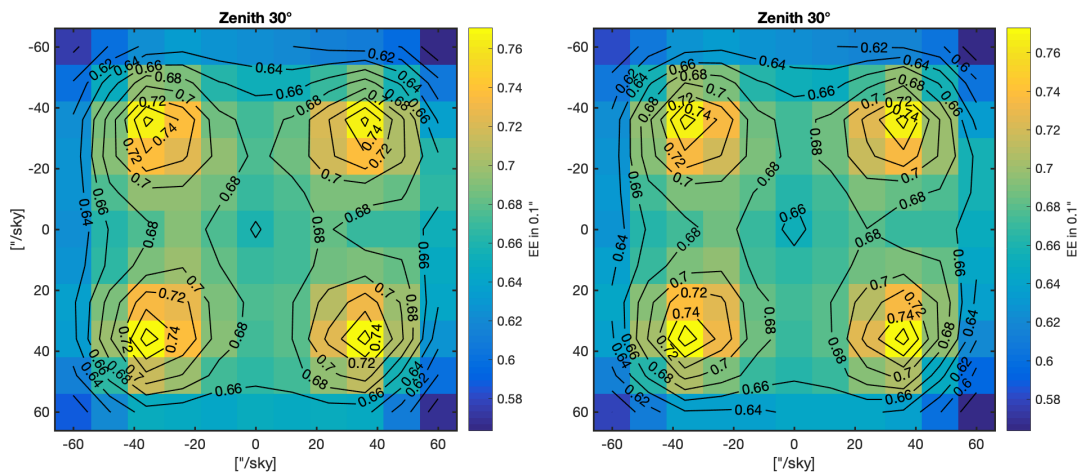


**Figure 34: EE<sub>01</sub> map over the 2 arcmin FOV. Left: POL based tomographic reconstructor. Right: Residual slopes only based tomographic reconstructor and assuming 0 ground layer turbulences.**

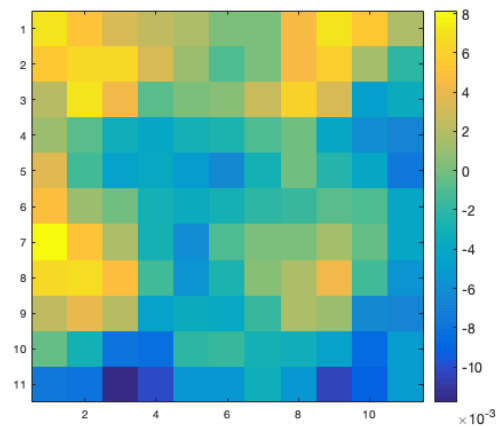


**Figure 35:  $EE_{01}$  difference map between the POL based reconstructor and the residual slopes only reconstructor assuming 0 turbulence at ground layer.**

### 2.5.3 GLAO (mean slopes vs tomography)

As baseline for our simulations, the ground layer DM commands are computed by averaging the signal of the WFSs (NGS and LGS). The GNAO team is considering a ground layer tomographic reconstructor optimized over an  $85''$  square centered in the telescope's FOV. We have now implemented in our code this specific mode and obtain as preliminary results a better GLAO correction.

### 2.5.4 MOAO System order

The system order plays a significant role on the performance of the AO system. It represents the number of WFS subapertures across the pupil diameter and drives the wavefront's sampling. The GNAO system is assumed to be in Fried configuration, the number of DM actuators is therefore equal to the WFS order plus one. Since the conceptual design where the GNAO system order was 16 [RD-04], the system order baseline raised up to 20 (GNAO private communication). So, we fixed the GNAO order to 20 and explored the impact of the GIRMOS order only. We noticed that the GNAO order essentially drives the wavefront measurement and has a stronger impact than the GIRMOS order. We computed the mean value of SR and  $EE_{0.1}$  over the full  $2'$  circular FOR, for different system order, see Figure 36. We found that the system order doesn't have a strong impact on the EE performances essentially because of the GNAO's order (20). We did not explore system orders larger than 20 because the wavefront sensing order is driven by GNAO and limits the tomographic information. Therefore, exploring an OL-DM with a higher order than the GNAO baseline will not provide better MOAO performances. The baseline order for the GIRMOS-MOAO system is fixed to 17. This number appears to be a safe spot between performances, risks and cost of the hardware, i.e. increasing the number of DM actuators to more than 17 becomes extremely expensive and also challenging for the RTC.

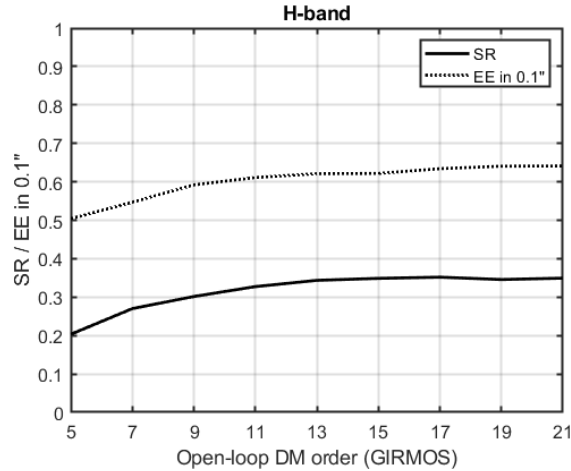


Figure 36: GIRMOS open-loop DM order impact, GNAO order is fixed to 20.

### 2.5.5 DM (see Appendix C)

We have conducted trade study on different DM technologies and Vendor during the conceptual design phase. The complete study can be found in Appendix C.

#### 2.5.5.1 Dead actuators

The baseline is an ALPAO DM 292 with High-Stability (HS) option. We already ordered one DM 292 HS option in order to conduct some test with the GIRMOS testbed with the goal of verifying the performance and the difference between the standard and High-Stability options. ALPAO recently finished the production of the DM. The DM was produced with 3 “dead” actuators (they are actually floating actuators). The company is claiming that with the production of HS option DM, a ratio of 1% dead actuators is expected and with any guaranty of zero dead actuators. ALPAO is now proposing 2 different DM High-Stability option, with both 3 “dead” actuators, BAX471 and BAX515. The position of the dead actuator for the 2 DMs is shown in Figure 37.

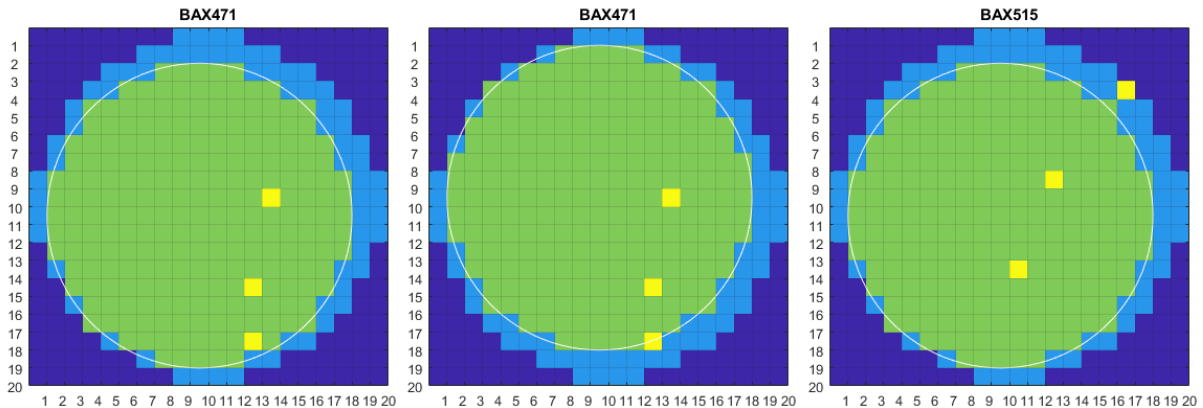
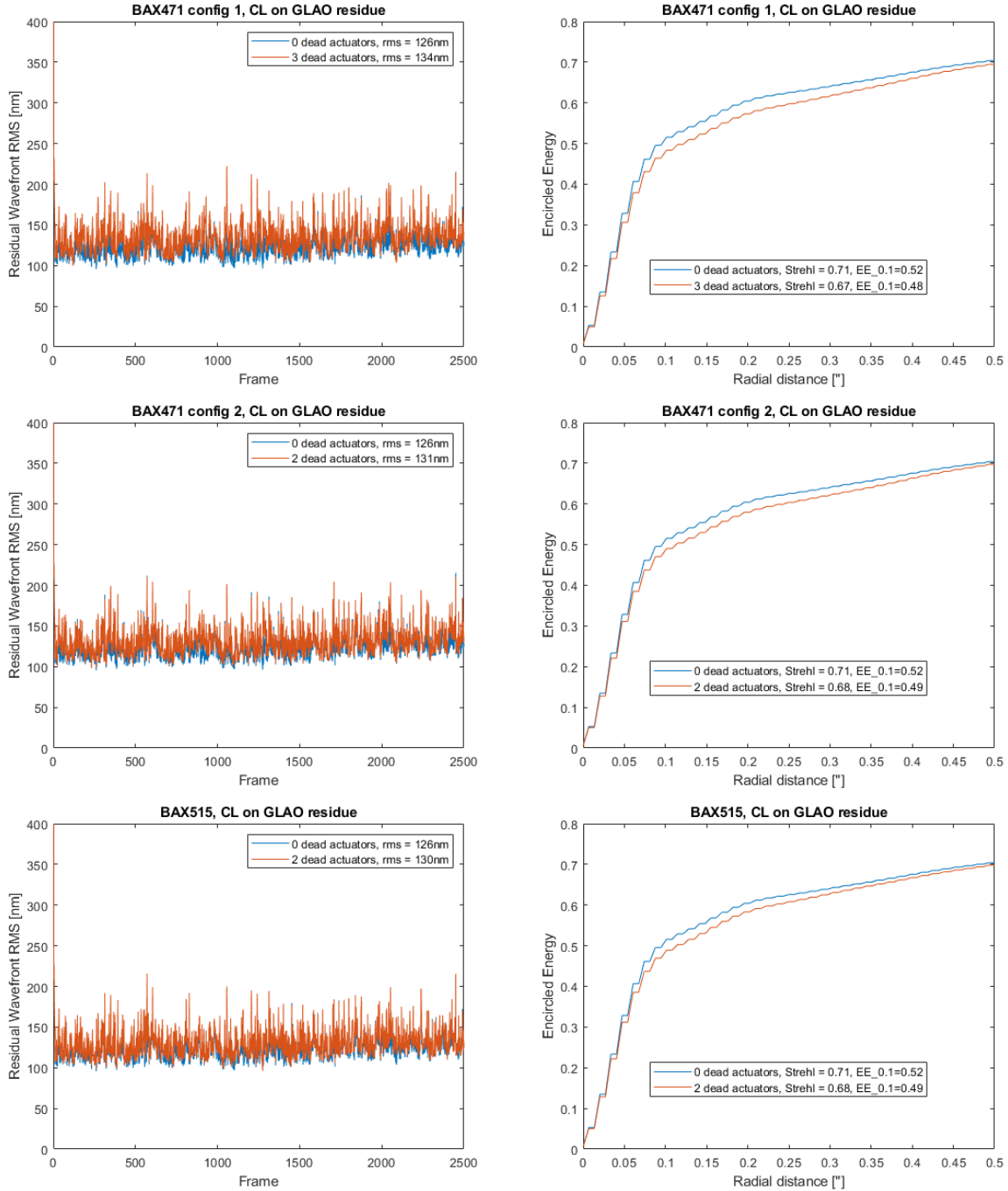


Figure 37: DM292 actuator map in shown light blue, green is the “active” actuators map for GIRMOS (17x17 actuators), the pupil (white) is not centered on the DM but shifted of one actuator pitch in x and y. Dead actuators are shown in yellow. *Left*: DM BAX471 in configuration 1 (3 dead actuators in the pupil). *Center*: DM BAX471 in configuration 2 (2 dead actuators in the pupil). *Right*: DM BAX515 (2 dead actuators in the pupil).

Therefore, we ran some simulations to understand the impact on performances for MOAO. We simply replaced the DM's influence functions corresponding to dead actuators by zeros, closed the loop with our CL-WFS on a typical GLAO residual wavefront. We extracted both the residual wavefront and the corresponding PSF for analysis.



**Figure 38: Residual wavefront (left) after closing the loop with on the GLAO-like residual wavefront and the corresponding PSF's Ensquared Energy profiles for different DM. Top: DM BAX471 in configuration 1 (3 dead actuators in the pupil). Center: DM BAX471 in configuration 2 (2 dead actuators in the pupil). Bottom: DM BAX515 (2 dead actuators in the pupil).**

We found that even if the residual wavefront error RMS is only affected by a couple of nanometers, see Figure 38 *left*, the PSF metrics (Strehl ratio and the Ensquared energy in 0.1") are significantly impacted (about 3-4% in I band).

### 2.5.6 WFS camera (see Appendix D)

We have conducted trade study on different WFS cameras technologies and Vendor. The full study can be found in Appendix D. The WFS Camera baseline is an Andor Zyla 5.5 USB3.

### 2.5.7 PSF reconstruction (Appendix E)

AO systems have irregular performances that depend on several changing conditions, such as the atmospheric turbulence, the guide stars luminosity, or the telescope zenith angle. A common method to determine the PSF of an exposure is to measure the light profile of a bright star within the FOV. When one is not available, as it is often the case in extragalactic observations, we can rely on the knowledge of the atmosphere and of the instrument to predict the general characteristics of the PSF. The GIRMOS strategy for PSF reconstruction is described in Appendix E. It uses the WFSs telemetry in conjunction with the statistical parameters of the turbulence, to predict analytically in real time several significant PSF metrics, such as the Strehl ratio and FWHM. This tool will be able to support the operation of GIRMOS on sky, as well as the analysis of the scientific data it delivers.

\$

## 2.6 RTC considerations and design

The full RTC design is described in Appendix F. The RTC design was contracted through NRC in the PDR phase, culminating in a design review in November 2021, and complete design and requirements documents. In addition, ICD documents were initiated to describe the interface of the GIRMOS and GNAO RTCs.

A key decision in this PDR-phase development is whether to have the GIRMOS RTC combined with the GNAO RTC. A clear outcome of the design and requirements contract was that GIRMOS should have its own stand-alone RTC as below.

### Down Select of GIRMOS RTC

Two RTC designs were considered during the RTC prebuild phase of the GIRMOS RTC. The first was a single RTC that would control both GNAO and GIRMOS AO bench and the other was for separate RTCs for both GNAO and GIRMOS. The design that had the strongest argument was for the separate RTCs. This will allow the GIRMOS team to build, integrate, and test independently, which will be important during the next few years. Separating the GNAO and GIRMOS RTCs also allows for more flexibility and options for Gemini should they wish to connect to a different downstream AO system in the future. Although the design of each RTC will be simplified, having two RTCs will require more coordination and communication between the two RTCs in order to share information. However, since the systems will be designed in a hierarchical fashion, that means that all the information will be sent by Gemini and then passed to the downstream to both RTCs which will not complicate communications from the Gemini system controller. The selected RTC design will result in a more streamlined, more robust system overall that will have undergone significant testing because that testing could be performed at earlier stages in development compared to the single RTC design.

**RTC design overview:**

The Herzberg Extensible Adaptive Real-time Toolkit (HEART) is a CPU-based software framework for the development of a Real-Time Controller (RTC) for a generalized Adaptive Optics (AO) system and is discussed in more detail in [RD2]. The building blocks of HEART are used to create an AO RTC, in this case the RTC for GIRMOS. Figure 2-1 shows the top-level context diagram of a HEART-based RTC for a Gemini AO-instrument. The specific context for the GIRMOS RTC is the same except GNAO is the upstream AO system for GIRMOS, and the “System Controller” is the GIRMOS Instrument Software (INSW) instrument sequencer (ISEQ), which is controlled by Gemini.

The RTC Command Handler accepts external commands (and internally distributes them to individual blocks as needed), and reports status back. The Hard Real-Time (HRT) Pipeline consists of all of the tasks that must be completed within one frame, or at most over a small number of frames (i.e., small fractions of a second). The Soft Real-Time (SRT) software consists of tasks that take much longer time (e.g., several seconds or more). The Telemetry Storage System handles the different types of telemetry in this design.

The HRT Pipeline is realized by configuring the HEART framework for the specifics of GIRMOS. HEART defines an internal interface layer that is common to all HEART-based RTCs. Access to physical hardware is done through custom interface/interpreter code blocks. For testing purposes, these external interface blocks can also be configured to pass information received from external simulators that provide pixel stream sources and command sinks to the RTC. This means that the external simulators pass the data using the internal interface layer. In HEART, the external simulators can be configured to read input data from a file and write output data to a file, thereby simulating the operation of an AO system without needing any AO hardware.

The GIRMOS RTC consists of 4 science channels. Each channel will run its own pipeline. The GNAO RTC will pass gradients from its 4 LGS Wavefront Sensors to each GIRMOS RTC science channel via the WFS Gradient Input block. There will be one input block per LGS WFS (4 in total). Each LGS gradient is passed to a High Order Reconstructor block for tomographic reconstruction where the control matrix is applied. There will be 4 High Order Reconstructor blocks for each science channel (16 in total). The 4 partial HO vectors are then passed to the Partial Vector Summation block to be summed and sent to the Temporal Filtering and Combination (TFC) block. This approach is more efficient than having one common tomography block sending a large three-dimensional atmospheric model to separate DM fitting blocks.

Each GIRMOS RTC science channel will also include an Internal Wavefront Sensor (WFS), which can operate in Truth or Figure mode. The internal WFS pixels will be received and read by a WFS input block, which calibrates the pixels. In the High Order NGS Pixel Processing block, the gradient pairs for each subaperture are computed from the calibrated pixels and centroid coefficients. The Non Common Path Aberration (NCPA) vector between the DM and Truth/Figure WFS (depending on operation mode) is subtracted from the scaled gradients. The resulting gradients are passed to a High Order Reconstructor block where a wavefront vector will be reconstructed by multiplying gradients by the control matrix (similar to HO Recon block above). If operating in Truth Mode, the resulting Internal/Truth WFS vector will be passed to the TFC block. If operating in Figure Mode, the resulting Internal/Figure WFS vector will be passed to the Open Loop Wavefront Correction (OLWC) block.

At the TFC block, the Non Common Path Aberration (NCPA) vector is subtracted from the HO Vector. If the GIRMOS RTC is running in Truth Mode, the Truth Wavefront Sensor (TWFS) vector will be integrated after a gain is applied (modal optical gain – provided by the SRT). The TWFS vector needs to be projected to DM space. When operating in Figure Mode, the TWFS steps will be skipped. Next in the pipeline is the Open Loop Wavefront Correction (OLWC) block. If the GIRMOS RTC is running Figure Mode, the Figure Wavefront Sensor (FWFS) vector will be applied (integrated) in this block. Actuator extrapolation will be performed on the DM error vector. At this point, disturbance injection can occur for testing purposes and system flat calibration applied. The DM commands will be clipped before being sent to the Wavefront Corrector (WC) output block. At the WC output block, a custom handler will scale the DM commands to the



device units required and send them to the DM electronics. If operating in Figure Mode, the DM command vector will be subtracted from the FWFS vector and the resulting errors will be scaled, integrated, and projected to fine tune the next set of DM commands.

## 2.7 Manufacturability Assessment

The DM and WFS manufacturability is discussed in the relevant trade study appendices.

## 2.8 Risks Retirement Activities

We present in this section, two on-going experiments (MOAO Testbed and REVOLT Open-Loop) with the goal of retiring some risks associated to MOAO, in particular the open-loop calibration and operation (go-to-errors).

### 2.8.1 MOAO Testbed

The goal of the testbed is to develop a prototype MOAO system similar to the final GIRMOS MOAO subsystem (one arm). The testbed has one configuration and the concept of operation as well as the optical layout are presented respectively in Figure 2 and Figure 3. This bench will allow to test most of the MOAO components (DM, FS and WFS) individually as well as some functionalities of the system, in particular, the go-to errors management with the figure source and the figure WFS.

- Simple bench design reusing some of the RAVEN parts to focus on open-loop control issues rather on tomography (which would require a full GNAO simulator)
- Verify MOAO calibration techniques with a calibration DM having a different order than the MOAO DM (it's the case for GIRMOS with GNAO DM0)
- Test the 3 different MOAO modes useful for GIRMOS:
  - Pure open-loop (OL) AO
  - OL AO + Figure Source
  - OL AO + low-bandwidth Truth WFS
- Once available, characterize GIRMOS DM go-to errors (creep, thermal).
- Test MOAO performance with GNAO like residual wavefront errors and tomographic error.

#### 2.8.1.1 Principle of operation

The GIRMOS testbed simulates the Gemini Telescope, the atmosphere, the GNAO correction achieved in a specific science direction and the GIRMOS MOAO system. The bench is made of 4 main components (see Figure 2): the SLM, the open-loop WFS (OL-WFS), the open-loop DM (OL-DM) and the figure WFS (F-WFS) also named closed-loop WFS (CL-WFS). The SLM plays the GNAO GLAO or MCAO residual wavefront. The OL-WFS can check the quality of the wavefront and is used for calibrations. The OL-DM provides the GIRMOS additional correction and the CL-WFS is used as a Figure WFS in order to cancel the go-to errors. The CL-WFS will also be tested as a truth sensor in an additional low bandwidth closed-loop for relatively compact and bright scientific targets. The bench is interfaced with OOMAO which will compute the GNAO residual wavefront in the science direction and the associated commands for the OL-DM. The open-loop DM and the CL-WFS are in Fried configuration (one actuator at each corner of the WFS subapertures) to maximize the WFS signal.

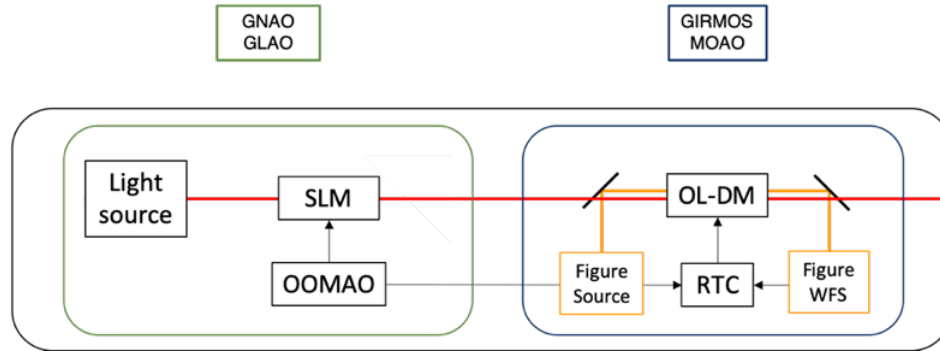


**Figure 39: Optical principle for the GIRMOS MOAO testbed. The top of the figure illustrates the optical and telemetry paths.**

The optical layout of the bench is shown in Figure 3. a). The light emerging from the source is spatially filtered by a pinhole, and a linear polarizer selects the appropriated polarization for the SLM to operate under pure phase modulation. A first achromatic lens (80 mm focal length) collimates the beam on the SLM, the diameter of the input pupil is 6.4 mm. A magnification telescope, composed of lens pair (80 mm and 300 mm focal length) conjugates the SLM plane with the DM (24 mm pupil diameter). Another achromatic lens (300 mm focal length) focuses the beam on the science camera. In between the pair of lenses, a 50:50 dichroic mirror reflects half of the light to the OL-DM path. The transmitted light is directed to another achromatic lens (38 mm focal length) which in combination with the 80 mm lens conjugates the OL-WFS lenslet array plane (3 mm pupil diameter) on the SLM. Just before the science camera, another 50:50 dichroic transmits half of the light to the CL-WFS path where a similar lens as for the OL-WFS (38 mm focal length) conjugates the CL-WFS lenslet array plane (3 mm pupil diameter) on the DM. Another dichroic is inserted between the first dichroic and the 300 mm lens, thus allowing us to place the figure source in a focal plane and illuminate the DM and the CL-WFS. The science camera has a high pass filter to filter the light from the figure source. Note that a subaperture of 8x8 pixels on the WFSs corresponds to 32x32 pixels on the SLM.

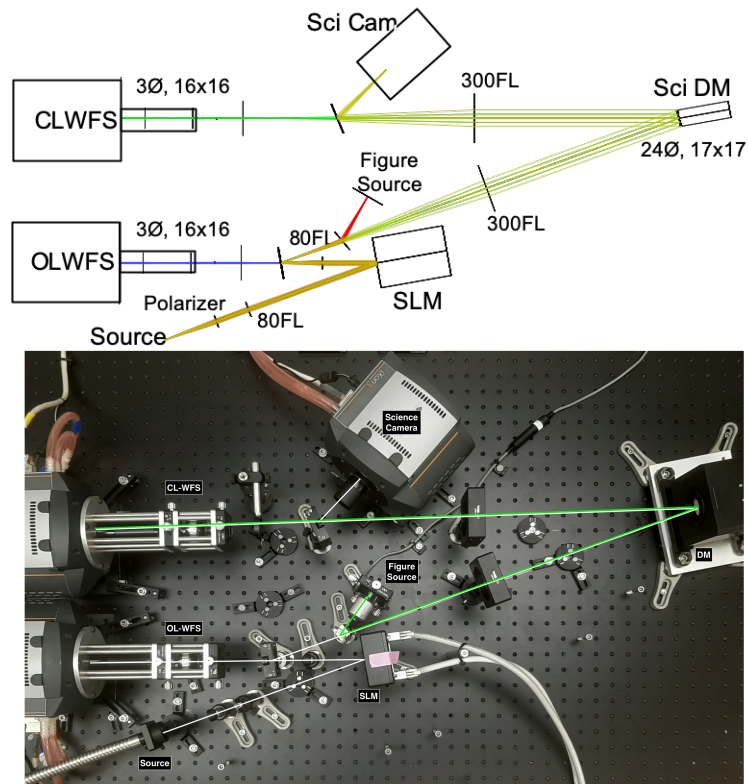


Figure 40: a) Optical layout of the GIRMOS MOAO testbed. b) The testbed fully integrated in the HAA AO lab.

### 2.8.1.2 Hardware

We converged to some suitable hardware allowing us to test and validate the different aspects of the GIRMOS MOAO system, most of the part are visible in Figure 40 b). Thanks to the RAVEN collaboration, which allowed us to use some of the instrument's parts. The SLM is a Hamamatsu (X13267-07) with 800x600 pixels of 12.5 $\mu$ m pitch, allowing a 2pi phase shift from 620 to 1100 nm. The DM is an ALPAO DM277 with 1.5 mm inter-actuator pitch from the RAVEN calibration unit. Each WFSs is made of a custom lenslet array coupled to an Andor iXon3 860 EMCCD camera with 128x128 pixels of 24  $\mu$ m from RAVEN. For the scientific camera we are now using an Andor camera (Zyla 5.5 sCMOS) with smaller pixels than the Andor Ixon3 860. For the science light source, we are using an LED at 780nm and for the figure source we are using an LED at 550nm. The testbed is fully integrated, is operational and sits in the AO lab at HAA. All the components are interfaced and controlled with Matlab and OOMAO, see Figures 3b and 4.

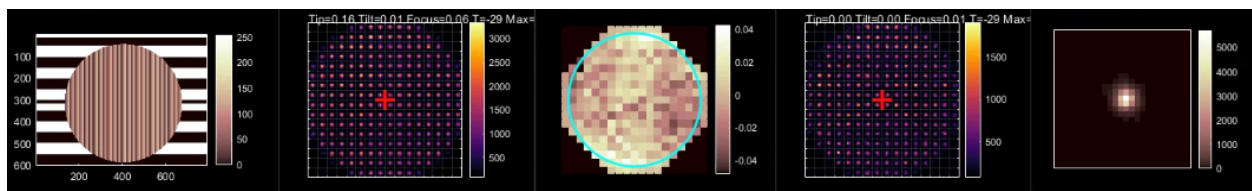


Figure 41: Image of the testbench real time display. From left to right (following the light path): The SLM shape, the OL-WFS spots, the DM shape, the CL-WFS spots and the science camera's PSF.

### 2.8.1.3 Tests & Results

Here is a list of the various system-level tests we have done or plan to do with the testbed.

- Science camera and WFS plate scale measurement (with the calibrated SLM). **[TBED-SYS-TEST-010]**
- NCPA calibration and correction. **[TBED-SYS-TEST-020]**
- System calibration (interaction matrices). SLM/DM/WFSs registration. **[TBED-SYS-TEST-030]**
- GLAO performance at 780nm (and 980nm) with the science camera, PSF analysis. In closed-loop (SCAO) and in open-loop. **[TBED-SYS-TEST-040]**
- MOAO performance at 780nm (and 980nm), PSF analysis and rejection transfer function (RTF).
  - Pure Open-loop. **[TBED-SYS-TEST-050]**
  - Open-loop + Figure WFS closed-loop. **[TBED-SYS-TEST-060]**
  - Open-Loop + Truth WFS closed-loop. **[TBED-SYS-TEST-070]**
- DM go-to-errors characterization. **[TBED-SYS-TEST-080]**
- Additional tests, vibration, miss registration, ... **[TBED-SYS-TEST-090]**
- Software development (High-level, bench super-class, ...)

#### **Plate Scale [TBED-SYS-TEST-010]**

This is the plate scale measurement of the Science camera and the WFSs. For the science camera, this is relatively simple, the idea is to inject a known tilt on the SLM and measure the field motion of the PSF in the science camera. As we know the PV of the tilt we applied, the SLM's pupil size (6.8 mm) and Gemini's pupil size (8m) we can compute the pixel scale.

- $slope = \frac{PV \text{ tip or tilt}}{Pupil_{SLM}} \frac{1}{4.85e^{-6}} [\text{arcsec}]$
- $magnification = \frac{Pupil_{SLM}}{Pupil_{Gemini}}$
- $PixelScale = \frac{slope * magnification [\text{arcsec}]}{Field \text{ motion} [\text{pixels}]}$

We can now compute the sampling of the PSF using the FWHM of the PSF at diffraction:

- $\lambda = 0.780 [\mu m]$
- $\theta = 1.028 \frac{\lambda}{D} \frac{1}{4.85e^{-6}} = 0.0206 [\text{arcsec}]$
- $Sampling = \frac{\theta}{PixelScale} [\text{pixels}/FWHM_{Diff}]$

**Table 2: Pixel scale and sampling measurement with tip.**

Tip injected [ $\mu m$ PV]	Field Motion [pixel]	Pixel Scale [arcsec/pixel]	Sampling [pixels/ $FWHM_{Diff}$ ]
3.12	6	0.0134	1.54
6.24	12	0.0134	1.54
9.36	17	0.0142	1.45

**Table 3: Pixel scale and sampling measurement with tilt.**

Tilt injected [ $\mu\text{m PV}$ ]	Field Motion [pixel]	Pixel Scale [arcsec/pixel]	Sampling [pixels/ $\text{FWHM}_{\text{Diff}}$ ]
3.12	6	0.0134	1.54
6.24	11	0.0146	1.42
9.36	17	0.0142	1.45

As by design we know the detector pixel size and the  $F_{\text{number}}$  of the beam on the science camera, we can directly compute the sampling of the PSF.

- $\text{PixelSize} = 6.5 [\mu\text{m}]$
- $F\# = 12.5$
- $\lambda = 0.780 [\mu\text{m}]$
- $\text{Sampling} = \frac{1.028 F\# * \lambda}{\text{PixelSize}} \left[ \frac{\text{pixels}}{\text{FWHM}_{\text{Diff}}} \right]$
- $\text{Sampling} = 1.54 \left[ \frac{\text{pixels}}{\text{FWHM}_{\text{Diff}}} \right]$

We find good agreement between the expected sampling of 1.54 pixels/ $\text{FWHM}_{\text{Diff}}$  from design and the measured sampling ( $\sim 1.49$  pixels/ $\text{FWHM}_{\text{Diff}}$ ).

### **NCPA [TBED-SYS-TEST-020]**

#### *Eye Doctor*

We developed a simple Eye doctor algorithm for PSF sharpening and NCPA estimation. The algorithm injects iteratively different Zernike mode amplitude for the first 36 modes or more. For each mode, we identified the amplitudes maximizing the PSF's peak value and applied it on the SLM. Note that we are using the SLM to inject the Zernike modes and not the DM, the DM is maintained in flat position after closing the loop with the CL-WFS.

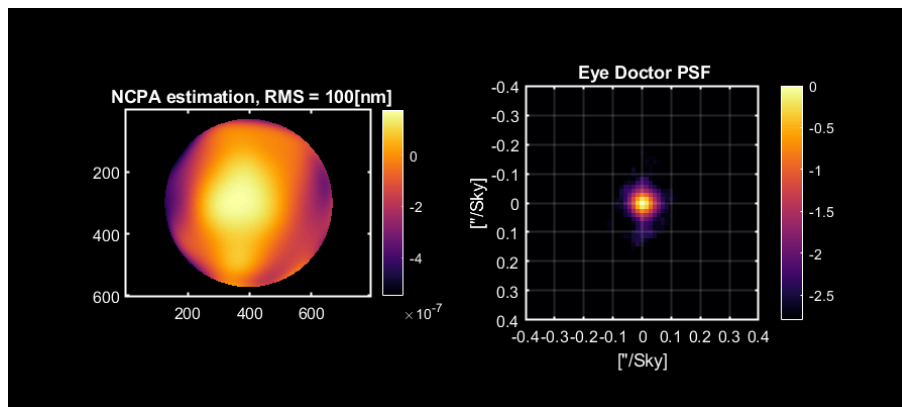


**Figure 42: Bench NCPA estimation (100nm RMS), NCPA corrected PSF (Strehl = 92%)**

#### *Phase Diversity*

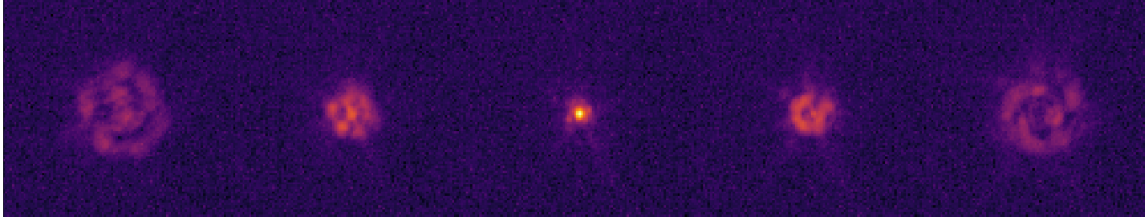


Figure 43: Example of in and out of focus PSFs. These images are used to run the phase diversity algorithm allowing to compute the NCPA.

**System calibration & registration [TBED-SYS-TEST-030]**

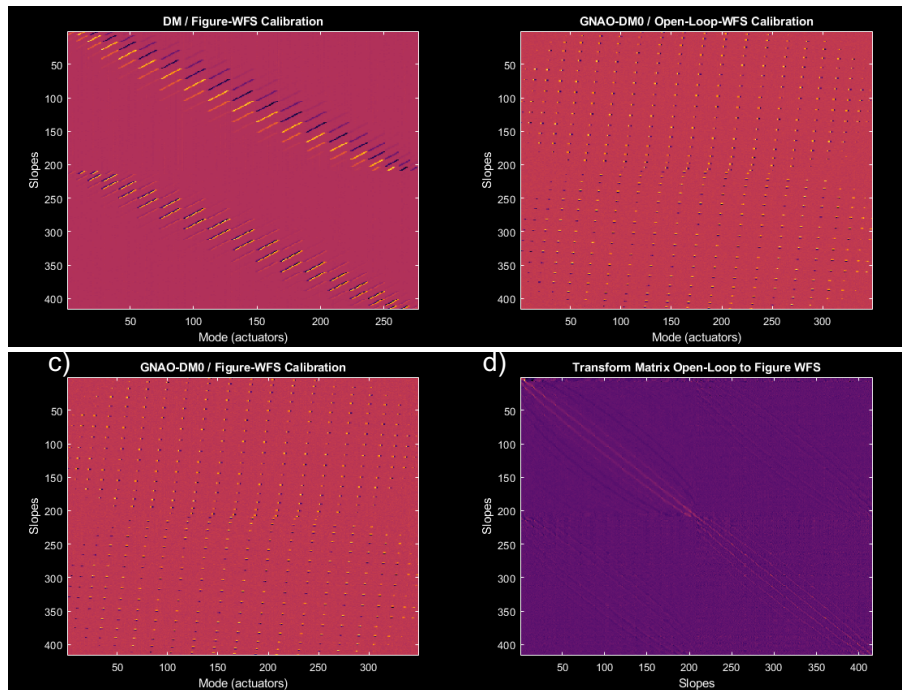


Figure 44: Different interaction matrices used on the bench. a) DM / CL-WFS interaction matrix using the figure source and the DM. b) GNAO-DM0 / OL-WFS interaction matrix ( $S_1$ ) using the science source and the SLM as GNAO-DM0. c) GNAO-DM0 / CL-WFS interaction matrix ( $S_2$ ) using the science source and the SLM as GNAO-DM0. d) The matrix (TF) used to transform the OL-WFS slopes into CL-WFS slopes in order to control the DM. This matrix is generated with  $S_1$  and  $S_2$  as  $TF = S_2 * S_1^T * (S_1 * S_1^T)^{-1}$ .

**GLAO and GLAO+SCAO performance [TBED-SYS-TEST-040]**

The goal of this test is to evaluate the ability to inject GLAO residual wavefront with the SLM, measure the injected wavefront with OL-WFS, and close the loop on the GLAO residual with the DM and the CL-WFS. Thus, allowing us to measure the performances the AO system can achieve and compare it with simulations (Figure 9). For this test we used the science source (780nm).

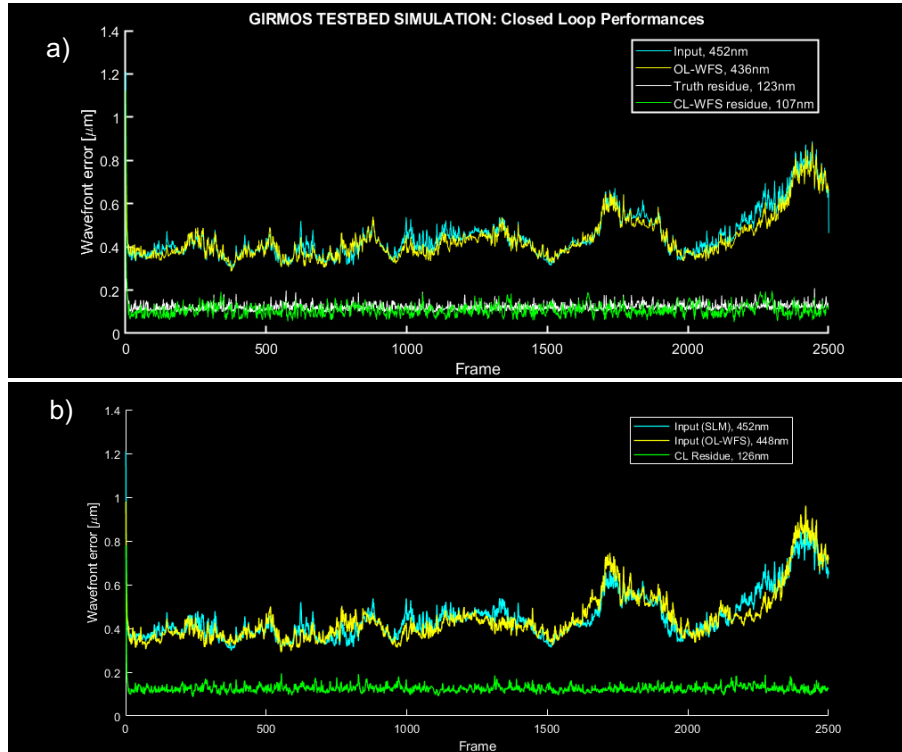


Figure 45: a) Testbed simulation showing the GLAO injected (cyan) and measured (yellow) wavefront error and the GLAO+SCAO residual wavefront (green). b) Testbed measurement showing the GLAO injected (cyan) and measured (yellow) wavefront error and the GLAO+SCAO residual wavefront (green).

#### Pure Open-loop [TBED-SYS-TEST-050]

For this test we are using the same configuration as for the previous test. For the OL residue (magenta curve in Figure 46) we are controlling the DM in open-loop using the telemetry coming from the OL-WFS the residual wavefront is computed from the CL-WFS measurements.

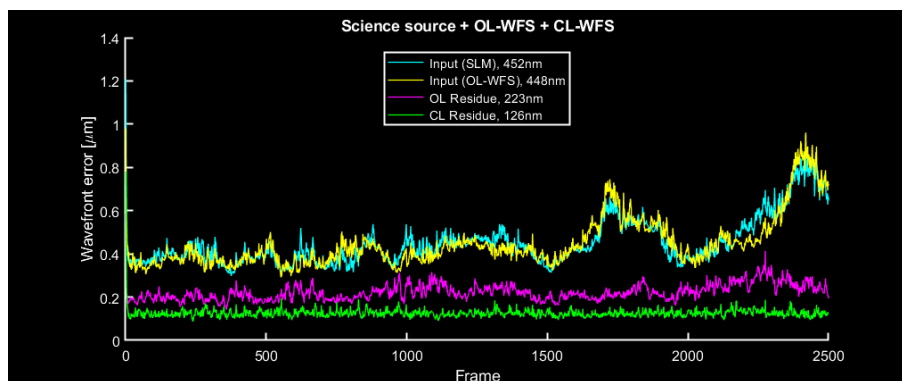


Figure 46: Testbed measurement showing the GLAO injected and measured wavefront error, the GLAO+SCAO residual wavefront and the open-loop residual wavefront.

#### Open-loop + Figure WFS closed-loop [TBED-SYS-TEST-060]

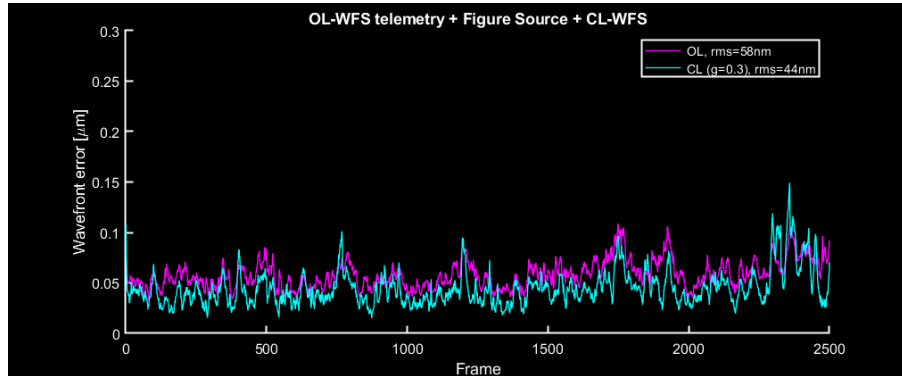


Figure 47: Testbed measurement showing the OL wavefront error measured using the FS and the CL-WFS. The magenta curve represents the wavefront error between the DM shape and the expected shape as measured by the figure source WFS (CL-WFS).

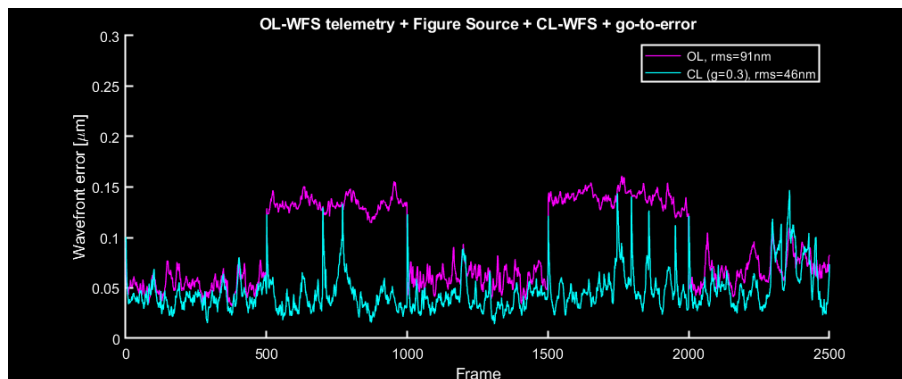


Figure 48: Testbed measurement showing the OL wavefront error measured using the FS and the CL-WFS. The magenta curve represents the wavefront error between the DM shape and the expected shape as measured by the figure source WFS (CL-WFS). We manually injected some significant go-to-errors on the DM to test the FS closed-loop.



## 2.8.2 REVOLT Open-Loop

The goal of the project described in this section is to test on sky several of the final components (hardware, software, and procedures) by using the REVOLT bench. This experiment will allow to investigate and retire several risks of the GIRMOS MOAO subsystem long before its integration and commissioning.

The main objectives are:

- Development of the calibration procedure to generate the OL command matrix and testing of the OL performance on sky (Section 2.8.2.2).
- Integration and use of the REVOLT CU that will be repurposed as the MOAO verification unit during integration and testing (Section 2.8.2.3).
- Preliminary testing of the GIRMOS RTC for the MOAO acceptance (Section 2.8.2.6).

### 2.8.2.1 REVOLT

REVOLT is an adaptive optics bench in development at NRC-HAA in Victoria for the McKellar Telescope on site. It is a successor to the VOLT experiment [RD-01] implemented on the same telescope. The aim of the instrument is to be a platform to develop and test on sky new AO technologies and algorithms. As such, it can become a valuable tool in the development of the MOAO subsystem of GIRMOS with the addition of an OL-WFS and a dedicated calibration unit.

#### **Telescope**

The instrument will be mounted on the McKellar Telescope at NRC-HAA, on Observatory Hill in Victoria. It is an optical reflective telescope of 1.22 m in diameter (F/34.5) with a coudé focus located in a room under it. The telescope is optimized for visible wavelengths (0.5 transmittance), but the transmission in J and H band (0.55 and 0.33, respectively) is sufficient to allow for long-exposure observations of bright stars also in the NIR.

The McKellar Telescope differs from the Gemini North telescope—where GIRMOS will be housed—not only by size but also by atmospheric conditions. Particularly relevant for AO are the turbulence characteristics which in Victoria are, unsurprisingly, more challenging than on Maunakea. It has been measured that the median Fried parameter ( $r_0$ ) at 500 nm on the 1.22m telescope is 0.05 m, much worse than a typical value of 0.186 m for Hawaii. While this staggering difference makes operating OL with REVOLT less similar than with GIRMOS, it allows to stress-test our MOAO procedures and algorithms.

#### **Instrument**

REVOLT was originally designed as a CL NGS SCAO system (Figure 49 and Figure 50). The light from the telescope focal plane is collimated (L1) on a deformable mirror (Alpao DM272) with 17 actuators on the pupil diameter. The beam is then refocused (L2) and split in an optical and an infrared path using a dichroic filter.

Coudé focus

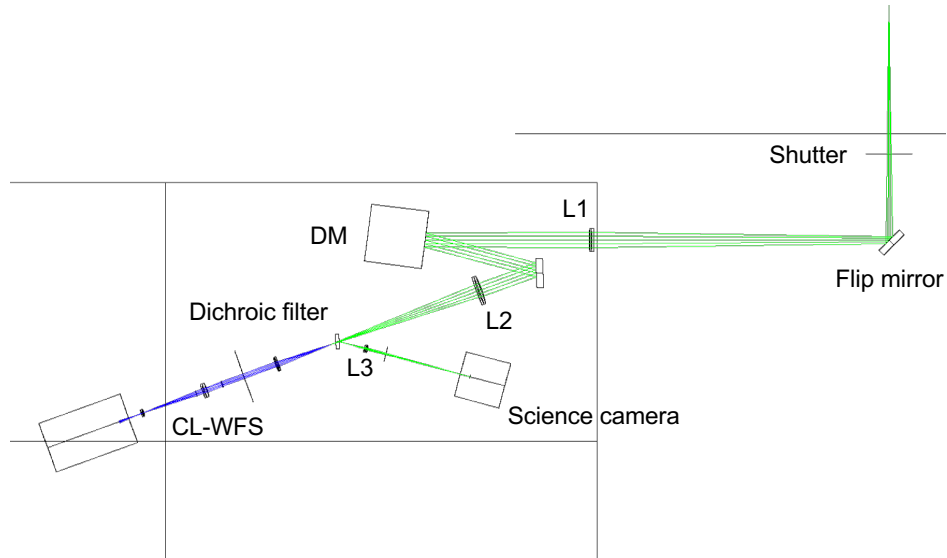


**Figure 49: Optical design of REVOLT (CL mode).**

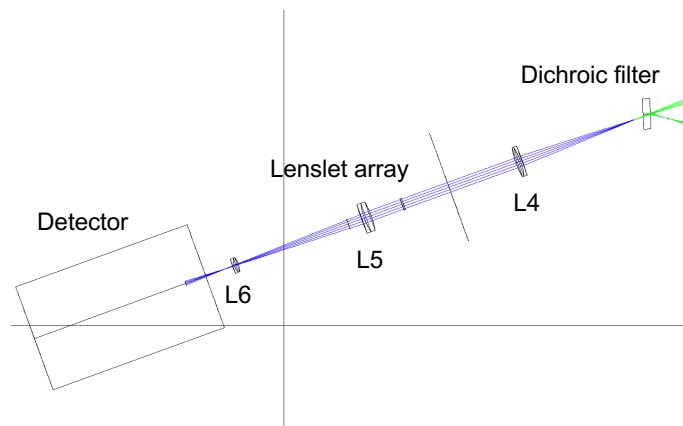


**Figure 50: Optical design of the REVOLT CL-WFS.**

The infrared light is reflected by the dichroic filter toward a “science” camera (Allied Vision’s Goldeye G-008 Cool TEC1) operating in the 1000-1650 nm wavelength range. It will observe the same NGS used by the WFS. The image of the star will reflect the PSF of the system, which provides important performance benchmarks (e. g., FWHM, SR, EE).

The optical light continues past the dichroic filter and is detected by a 16×16 SHWFS using the First Light’s CMOS detector C-BLUE One (1.7 MP), described in Table 4.

**Table 4: Characteristics of the C-BLUE ONE detector.**

Wavelength range	350-900 nm
Peak QE	73% (@ 550 nm)
Pixel size	9 μm
Area	1604 × 1100 px

Frame rate	480 Hz
Dark current	0.96 e <sup>-</sup> /s/px
RON	2.33 e <sup>-</sup> /px

### 2.8.2.2 OL-WFS

One of the main differences between the REVOLT design described in Section 2.7.2.1.2 and the GIRMOS MOAO system is the loop mode, with the former being “close” and the latter “open”. To utilize REVOLT as a GIRMOS surrogate, we need to add an OL-WFS to the bench. At the end of the OL experiment on REVOLT, the OL-WFS detector and lenslet array will be “re-cycled” in one of the arms of the GIRMOS MOAO.

The OL-WFS will have a similar optical design to the CL-WFS, using the same C-BLUE ONE detector (Table 1) and a lenslet array of the same order (16×16). Since the OL-WFS has to observe the wavefront before it reaches the DM, our solution is to add a visible light beam splitter before the DM (Figure 3). We are considering to use a 50/50 beam splitter, in order to operate the two WFSs (and modes) with similar photon fluxes.

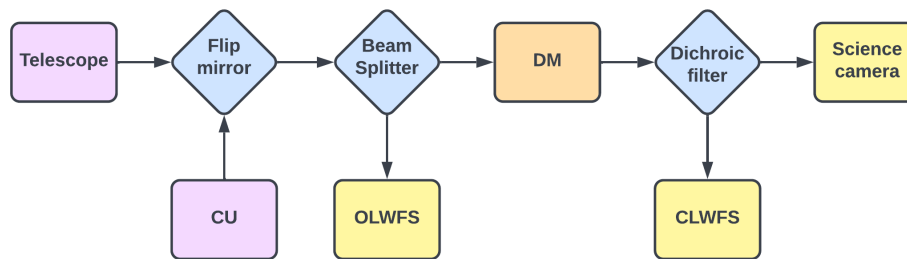


**Figure 51: Diagram of the light path in REVOLT.**

Another important distinction between GIRMOS and REVOLT is that the latter will correct the full atmospheric turbulence, while the former will deal only with the residual wavefront after the GNAO correction. This difference cannot be removed, but we still need to keep it in mind in determining if the REVOLT OL mode has a chance of producing a diffraction-limited PSF. For this reason, we have implemented an end-to-end simulation of the system using the OOMAO code [RD-02]. We have found that a framerate of 400 Hz can produce a high-SR (~50%) under the typical atmospheric conditions in Victoria.

One of the challenges of running the OL-WFS at 400 Hz is the possibility that the detector becomes photon-starved, considering the combination of small size of the subapertures (7.6 cm), detector’s quantum efficiency (0.7), telescope transmittance (0.6), atmospheric absorption in the visible (0.6) and CL/OL beam splitter (0.5). We have performed a (conservative) calculation of the photon noise, sky background, and detector’s characteristics to determine the limiting NGS magnitude. To be able to detect small systematic errors in the AO correction, we need them to dominate the random errors of the centroids of the SHWFS spots. In Figure 4 we show that to achieve a SNR of at least 10, we need an NGS brighter than magnitude 3 in V band. While this limitation makes only a handful of stars suitable to be used as NGS at any time, our experiment is not constrained by the need to observe a scientific target within their isoplanatic angle.

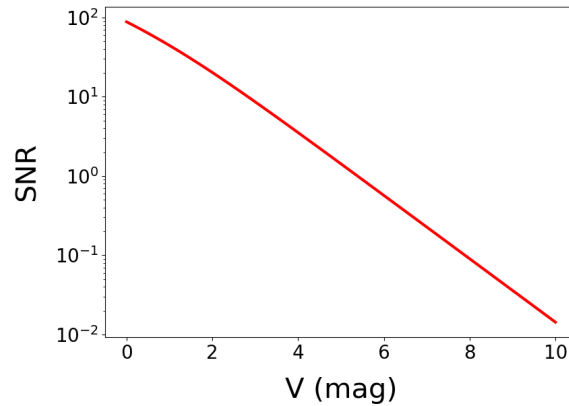


**Figure 52: Simulation of the SNR of one spot in one frame of the OL-WFS, as a function of the NGS magnitude.**

A further dissimilarity from GIRMOS is the lack of a dedicated FWFS in REVOLT. This component is required to monitor the quasi-static shape of a DM during the operation of the instrument, which can slowly change from its calibrated profile. This drift is invisible to the OL-WFS and it would affect negatively the performance of the spectrograph. We can solve this deficiency on REVOLT by making simultaneous use of both WFSs. While the OL-WFS measures the atmospheric turbulence and corrects it at high framerates, the CL-WFS can act as the slower FWFS.

A FWFS would typically require its dedicated light source in front of the DM, but we have decided to not include it—or to not use the CU of Section 5—for two reasons. First, we would have to replace the flip mirror of Figure 3 with another beam splitter to combine the light coming from the telescope and the CU. This would cause a loss in sensitivity of all the detectors downstream. Second, the OL-WFS and CL-WFS would be observing two sets of spots each (the NGS and the calibration source), complicating the job of the RTC. Our solution is to use the NGS itself as the “figure” source. A caveat of this choice is the risk that the FWFS would measure and rectify also the residual atmospheric turbulence that the OL did not correct. This would amount to “cheating” the open loop, and it would defy much of the experiment. The solution is to implement a spatial and temporal filter to the CL-WFS slopes. By measuring only a few dozen Zernike modes using a slow framerate (1-10 Hz), the FWFS would filter out most of the atmospheric turbulence residuals. After that, the resulting slopes are then transformed into DM commands through the CL command matrix (Section 5), and are provided at regular intervals to the RTC as an offset DM command.

### 2.8.2.3 CU

Accurate and repeatable calibrations of the CL and OL command matrices and NCPAs can be achieved by placing a diffraction-limited artificial source in front of REVOLT with the same F/# as the telescope. The optical design is shown in Figure 53. This design allows to repurpose the CU—at the end of the REVOLT experiment—as the AOVU unit [AD-01] needed for the MOAO verification phase [AD-02].

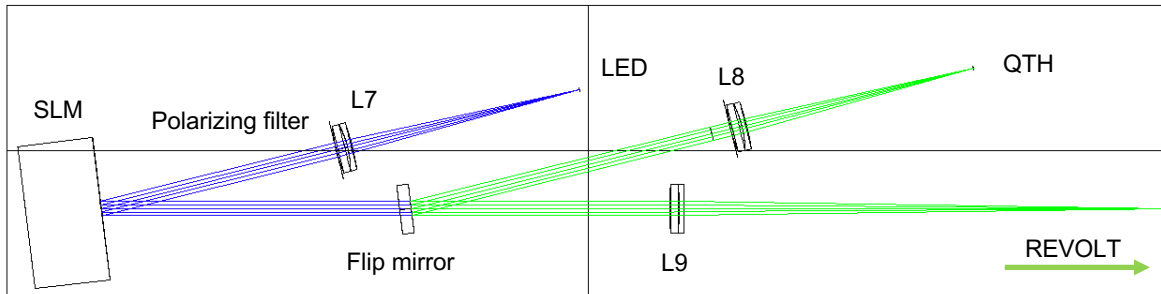


**Figure 53: Optical design of the REVOLT CU.**

#### 2.8.2.4 CL

The CU requirement for the CL mode is the calibration of the CL-WFS/DM command matrix and the CL-WFS/science NCPA. The former will be computed from the interaction matrix registered by poking the DM actuators one-by-one and measuring the slopes on the CL-WFS. For the NCPA calibration, we have to find the DM command that maximizes the quality of the science PSF. It is commonly achieved through procedures like image sharpening (of the SR) with a simplex algorithm. For this task, the CU needs a light source that can be observed by both the science camera (NIR) and the CL-WFS (visible). We have chosen to employ a fiber bundle and QTH lamp with a wavelength range from 240 to 2700 nm.

#### 2.8.2.5 OL

The only requirement for the OL mode is to map the slopes from the OL WFS to the CL WFS space [AD-01]. For this task, we need to produce a set of aberrations—similar to the pokes for a command matrix—that can be seen by both WFSs. On GIRMOS, this task will be executed by the GNAO DM0 [AD-01]. On REVOLT, since the OL system is correcting the full atmosphere, we need to have such a deformable mirror in the CU.

We have chosen to use a SLM and because of its high spatial resolution and the availability at NRC. One of the problems associated to the use of a SLM is its reduced stroke range, about  $3\pi$  radians in the visible. To achieve a higher OPD, we can “wrap” the phase periodically ( $2\pi$ ), like in a Fresnel lens (Figure 54). Since the wrapping process is chromatic, we are compelled to use a monochromatic source to produce a diffraction-limited source. To perform the calibration with high SNR, we will use a 1A LED at 660 nm, near the quantum efficiency peak of the OL WFS detector (see Table 4).

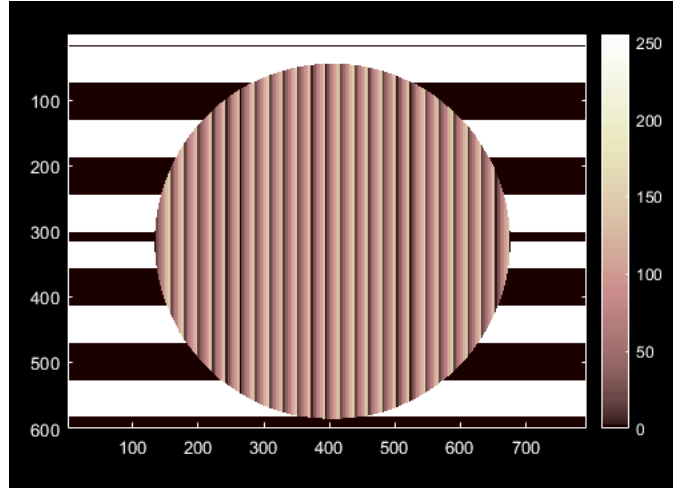


**Figure 54: Pixel map of the SLM for a tilted wavefront. The vertical stripes inside the pupil are wrapped with a frequency of  $2\pi$  radians to produce the tilt.**

Another issue in using a SLM is the need to use linearly polarized light. For this reason, there will be a polarizing filter between L7 and the SLM (Figure 53).

#### 2.8.2.6 RTC

REVOLT will be the first instrument to implement HEART, the new RTC developed by NRC, which will be utilized on GIRMOS. The OL experiment can contribute to the MOAO verification phase [AD-02] by providing an early assessment of several aspects of the RTC performance.

- Our on-sky, real-time experiment will test the loop speed and time lag of the OL and FWFS modules of the HEART software.
- The DM and WFS detectors mounted on REVOLT will be similar—if not the same—as those in GIRMOS. We will be able to certify in advance that these components are compatible with the RTC computer architecture.
- The calibration of the MOAO subsystem requires access—both reading and writing—to many parameters stored within the RTC, such as DM commands, WFS slopes, and command matrices. We will learn how to interface directly with HEART, and to use communication protocols with an external computer.
- Basic detector calibrations such as dark subtraction, flat fielding, and pixel masking will be tested and automated.
- We can begin the development of various scripts that analyze the data stream of the DM commands and WFS frames, useful for diagnosing the system in real time.
- Having access to complete and realistic telemetry will support the development of our strategy for PSF reconstruction [REF].

#### 2.8.2.7 Time Schedule

The REVOLT bench in its CL configuration has been already assembled in the AO Lab at NRC. The only missing piece of hardware is the C-BLUE ONE detector, which is expected to arrive during Q2 2022. The bench is planned to see first light in the early summer of the same year. If it will not be feasible to integrate it by that time, we will use a temporary WFS detector. This telescope run would still be useful to check alignment, throughput and RTC operations. The OL-WFS—as well as the OL part of the CU—will be added to the bench later during the year. In Table 2 we provide a tentative time schedule for the integration and “commissioning” of REVOLT (CL and OL).

**Table 2: REVOLT time schedule for 2022.**

<b>APR</b>	<b>MAY</b>	<b>JUN</b>	<b>JUL</b>	<b>AUG</b>	<b>SEP</b>	<b>OCT</b>
CU alignment	CU integration	First light (CL)		C-BLUE ONE	OL-WFS alignment	First light (OL)

### 3 Analysis

#### 3.1 Optical Analysis

For the optical analysis please refer to OSEL design document [AD-07].

#### 3.2 Mechanical Analysis

This section discusses any analyses performed on any of the components which comprise the MOAO Subsystem.

##### 3.2.1 Sensitivity Analysis

This section lists the optical components used in the MOAO subsystem and compares the actual range and resolution of each mount to those required for optical alignment.

**Table 5: MOAO Components mechanical sensitivity.**

Assembly Name	Components	Part No	DOF provided	Design Resolution <sup>1</sup>	Required Range and Resolution <sup>1</sup>	Comments
<b>DM Assembly</b>			<i>DZ RY, RZ</i>	<i>1<math>\mu</math>m 1.5<math>\mu</math>rad</i>	<i><math>\pm 1</math> deg, &lt;25<math>\mu</math>rad</i>	
<b>Figure Source</b>	Light Source		<i>DX, DY DZ</i>	<i>TBD</i>	<i><math>\pm 1</math> mm &lt;25<math>\mu</math>m <math>\pm 5</math> mm 0.1mm</i>	
	Fold Mirror		<i>RX, RY</i>	<i>&gt;<math>\pm 2</math> deg, 0.1<math>\mu</math>rad</i>	<i><math>\pm 1</math> deg, &lt;25<math>\mu</math>rad</i>	
<b>WFS Path</b>	Corrector plate cell		<i>None</i>			
	Fold Mirror (M11) mount		<i>RX, RY</i>	<i>&gt;<math>\pm 2</math> deg, 0.1<math>\mu</math>rad</i>	<i><math>\pm 1</math> deg, &lt;25<math>\mu</math>rad</i>	
	Collimator lens	Thorlabs CP1XY Cage Flexure	<i>DX, DY DZ</i>	<i>3.5<math>\mu</math>, 10<math>\mu</math>m 3.5<math>\mu</math>, 10<math>\mu</math>m</i>	<i><math>\pm 1</math> mm ,5<math>\mu</math>m <math>\pm 2</math> mm ,50<math>\mu</math>m</i>	Design resolution is intrinsic to flexure cage
	Lenslet array	Thorlabs CP1XY Cage Flexure	<i>DX, DY DZ RZ</i>	<i>3.5<math>\mu</math>, 10<math>\mu</math>m 3.5<math>\mu</math>, 10<math>\mu</math>m Infinte rotation, &lt;0.5mrad</i>	<i><math>\pm 1</math> mm ,5<math>\mu</math>m <math>\pm 2</math> mm ,50<math>\mu</math>m <math>\pm 3</math> deg, 1mrad</i>	Design resolution is intrinsic to flexure cage
	Relay lenses (2)		<i>DZ</i>	<i>9 <math>\mu</math>m</i>		Based on lens tube threading
	WFS Camera		<i>DZ RX, RY</i>	<i>1 <math>\mu</math>m 1.3 <math>\mu</math>rad</i>	<i>Not Specified</i>	

##### 3.2.2 Analysis of the Deformable Mirror (DM) Deflection Under Varying Gravity Vector

While most of the MOAO mounts can be considered rigid, the deformable mirror may not fall into that category. The engineering data given only states bounding box dimensions with a mass of “~1kg”. No information is given about where the center of gravity lies, if the mass is evenly distributed through the housing or, if there is a lumped mass, how it is attached to the housing. Further, there is no information on how mass of the housing is transferred to the attaching features (threaded fasteners in the base). Because of this, a basic finite element analysis (FEA) was performed on the housing/adjustable base assembly using a simplified model of the housing. For the analysis, the following assumptions were made:

- 1/16” (1.6mm) thick sheet stainless steel housing
- Any mass over and above that of the housing would be in the area of the mirror
- The center of gravity of the DM would be close to the actual deformable mirror
- Based on the previous point, addition of a ring- shaped mass centered behind the mirror (in order attain he correct mass



The screen capture in Figure 29 shows a section view of what was modeled. 2 gravity case were explored:

1. Gravity vector perpendicular to the side of the DM
2. Gravity vector perpendicular to the front (mirror) face

From those two cases the resulting deflections at the center of the mirror face were found to be  $\sim 3 \mu\text{m}$  in case 1 and  $\sim 4 \mu\text{m}$  in case 2. Included below is a screen capture of Case 2. The primary deformation is from the inherent flexibility in the base of the DM housing (as modeled).

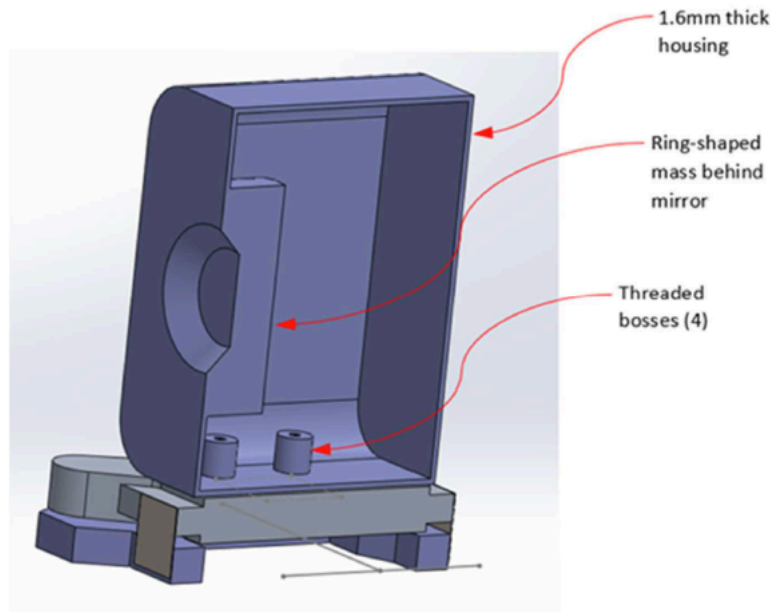


Figure 55: Conceptual model of DM assembly for FEA.

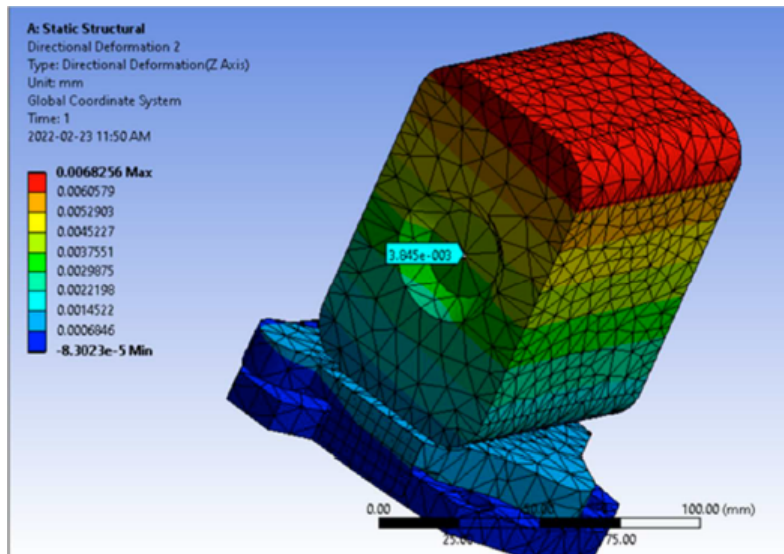


Figure 56: FEA results for DM assembly (gravity vector perpendicular to mirror face).

Analytically, as modeled there is only the thin SS housing in the base of the DM where the bolted attachment would occur (some internal bosses were added for the attachment screws to avoid unrealistic stress concentrations on the FE model). If the base of the DM housing (or the housing altogether) is (actually)

thicker, that would reduce the deformations. Also, this model assumes where the mass over and above the housing needs to be added and the position of the center of gravity. If the additional mass is located elsewhere or attached differently, that would alter the results. If more information on the geometry of the DM can be obtained, a more accurate analysis could be run. It should also be noted that this amount of deformation represents a change in gravity vector on the DM that would require 6 hours to occur in normal operations. The fact that the stability specification is run over a much shorter time period should reduce any concerns from this analysis.

For completeness it is noted that the first mode of vibration (fore-aft rocking) is just under 224 Hz.

### 3.3 Electrical Analysis

We have performed a power budget estimation.

#### 3.3.1 Components Power Consumption

##### 3.3.1.1 DM

ALPAO specifies 500W maximum power consumption for the electronics box. The MOAO power budget being very limited, we can't afford such a high-power consumption. We therefore, asked ALPAO to provide a better power estimation for the DM292. While waiting for more information from ALPAO, we performed some measurement in the lab using another ALPAO DM, the DM468 (468 actuators controlled from one electronic box) from the NEW EARTH LAB. The measurement was done either by pushing all the actuators to respectively 0, 2.5, 5, 7.5, 10 and 12.5% of the maximum stroke (12 $\mu$ m TT for the DM468). Assuming a linear conversion, we can convert the stroke in  $\mu$ m. The results obtained are shown in Figure 5. The 0 $\mu$ m stroke corresponds to the factory flat. Note that the electronic box required 70W when just connected and not applying the factory flat. We also tested to push only 292 actuators instead of all the 468, the 176 remaining actuators were maintained in factory flat position. From simulation (see Figure 58), we have an estimation of the DM stroke requirements. We estimated that 3.5 $\mu$ m stroke is required in poor seeing conditions and from Figure 57 we can extrapolate a linear consumption of about 200W for such a stroke. Note that we will never push all the actuators of the DM to 3.5 $\mu$ m at the same time, so our estimation is an upper limit. **Assuming some margin, a maximum power consumption of 800W is estimated for the DMs.**

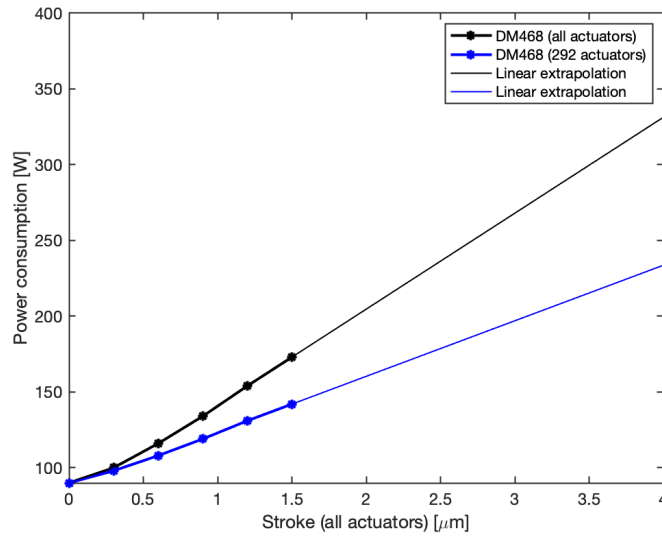


Figure 57: Power consumption of the ALPAO DM468.

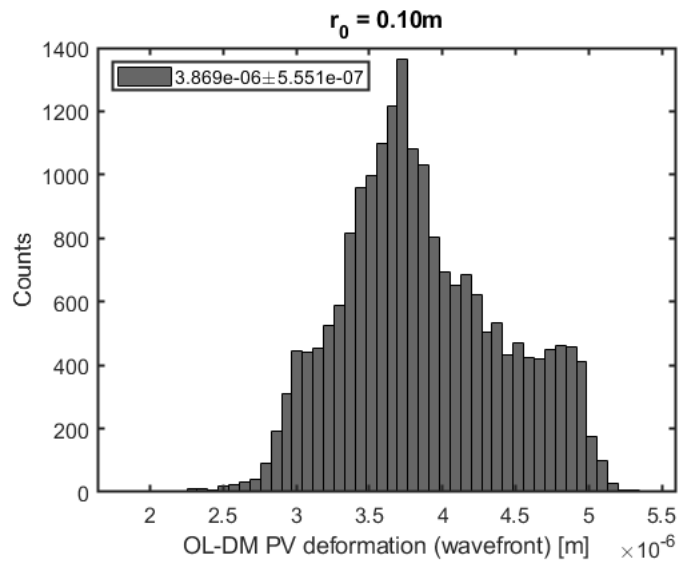


Figure 58: Expected mirror deformations from simulation.

### 3.3.1.2 WFS

Assuming the Andor Zyla 5.5 camera [see, AD-04], the maximum power consumption is 60W per camera. **We estimate therefore, a maximum power consumption of 240W for the WFSs.**

### 3.3.1.3 FS

For the FS, the LEDs require a 5V voltage and a maximum current of 100mA so we can estimate a consumption of 2W for controlling 4 LEDs. **Assuming some margin, we can estimate a maximum consumption of 30W for the FS.**

### 3.3.1.4 RTC

Assuming the RAX QS12-22E2, and based on the expertise of the RTC team at HAA, a power consumption of 600W is required without the PCIe boards. For the DM PCIe boards, we estimated a maximum power consumption of about  $4 \times 1.62 = 6.5W$  (we can expect only 3.25W if we combine the electronic boxes). For the WFS cameras PCIe boards we found a power requirement of maximum 4W per camera, so we estimated a power consumption of about  $4 \times 4 = 16W$ . **In total, assuming the PCIe boards, we estimated a maximum power consumption of about 625W.**

### 3.3.2 MOAO Power Requirement Summary

We provided an estimation of the GIRMOS MOAO power requirement. This estimation is probably an upper limit, especially due to some uncertainties on the DMs power requirement. In the coming weeks, we will be able to estimate the DM power consumption more precisely from our MOAO TESTBED, using an ALPAO DM277 with the same configuration (number of moving actuators) as with the DM292.

**Table 6: Summary of the MOAO power budget.**

Subsystem component	Maximum Power consumption
DM (upper limit)	800W
WFS	240W
FS	30W
RTC + (PCIe)	600W+25W
<b>Total</b>	<b>1695W</b>

## 3.4 Performances Analysis

The performances are extracted from simulation and modelling of the GNAO-GIRMOS AO system using the parameters described in Section 2.4.

### 3.4.1 Baseline performance

We provide the nominal performance of GNAO operating in GLAO mode. The  $EE_{0.1}$  and SR performances are shown in Figure 59 *left*. Averaging the values over the 2' FOR, we find  $EE_{0.1} = 51\%$  with a standard deviation across the field of 1% and  $SR = 11\%$  with a deviation of 1%. For this set of simulations, the ground layer DM commands are computed by averaging the signal of the WFSs (NGS and LGS). The GNAO team is considering a ground layer tomographic reconstructor optimized over an 85'' square centered in the telescope's FOV. We have now implemented in our code this specific mode and obtain as preliminary results a better GLAO correction.

The GIRMOS main operating mode is GLAO+MOAO. For this configuration, GNAO is operating as mentioned in the previous section. For this set of simulations, the OL-DM commands are computed using the pseudo-open loop (POL) signal built from the GNAO-LGS-WFSs' residual slopes and the DM0 command.

The  $EE_{0.1}$  and SR performances are shown in Figure 59 *right*. Averaging the values over the 2' FOR, we find  $EE_{0.1} = 60\%$  with a standard deviation across the field of 1% and  $SR = 29\%$  with a deviation of 2% which are in the requirement previously discussed, [REQ-2-MOAO-0370] [AD-01].

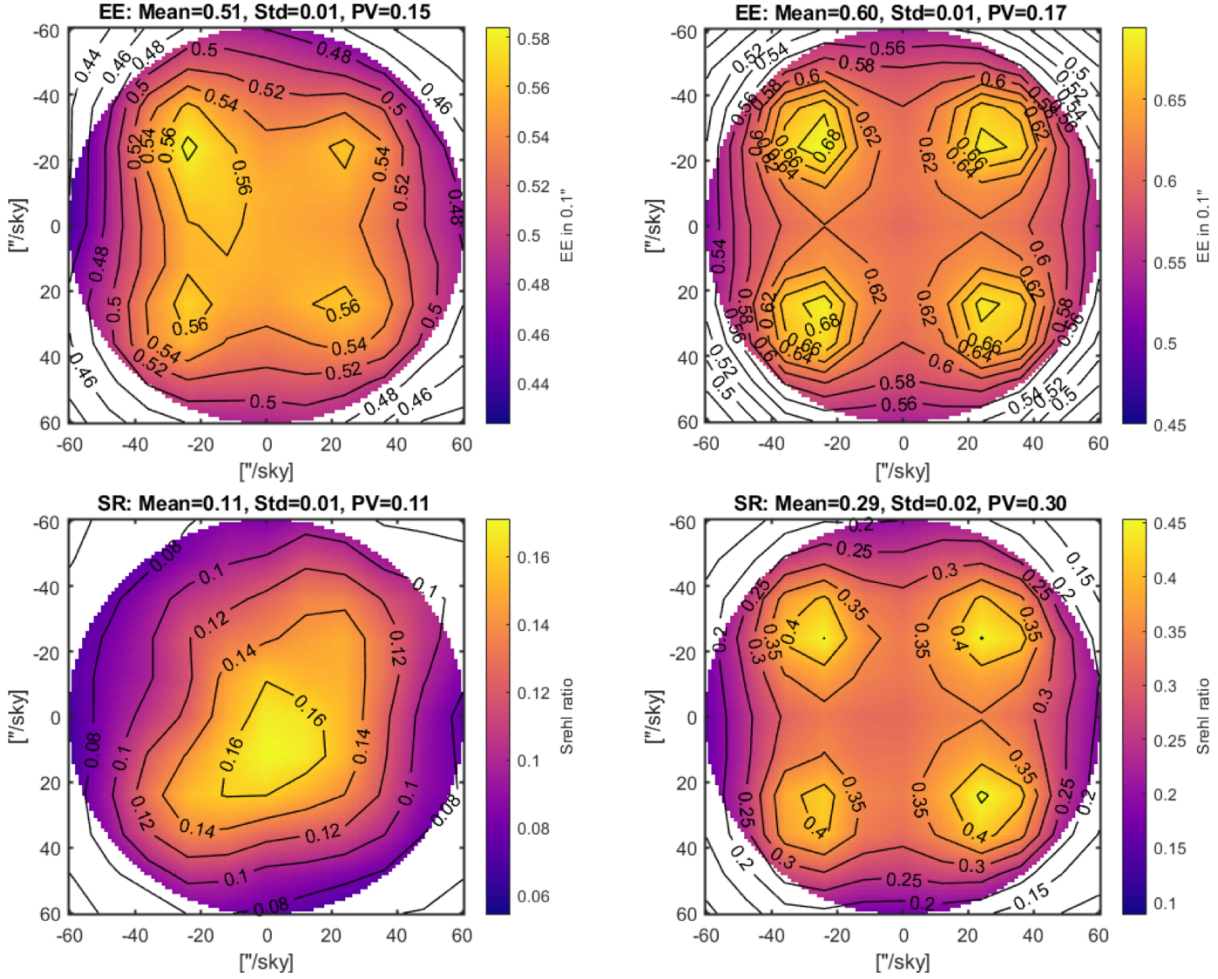


Figure 59: H-band  $EE_{0.1}$  (top) and SR maps (bottom). Left: GLAO mode with baseline parameters. Right: GLAO+MOAO mode with baseline parameters.

### 3.4.2 Atmospheric conditions

We explored different atmospheric conditions essentially through the  $r_0$  parameter, while keeping the same 50 percentiles atmospheric profile. In Figure 61 left, we can see that the area where  $EE_{0.1}$  is equal to 52%, reduces drastically for small  $r_0$  values. The GLAO as well as the MOAO performances are rapidly limited by the tomographic error as explained in [RD-08]. The mean SR value over the FOR is slightly less impacted as the  $EE_{0.1}$ , see Figure 61 right.

GNAO must operate down to a zenith angle of  $50^\circ$  (GNAO private communication). We therefore studied the impact of the zenith angle on the GIRMOS image quality for values from  $0^\circ$  to  $60^\circ$ . The zenith angle  $\zeta$  will essentially affect the Fried parameter  $r_0$  as shown in Equation 1.

$$r_0(\zeta) = \cos(\zeta)^{3/5} r_0(0) \quad (1)$$

From Figure 61, we can extract the zenith angle impact. Using Equation 1 we can compute  $r_0(\zeta)$  value assuming the baseline value of  $r_0(0) = 0.186\text{m}$  and a zenith angle of  $30^\circ$ . The SR and  $EE_{0.1}$  average value

on the FOR and up to 50% of the FOR is meeting the requirements, for zenith angle down to 50° which corresponds to a  $r_0 = 0.14-0.15\text{m}$  in Figure 60.

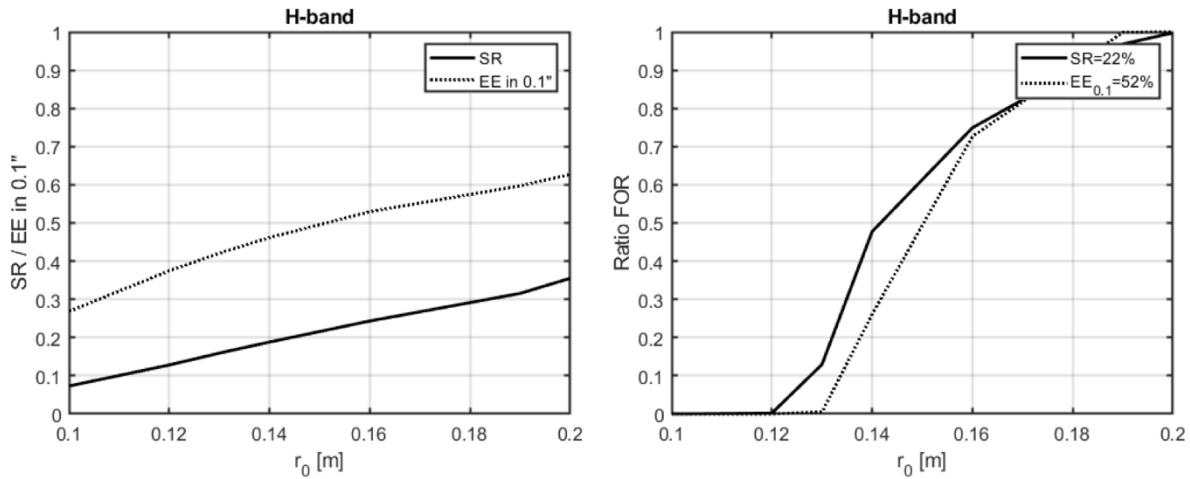


Figure 60: *Left:* Values of EE<sub>0.1</sub> and SR averaged over the FOR. *Right:* Ratio of the GIRMOS FOR where the requirement is reached for both EE<sub>0.1</sub> = 52% and SR = 22%.

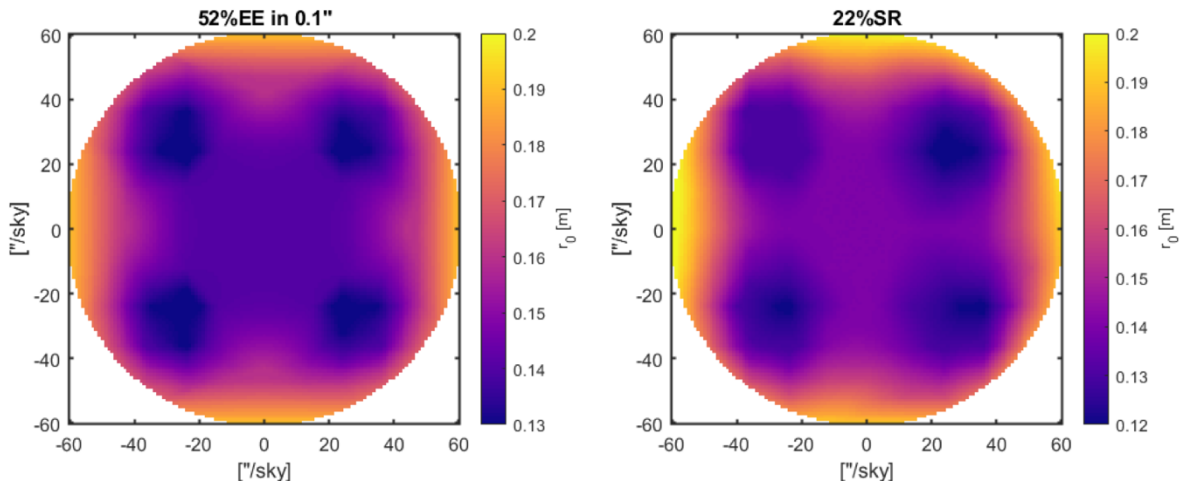


Figure 61: *Left:* Surface where EE<sub>0.1</sub> = 52% for different  $r_0$  values translated at zenith (color code). *Right:* Surface where SR = 22% for different  $r_0$  values (color code).

We also extracted the residual wavefront error for one position in the 2 arcmin FoV for which the EE<sub>0.1</sub> value is the same as the averaged EE<sub>0.1</sub> value on the 2 arcmin FoV. In Figure 62, we can see that for an  $r_0=0.186\text{m}$  the wavefront error should be around 320nm RMS. Note that for an  $r_0=0.15$ , the wavefront error measured is about 390nm RMS.

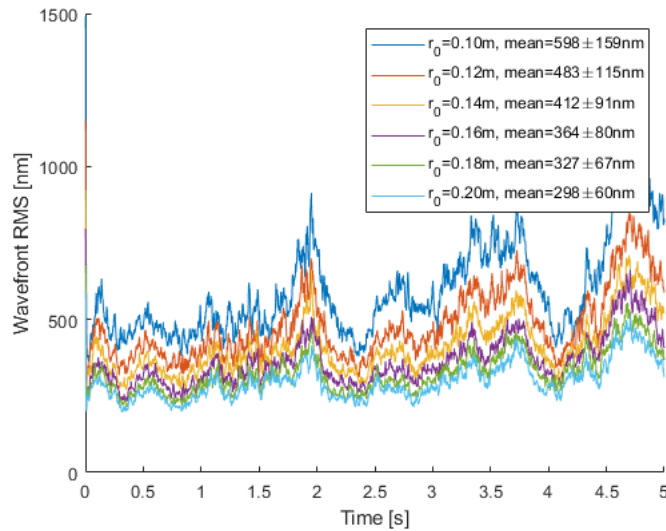


Figure 62: GLAO+MOAO residual wavefront error in nm RMS for different  $r_0$  (colors).

### 3.4.3 LGS Asterisms

We present in this section the expected MOAO performances assuming different LGS configurations: 5LGS with 4 in a 70.7" square (radial distance of 50") and a central star (**5LGS**), 4LGS in a square for 3 different radial distances: 42.4", 45" and 50" (**4LGS-A**, **4LGS-B**, **4LGS-C**), 4LGS with 3 in an equilateral triangle (radial distance of 50") and a central star (**4LGS-T**).

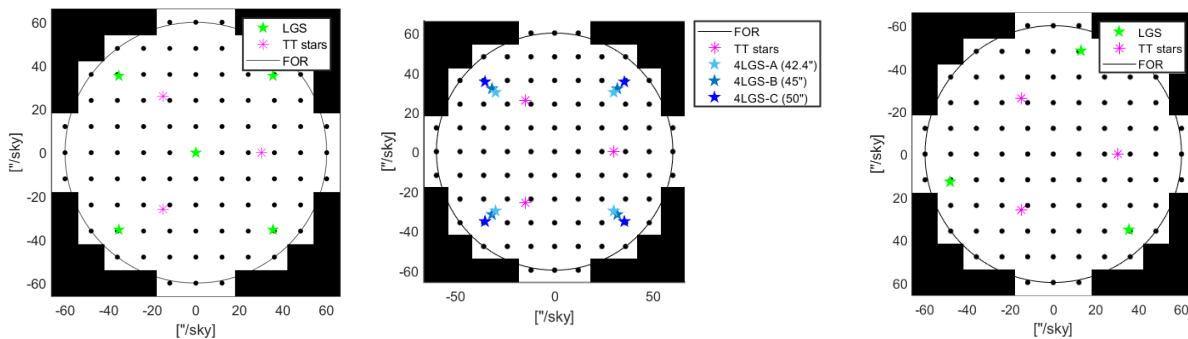


Figure 63: Science (black), LGS (green, blue) and TT stars (magenta) positions within the GIRMOS FoV. Left: 5LGS configuration. Center: 4LGS-A, 4LGS-B and 4LGS-C configuration. Right: 4LGS-T configuration.

#### 3.4.3.1 5LGS

This was the initial configuration assumed during the preliminary phase of the MOAO design. There is 1 central LGS and 4 LGS located at a radial distance of 50 arcsec in a square.

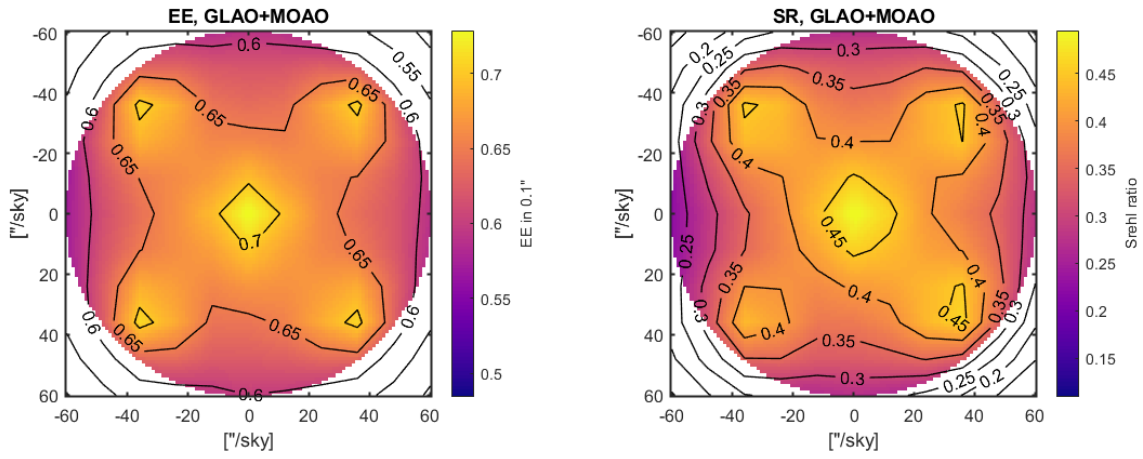


Figure 64: EE in 0.1'' (left) and SR (right) performances in H-band for the 5LGS configuration.



3.4.3.2 4LGS-A, 4LGS-B, 4LGS-C

4 LGS located at a radial distance of respectively 42.4, 45 and 50 arcsec in a square.

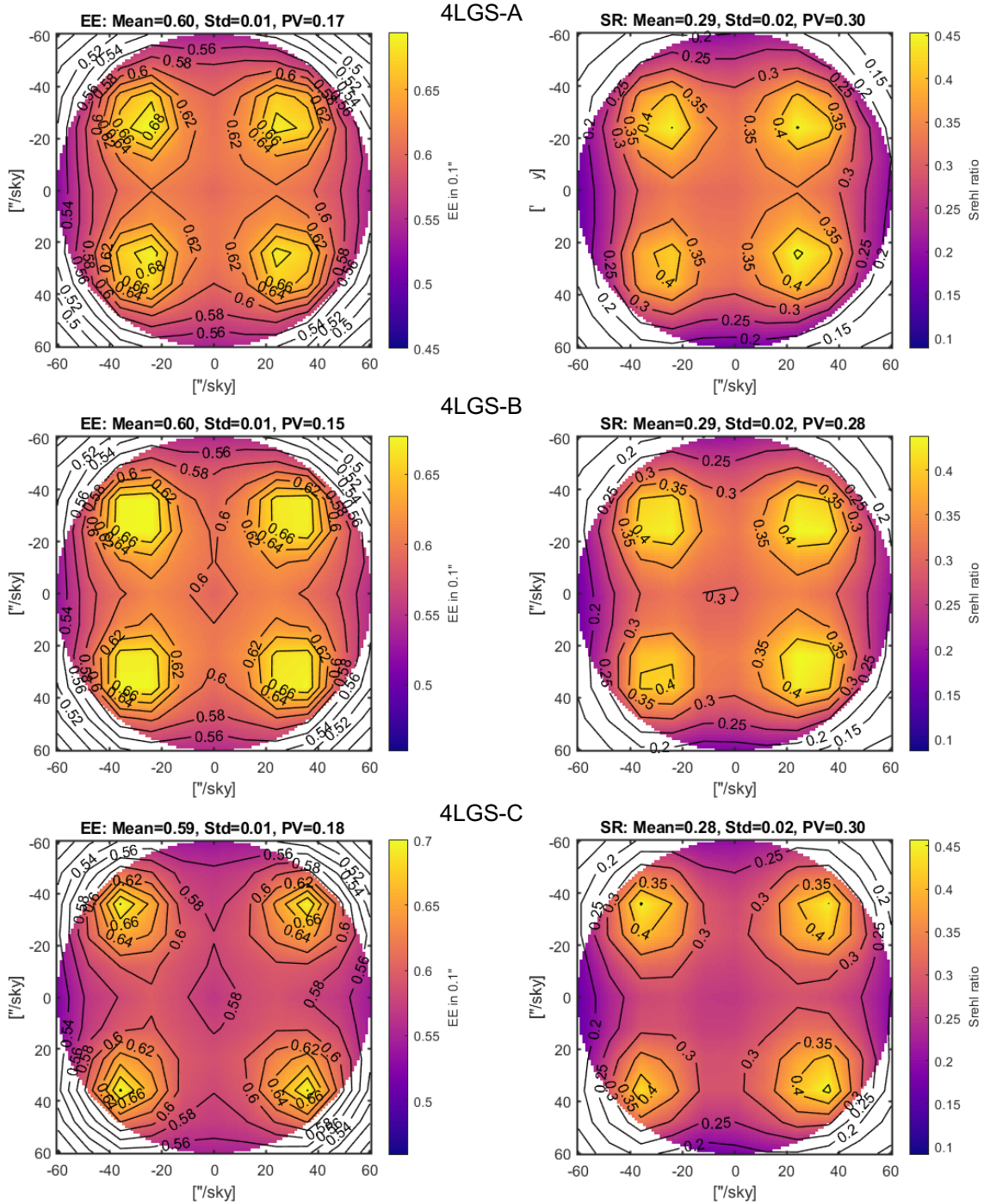


Figure 65: EE in 0.1" (left) and SR (right) performances in H-band for the 4LGS configuration, top line is for 4LGS-A, middle is 4LGS-B and bottom is 4LGS-C.

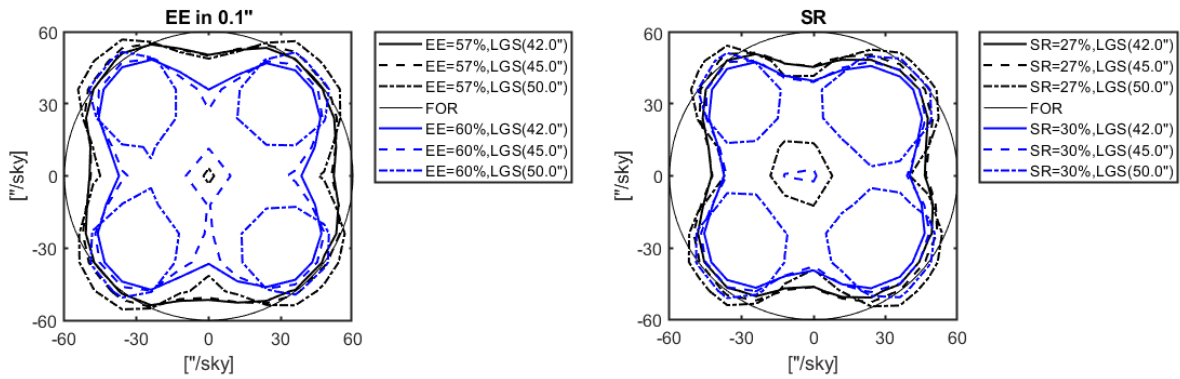


Figure 66: EE in 0.1'' (left) and SR (right) contours corresponding to 57%EE and 27%SR in black and to 60%EE and 30%SR in blue. The line style is for the 3 different 4LGS configurations (A, B and C).

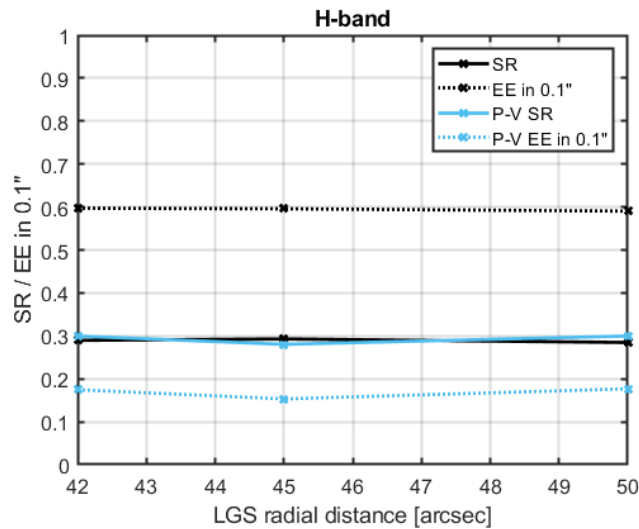


Figure 67: EE in 0.1'' and SR (black) and Peak to Valley (blue) values over the 2 arcmin FoV for different 4LGS radial distance (4LGS-A, B, C).

### 3.4.3.3 4LGS-T

### 3.4.3.4 Results

We present in this section the summary of the results obtained from simulation of the system for different LGS configurations. Considering the 4LGS configurations (only A, B, C, T being discarded by GNAO).

**Table 7: Reported GLAO-MOAO performance over the 2' FOV in H-band (1.65 $\mu$ m), assuming median seeing conditions at Mauna Kea and 30° zenith angle (1.5 Airmass).**

LGS configuration	EE <sub>0.1"</sub> , 2' FOV averaged [%]	EE <sub>0.1"</sub> , 2' FOV std [%]	SR, 2' FOV averaged [%]	SR, 2' FOV std [%]
5LGS	64	1	35	2
4LGS-A	59	1	28	2
4LGS-B	60	1	29	2
4LGS-C	60	1	29	2
4LGS-T	60	1	31	2

### 3.4.4 NCPA

We also explored the impact of uncorrected NCPAs on the performances. We simulated a random NCPAs map, essentially due to polishing errors using a series of 100 Zernike modes with their normalization following a  $f^{-2}$  power law. We ran the simulation and add the NCPAs on top each wavefront frame used to compute the long-exposure PSF. We repeated the operation for different amplitudes of NCPAs and the results are shown if Figure 68. We can see that the EE and SR are not strongly affected (< 3% relative) for NCPAs' amplitudes smaller than 80nm RMS. This result is very encouraging and relaxes our requirement on NCPAs. To mitigate the NCPAs, we are planning to use a focal plane sharpening algorithm (Lamb et al. 2014), adapted for the GIRMOS IFU.

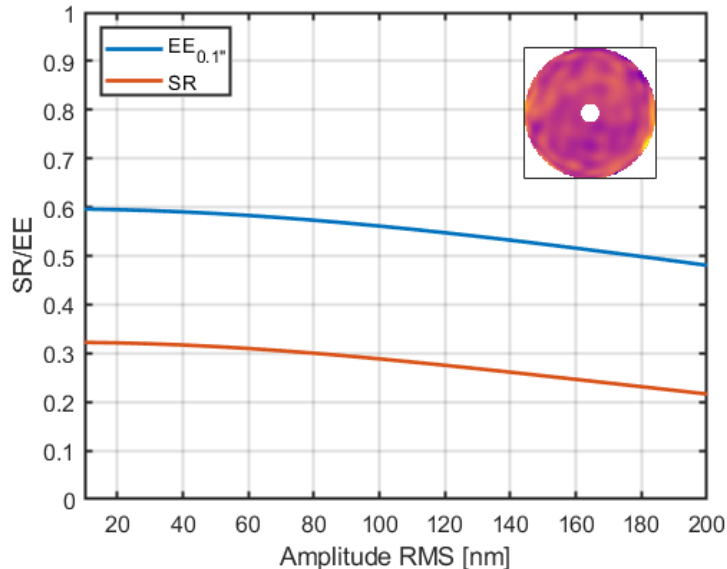


**Figure 68: EE<sub>0.1</sub> (blue) and SR (red) for different NCPAs (insert) amplitudes, in H-band.**

### 3.4.5 Error Budget

A preliminary High Order error budget was performed during the conceptual design phase assuming GeMS and not GNAO, more details can be found in [RD-08].

## 4 Manufacturing, Assembly, Integration and Tests (MAIT)

### 4.1 Manufacturing

Given the current mechanical design, there are no manufacturing concerns for the MOAO components. Most of the optical mounts are a combination of COTS components mated to easily fabricated mechanical mounts (brackets and baseplates). Some mounts have heritage in proven designs and as such GHOST, GPI and GRACES and as such pose little if any risks.

### 4.2 Preliminary MAIT flowchart

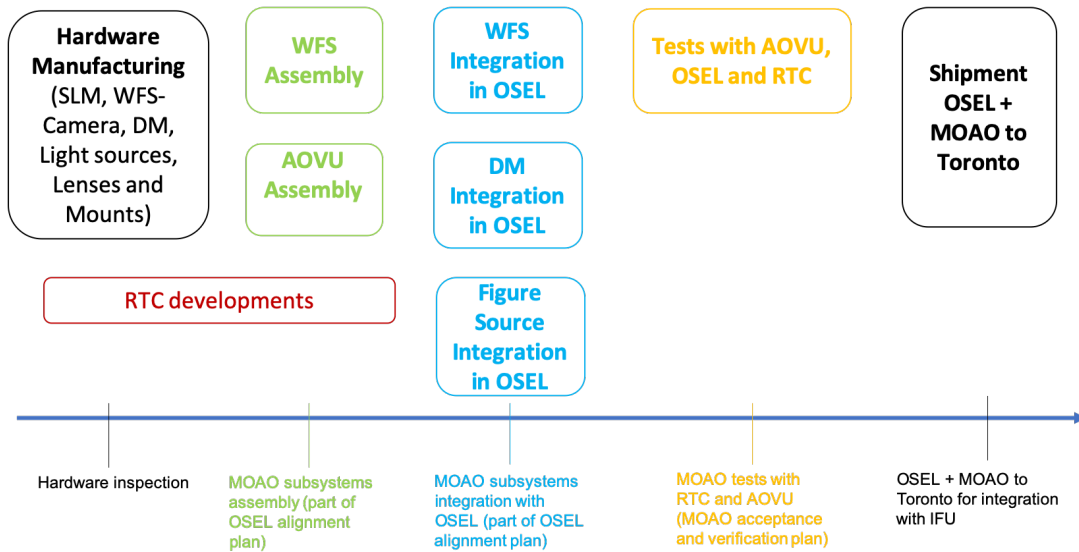


Figure 69: MOAO MAIT Flowchart.



Manufacturing, Assembly, Integration, & Test (MAIT) Flowchart Draft

GIRMOS - OSEL

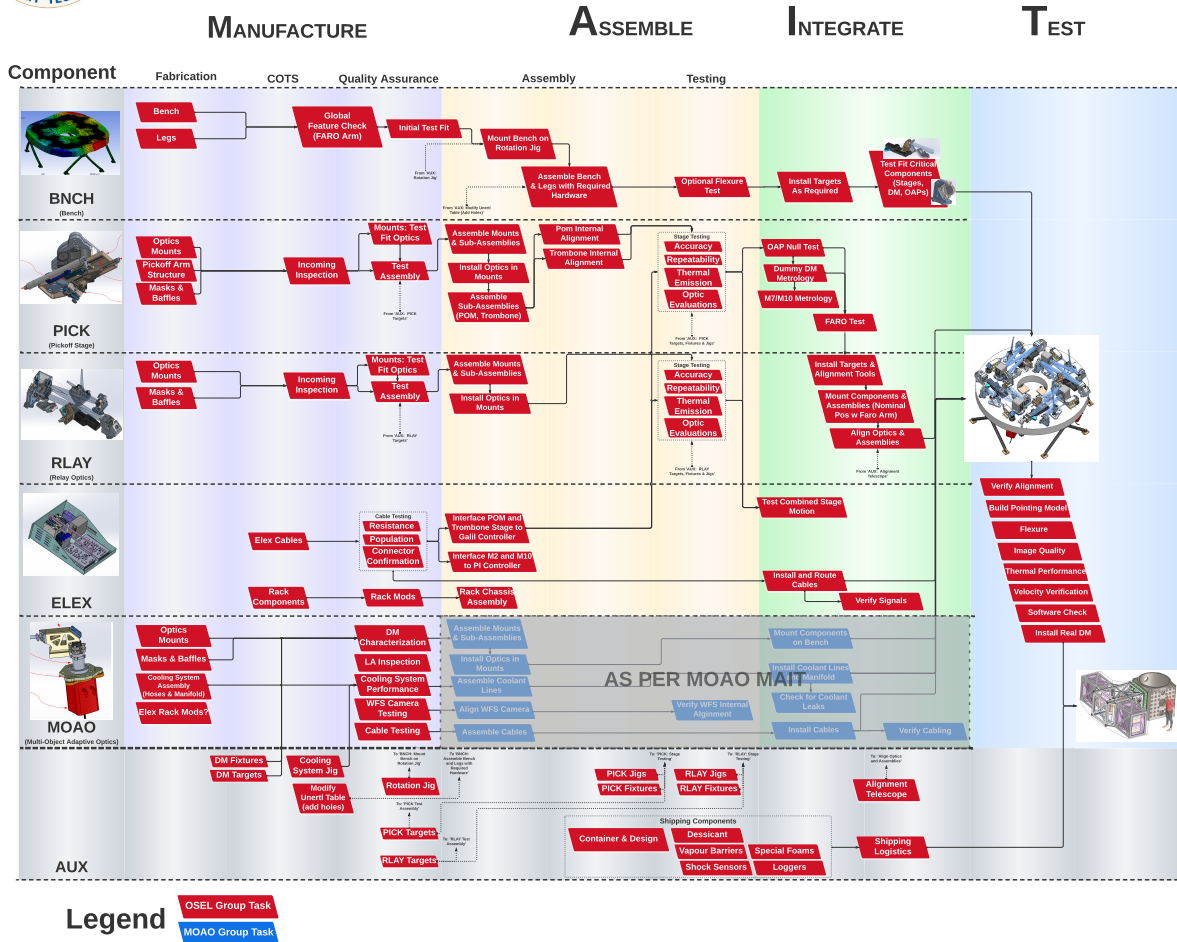


Figure 70: OSEL-MOAO MAIT Flowchart.

### 4.3 Long Lead Items List

Mechanically speaking there are no long lead or critical items. Here’s what I said for OSEL – MOAO is essentially the same (can’t talk to actual availability of things like the DM or WFS): All COTS components for the MOAO subsystem are currently readily available within the defined timeframe for long lead. In addition, for the custom mounts, material (6061-T6 aluminum) not taken from stock has a typical lead time of 1 – 2 weeks.

The only lead item is the DM (about 6 months for the production).

### 4.4 Preliminary Integration Plan

#### 4.4.1 Tools

The alignment of MOAO will need tools already owned by NRC and also used for OSEL alignment, as shown in Figure 71 and Figure 72:

- Alignment telescope (AT) (x1) with a retro-reflective target and 4-DOF mount.
- RAVEN cone targets (x2) on Thorlabs SB1 magnetic bases (x10)
- A Point-Source Microscope (PSM) (x1)
- A 150mm diameter lambda/10 (goal lambda/20) flat mirror on a tip/tilt mount.
- A portable CMM, such as a Faro arm (x1)
- A Spindle mirror target (SMT) (x1)
- A paper target on X-Y stage with 2 digital micrometers (Newport DMH-1) (x1)

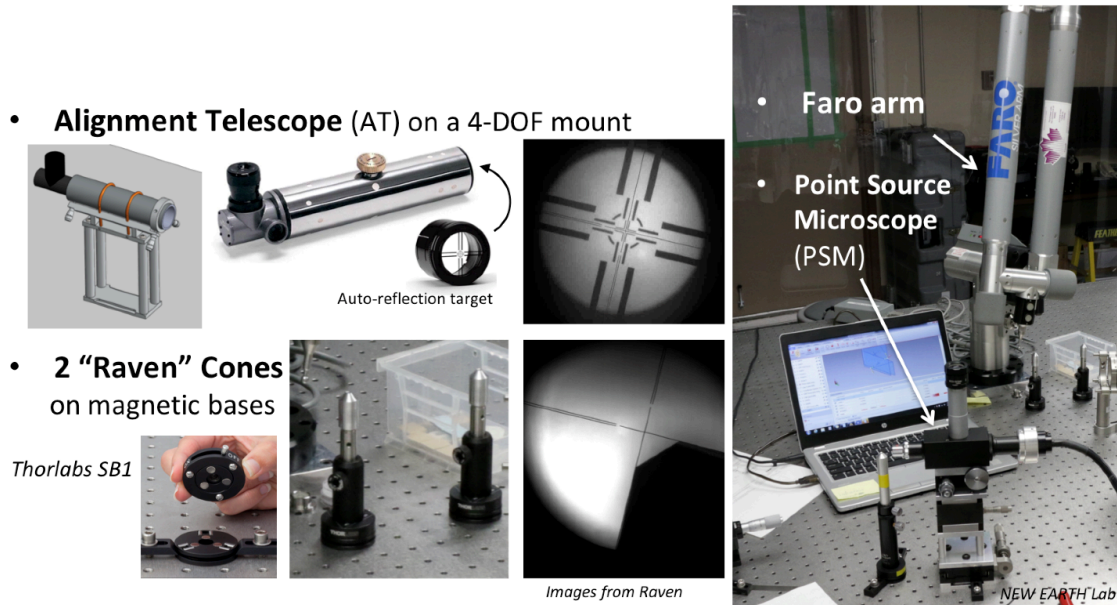


**Figure 71: Alignments tool required for MOAO.**

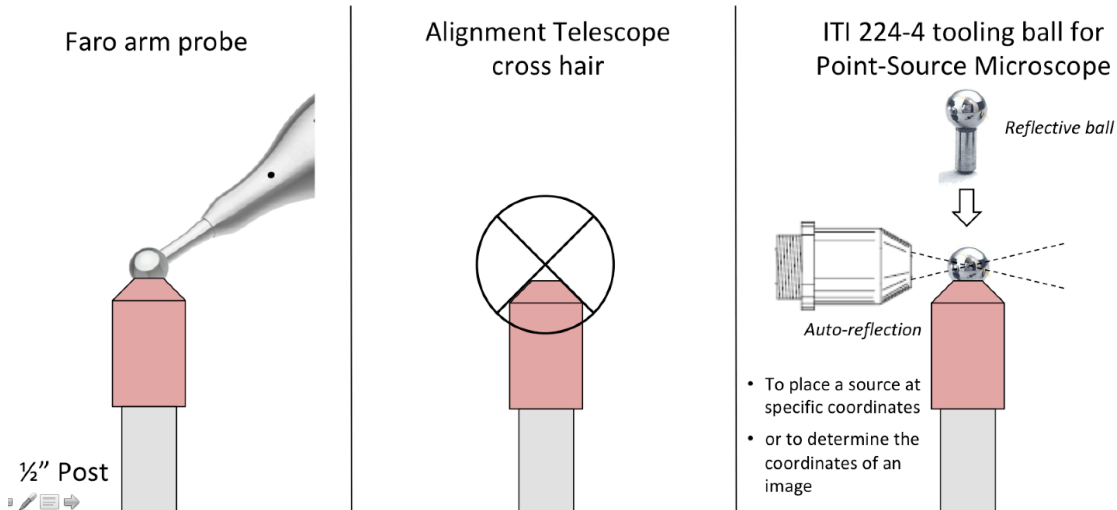


**Figure 72: A RAVEN cone enables interchangeability between Faro arm, Alignment Telescope and Point-Source Microscope.**

#### 4.4.2 WFS Sub-assembly Offline Alignment (Prior to integration)

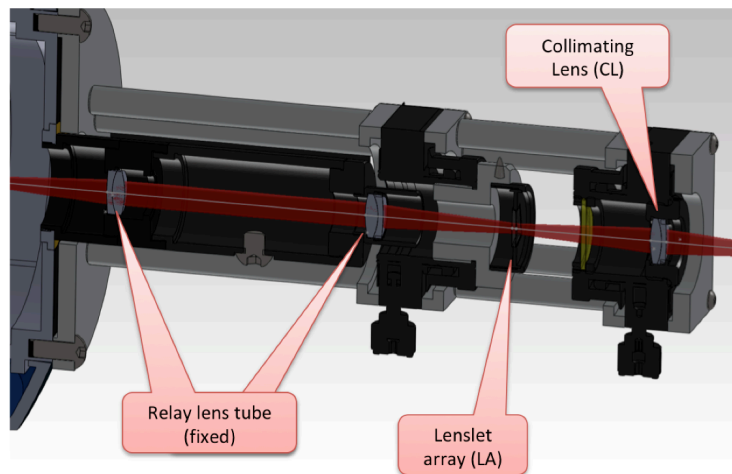
A view of the WFS assembly, as designed for RAVEN (same concept than OSEL WFS), is depicted in Figure 73. The goals of this alignment are:

- Center and clock Lenslet Array (LA) wrt detector pixels
- Focus LA spots on detector
- Center and Focus Collimating Lens (CL) to have LA conjugated to infinity.
- Report distance from focus to WFS assembly body.

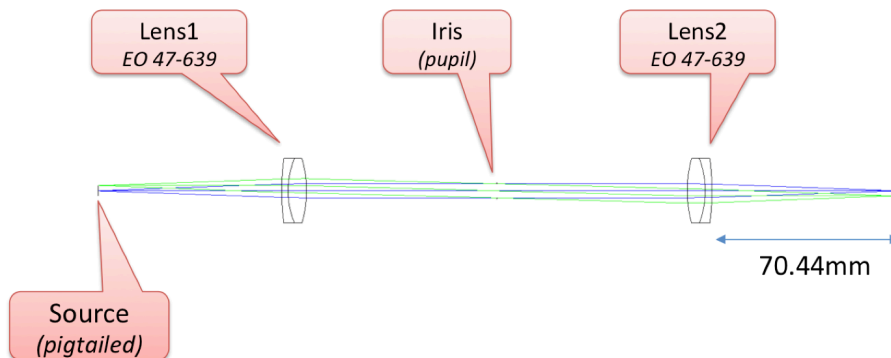
An alignment source tool is required to illuminate the WFS assembly with a F/14.4 focus and exit pupil at infinity like does OSEL. This tool is a telecentric 1:1 relay lens made of COTS parts as shown in Figure 74. This tool already exists as it was used for RAVEN.

Assumptions and prerequisites:

- The camera is fixed (reference)
- The tool is internally aligned
- Tool translation stage is assumed to be parallel with camera optical axis
- The tool is at the nominal distance from Camera

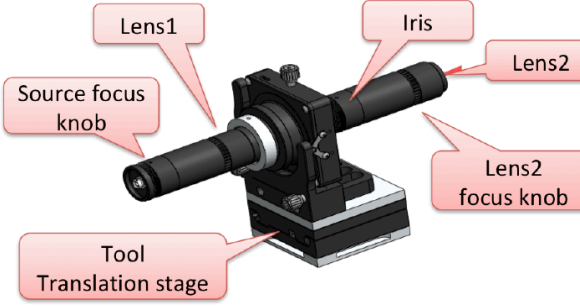
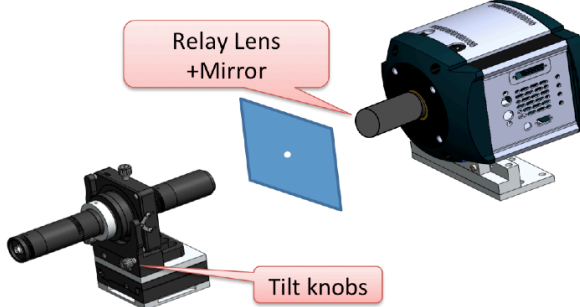
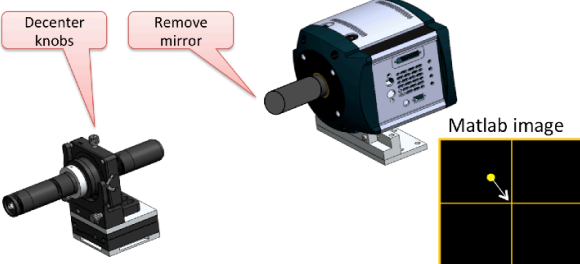
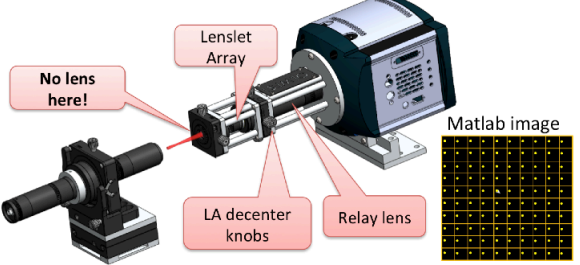


**Figure 73: WFS assembly as designed for RAVEN (same concept than MOAO WFS).**



**Figure 74: Alignment source tool use for the internal alignment of the WFS assembly.**

The procedure to internally align the WFS assemblies before integration in OSEL is as follows:

<p><b>Step 0 - Tool Collimation</b></p> <p>Goal: Exit pupil @ inf., inner-beam collimated.</p> <ol style="list-style-type: none"> <li>Adjust focus on a Alignment Telescope (AT) to <math>\infty</math> by autocollimation</li> <li>Remove Source and Lens1, place tool in front of AT, Lens2 toward AT</li> <li>Adjust Lens2 focus so that the Iris edges appear sharp in AT (the pupil is now at infinity)</li> <li>Remount Source and Lens1, Remove Lens2 and open Iris to max</li> <li>Adjust Source focus so that you can see Airy rings (the inner-beam is now collimated)</li> </ol>	
<p><b>Step 1- Tilt adjustment of the Tool</b></p> <p>Goal: Make Tool axis and Camera axis parallel</p> <ol style="list-style-type: none"> <li>Remove Lens2 from Tool and screw mirror on the camera C-mount thread</li> <li>Insert the hole screen</li> <li>Tilt the tool to superimpose the hole and the reflected spot</li> <li>Optional: Repeat this test with Lens2 on and iris almost closed (if the reflected spot is off the hole, check the internal alignment of the tool!)</li> </ol>	
<p><b>Step 2- Centration of the Source-Tool</b></p> <p>Goal: Make Tool axis and Camera axis colinear</p> <ol style="list-style-type: none"> <li>Remove the mirror</li> <li>Close the iris to make a pinhole, remove Lens2</li> <li>Adjust the tool decenter knobs to center the spot on the CCD (Use AlignAndorWfs.m and itRaw timer to display the image w/ a crosshair and the centroid position)</li> </ol>	
<p><b>Step 3- Lenslet Array focus &amp; clocking</b></p> <ol style="list-style-type: none"> <li>Screw relay-lens and LA on the camera, but remove collimating lens</li> <li>Open iris to max, remove Lens2</li> <li>Focus LA spots on CCD (use AlignAndorWfs.m and itSpots timer for gaussian fit and FWHM and Max computation)</li> <li>Clock the LA to align spots w/ pixels</li> </ol>	



<p><b>Step4 - Collimating Lens focusing</b>                  Goal: Put the Lenslet Array at infinity (seen from the front)</p> <ol style="list-style-type: none"> <li>Insert a 45deg mirror between tool and WFS to look at the LA with AT</li> <li>Adjust the focus of the CL to get a sharp image of the LA on AT reticle</li> </ol>	
<p><b>Step 5- Collimating Lens (CL) &amp; LA Centration</b></p> <ol style="list-style-type: none"> <li>Screw the collimating lens in front of the LA. Screw lens2 on Tool</li> <li>Reduce the Iris size to about 3x3 subap</li> <li>Adjust the CL decenter knobs to center the beam footprint on LA (use AlignAndorWfs.m and itSpot timer for lenslet intensity and pupil centroiding)</li> <li>Open the Iris and Adjust LA centration to get no tip/tilt error</li> </ol>	

### 4.4.3 AOVU Sub-assembly Offline Alignment

- Define optical axis and foci w/ 2 cones per segment placed w/ Faro
- Align AT on C1/C2
- Nudge SLM (Power on with factory flat) to align C3/C4/C5 on AT
- Install return flat on C2 and autocollimate w/ AT
- Insert lens1 and adjust in XYZ to center and focus return spot in C3/C4
- Align AT on C3/C4
- Install return flat on C3 and autocollimate w/ AT
- Insert lens2 and adjust in XYZ to center and focus spot in C4
- Insert lens3 and adjust in XYZ to center and focus spot in C5

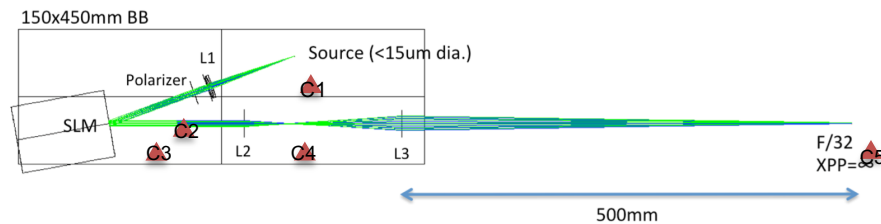


**Figure 75: AOVU path optical layout. with position of cones for alignment.**

### 4.4.4 WFS Path Alignment Steps

Once the OSEL science path optics are aligned, we can align the WFS path front (i.e. Figure source) and back ends:

Assumption:

- Dummy DM is still in place; otherwise, the DM shall be at its factory best flat command.
- Wavefront sensing software is ready and must produce a live display of WF TT and pupil XY centration errors.

Main alignment steps:

1. Survey component to nominal position in XYZ with Faro arm
2. Turn on Figure Source (FS)
3. Tilt FS fold to center FS in FSM located at IF (FS is expected to be bright enough to be seen after reflection on M10, if not, put a white source behind pinhole)
4. Nudge FS in Z to get a focused image in the PSM
5. Install pre-aligned WFS assembly to nominal position
6. Tilt WFS fold to center pupil footprint on detector (CL and LA are already aligned w.r.t. detector)
7. Adjust WFS assembly DX/DY to null TT read by WFS.
8. Adjust WFS Z to null focus read by WFS (if easier move both WFS fold and assembly laterally).
9. Repeat Steps 6 to 8 if needed.
10. If a white source has been used, install real FS and repeat Step 6 to 8 in case the switch had perturbed pinhole position.

#### 4.4.5 Real DM integration

This sequence is required when the time to switch the dummy DM with the real DM comes. Both science and WFS paths need to be aligned first, and the wavefront sensing software working.

1. Make sure FS WFS reads zero TT and zero pupil shifts.
2. Install AT after IF, realign it on C5 & C6
3. Remove dummy DM. Install real DM to nominal position (including half pitch shift as shown in Figure 5-10). Send factory best flat.
4. Tilt DM mount to center C5 on AT
5. If needed, nudge DM in Z to recenter C6 on AT. Repeat steps 4 & 5.
6. Fine-tune DM tilt and Z position when looking at FS WFS (null TT w/ DM TX/TY, null pupil shift with DM Z)
7. Poke 3 actuators. Measure registration errors (DX,DY,TZ) w/ FS WFS.
8. Clock DM to WFS (or vice-versa)\* to null TZ registration error.
9. Adjust DM X/Y to null DX/DY registration errors.

\*at the telescope, DM will be clocked to GNAO DM, then WFS will be clocked to DM.

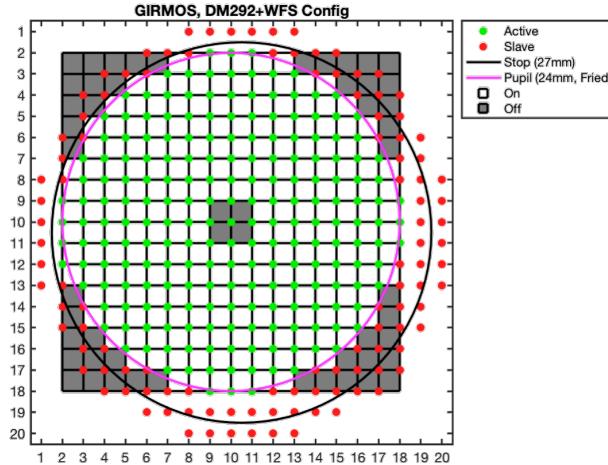


**Figure 76: The real DM must be shifted by half an actuator pitch (i.e., 0.75mm) in X and Y w.r.t. the optical axis in order to put an actuator on-axis and have 17 actuators across the beam.**

## 4.5 Preliminary Quality/PA Plan

Here we describe what we will do to ensure the components we use for MOAO meet the quality that we require. These include manufacturer test reports, and direct measurements. The MOAO group is responsible to carry out the tests.

### Deformable Mirrors.

Test reports from ALPAO, similar to that presented below, describe the performance upon manufacture. We are still in discussion with ALPAO about dead actuators, the effect on our performance, and the causes of the dead actuators to ensure this will not be a developing problem. We will seek a contract that ensures a maximum number of dead actuators (2 based on simulations in Appendix C), guaranteed over a 10 yr period, with a clause to fix or replace should this number be exceeded.

DM performance will be assessed by the MOAO group on the TBED-V2 bench, using a similar series of tests described above for the existing TBED setup.

### WFS cameras.

Similar test reports from Andor will be available upon procurement of the WFS cameras.

The contract for the CMOS cameras includes a guarantee for maximum dark current performance over a 10yr period.

WFS performance will be assessed by the MOAO group on the TBED-V2 bench, using a similar series of tests described above for the existing TBED setup.

## ■ COMPLIANCE MATRIX

The table hereafter summarizes the compliance test results of your ALPAO Deformable Mirror.

Property	Specification*	Result	Unit	Pass/Fail
Mirror best flat, residual error	<7	3.5	nm RMS	Pass
Wavefront 3x3 stroke	>10	24.6	μm PV	Pass
Wavefront tip/tilt stroke	>15	29.1	μm PV	Pass
Wavefront defocus stroke	>10	63.1	μm PV	Pass
Wavefront astigmatism stroke	>10	22.8	μm PV	Pass
Linearity	<3	0.01	%	Pass
Hysteresis	<2	0.51	%	Pass
Peak frequency	>2000	1594	Hz	Pass
Frequency at -45° phase	>1500	1598	Hz	Pass
Settling time	<0.5	0.29	ms	Pass

*\*Standard specifications*

**Figure 77: ALPAO DM292 compliance list from the test report delivered for the first DM procurement on March 14, 2022.**

### 4.6 Handling and Test Equipment (H&T)

## 5 Future Phases

Here we discuss staffing, risk, and overall budget. This is intended to give context on what is required for success with the MOAO system.

### **CDR**

The CDR phase represents the main prototyping and risk retirement phase for the MOAO system. A preliminary prototyping and risk retirement was undertaken in PDR as described above, consisting of a model MOAO arm (TBED) using different hardware from that intended for GIRMOS, and the initiation and planning of an on-sky open loop test on the REVOLT experiment.

CDR will see a full integration and testing of a prototype GIRMOS MOAO arm on the TBED platform, using the intended hardware (ALPAO DM292 and CMOS-based WFS). This 'TBED-V2' will see the preliminary RTC implemented with the hardware, and a series of more rigorous tests performed on the TBED-V2.

CDR also represents a major development phase for the GIRMOS RTC contract with NRC.

### **Staffing:**

Over the 18mo of CDR, we have allocated 2.5 FTE years of postdoc effort to MOAO work.

### **Risk:**

The CDR phase retains some risk related to the performance of the MOAO, and continued evolution of the GNAO optical bench specification and design. At the end of CDR, the GNAO design should be mature and finalized, while our main risk mitigation activities will be completed (TBED-V2 and REVOLT-OL).

### **Overall Budget:**

As described in Fig.75, the CDR phase has budgeted for 2.5 FTE years of postdoc effort (\$200,000) coming entirely from operation and maintenance funds working on the working test experiments (TBED-V2 and REVOLT-OL). RTC contract work at \$312,000, and mechanical engineering work at \$21,000, for a total of \$333,000. In addition, \$30,000 in non-labour (hardware for TBED-V2 and REVOLT-OL) have been allocated.

### **MAIT**

The MAIT phase for MOAO consists of first implementing the TBED-V2 prototype arm on the GIRMOS optical bench, integrated with the OSEL subsystem. In parallel, the hardware for the other 3 arms will be procured, and then installed on the GIRMOS bench.

The MOAO hardware will be aligned and tested for basic functionality. The full testing phase will be done using the AOVU assembly to provide

### **Staffing:**

Staffing has been allocated for MAIT with 2.5 FTE years of postdoc effort, allocated through the 30mo of the MAIT phase.

### **Risk:**

There is little risk in the MAIT phase given that the prototype MOAO arm and RTC will have been fully tested using the AOVU in the CDR phase.

### **Overall Budget:**

As described in Fig.75, the MAIT budget includes 2.5 FTE years of postdoc effort divided between the 4 MAIT phases, and funds to procure one additional MOAO arm. The 3rd and 4th arms are not included in this budget, but are anticipated to come from a partner (likely South Korea) contribution.

The remaining RTC contract (hardware and labour) with NRC (\$200,000) is paid in this phase, along with \$21,000 in contracted mechanical work from NRC.

**Commissioning**

Staffing:

Staffing has been allocated for commissioning with 0.8 FTE years of postdoc effort, allocated through the 6mo of the phase.

Risk:

There is some risk in the commissioning phase given that this is the first implementation with GNAO on sky.

Overall Budget:

In commissioning, \$60,000 has been allocated for labour and \$5000 for travel.

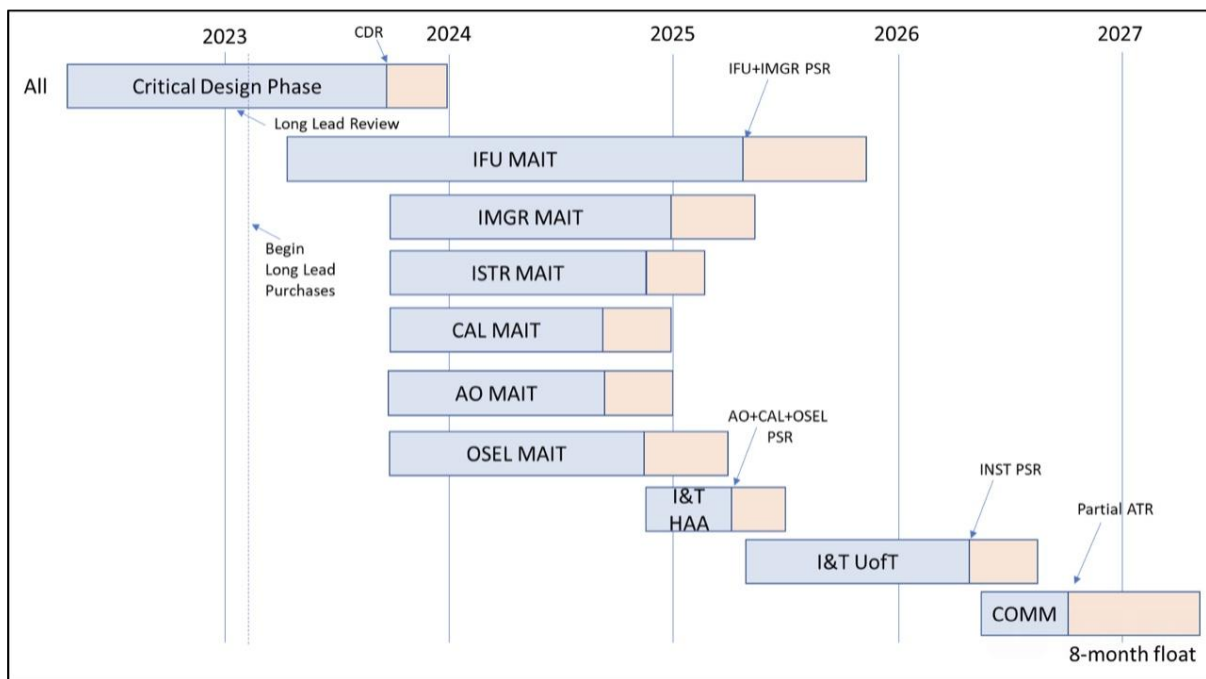


Figure 78: The AO schedule relative to other subsystems.

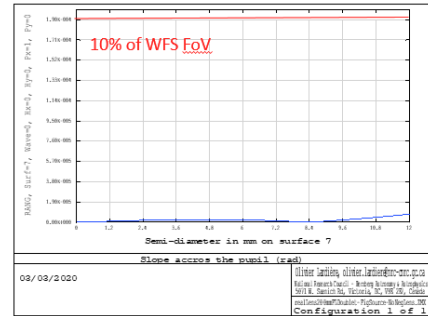
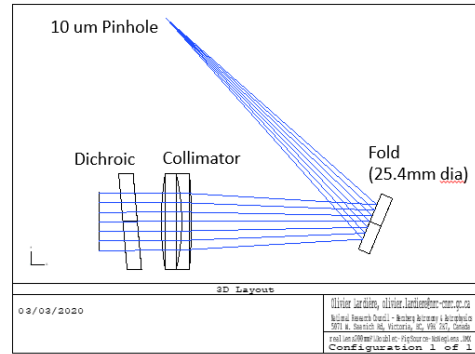
GIRMOS PROJECT PLANNING ESTIMATES									
SUBSYSTEM	PROGRAM PHASE		SUB-SYSTEM ESTIMATES						
	PHASE	NOMINAL DURATION (Months)	DURATION EST. (Months)	DURATION FLOAT EST. (Months)	LABOUR COST BASE EST. (\$CAD)	LABOUR RISK EST. (\$CAD)	NON-LABOUR COST BASE EST. (\$CAD)	NON-LABOUR COST RISK EST. (\$CAD)	
[SUB-SYSTEM NAME]	CRITICAL DESIGN PHASE (CDR)		18 months	18	2	333000	66600	30000	3000
	PRODUCTION (MAIT)	MANUFACTURING	30 months (total)	12	2	171000	34200	372500	74500
		ASSEMBLY		2	0	16700	0	0	0
		INTEGRATION		8	1.6	67000	13400	10000	2000
		TESTING		8	1.6	67000	13400	10000	2000
	COMMISSIONING		6 months	6	2	60000	12000	5000	0

Figure 79: The MOAO budget in future phases from CDR to commissioning.

## Appendix A      Folded Figure Source Design

# Folded Figure Source design

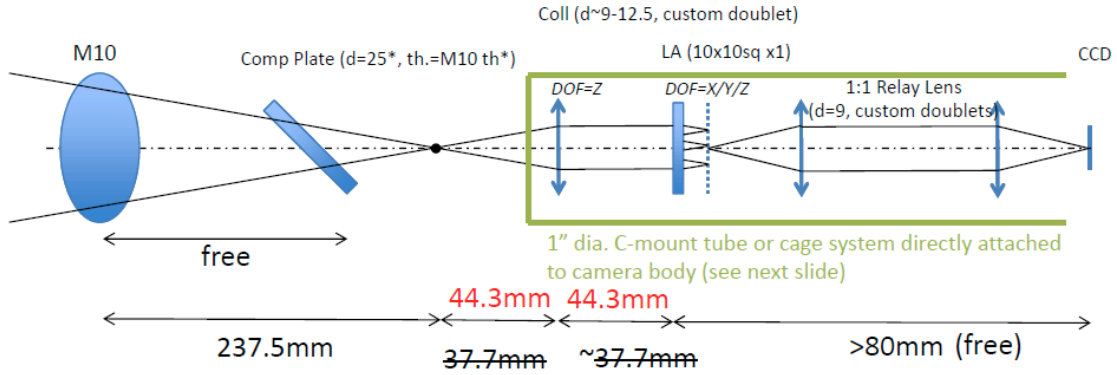
- LED assembly:
  - Thorlabs LED680L + diffuser DG1-120 + pinhole P10D
- Fold mirror (25.4mm dia.)
- Collimator + Mirror assembly:
  - Thorlabs AC508-200 (50mm dia, 200mm FL) or Edmund #49-383 (40mm dia, 200mm FL)
  - 6mm-thick fused silica dichroic or leaky mirror (T>2% @ 680nm, R>98% @ 950-2400nm)
- Notes:
  - Distance pinhole to (Edmund) collimator = 194mm
  - Distance between collimator and mirror doesn't matter.
  - Collimator and mirror can be stacked on the same mount.
  - Position and tilt of fold mirror do not matter.
  - Maximum pinhole diameter is 10um.
  - Allow ~20mm behind the pinhole to fit LED connector, LED itself and diffuser.



## Appendix B GIRMOS WFS Path

All dim. are in mm

### GIRMOS WFS Path



The path can be folded anywhere before the collimator

Camera DOFs= X,Y,Z,TZ (clearance holes and shims/nudgers)

\* Actual Dia. And thick. depend on axial position

LA could be mounted in 1" SUSS Microoptics mount ([part1](#) + [part2](#))



## Appendix C MOAO DM trade study

This section presents a trade study performed during the conceptual design phase (assuming GeMS instead of GNAO at that time). The goal was to identify the best technology and Vendor for the MOAO DM.

### C.1 Previous studies

The choice of the best DM for MOAO applications is not a new subject and some previous author already studied this problematic, see [RD-12], [RD-13], and [RD-14] and [RD-15]. We present here a summary of the previous studies.

In [RD-12], they investigated the state of the art DMs for an MOAO instrument concept (FALCON) and identified different possible issues (hysteresis, creep, ...) with DMs depending on the temperature and on the ageing. At the time of the study, no DMs were able to meet the FALCON's requirement but they noticed that electrostatic mirrors could fulfil their requirement provided that the stroke is enlarged. They pointed out that ongoing test with large stroke magnetic mirrors are promising.

In [RD-13], 3 different DMs (manufacturers and technologies) were tested and compared for open loop purposes for the CANARY experiment: OKO (electrostatic), ALPAO (magnetic) and CILAS (piezoelectric). The OKO mirror was not selected due to the very limited actuator stroke ( $\sim 0.2 \mu\text{m}$ ). ALPAO was identified as a potential promising manufacturer. The [RD4] study was performed with a 1<sup>st</sup> generation of ALPAO DM build in 2006 and found that the temporal bandwidth was too slow for their open loop applications. However, they noticed the progress made by ALPAO which is now able to deliver mirrors featuring  $\sim \text{kHz}$  bandwidth as demonstrated by the VOLT experiment. For CANARY, they selected the CILAS mirror (the one used for COME-ON). However, they noticed that an important effort has to be done to reduce hysteresis, creep, and to improve the repeatability of such piezoelectric actuators.

In 2014, the ALPAO Hi-Speed-DM241-25 was characterized for open loop purposes [RD-14]. More precisely the creeping and the hysteresis. In particular, they found that the DM is subject to creeping up to 30% of the RMS in the difference in shape before and after the flipping point. However, *"The deformation of the DM surface in time is repeatable and hence predictable. We demonstrate how to compensate for the deformation in software. We continuously adapt the actuator commands after the flipping point in such a way that they counterbalance the deformations of the DM surface"*, [RD-14]. For ALPAO, this creeping is due to the polymer in the springs, ALPAO now offers a new technology not subject to creep, [RD-14, RD-15].

### C.2 Simulations

A GIRMOS MOAO simulation of the system was performed with OOMAO Matlab Toolbox. Both GeMS working in GLAO mode and the open-loop DM of GIRMOS were considered here. From the simulation we can start to parametrize the open loop DMs requirements for the instrument. The GIRMOS AO performance requirement is  $\sim 50\%$  of ensquared energy (EE) within 0.1 arcsec in HK bands [RD-06, RD-07].

#### **Number of actuators:**

The number of DM actuators or system order affects the EE as we can see on Figure 80. To reach the AO performances requirement, a system order of minimum 16 is needed. And A system order  $> 20$  doesn't improve significantly the EE.

**Our first GIRMOS OL DM requirement is to have between 16 and 20 actuators across the pupil.**

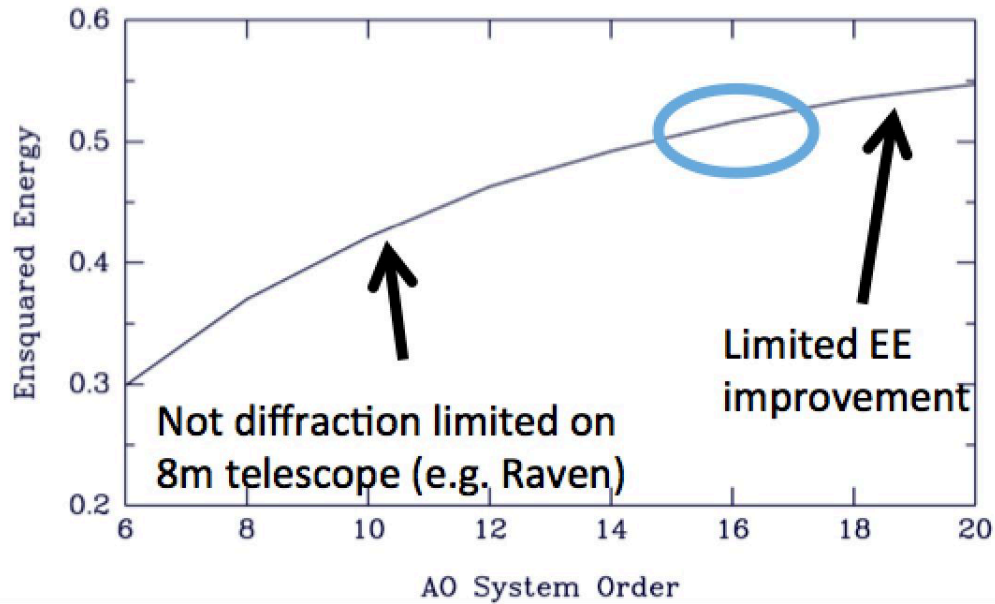
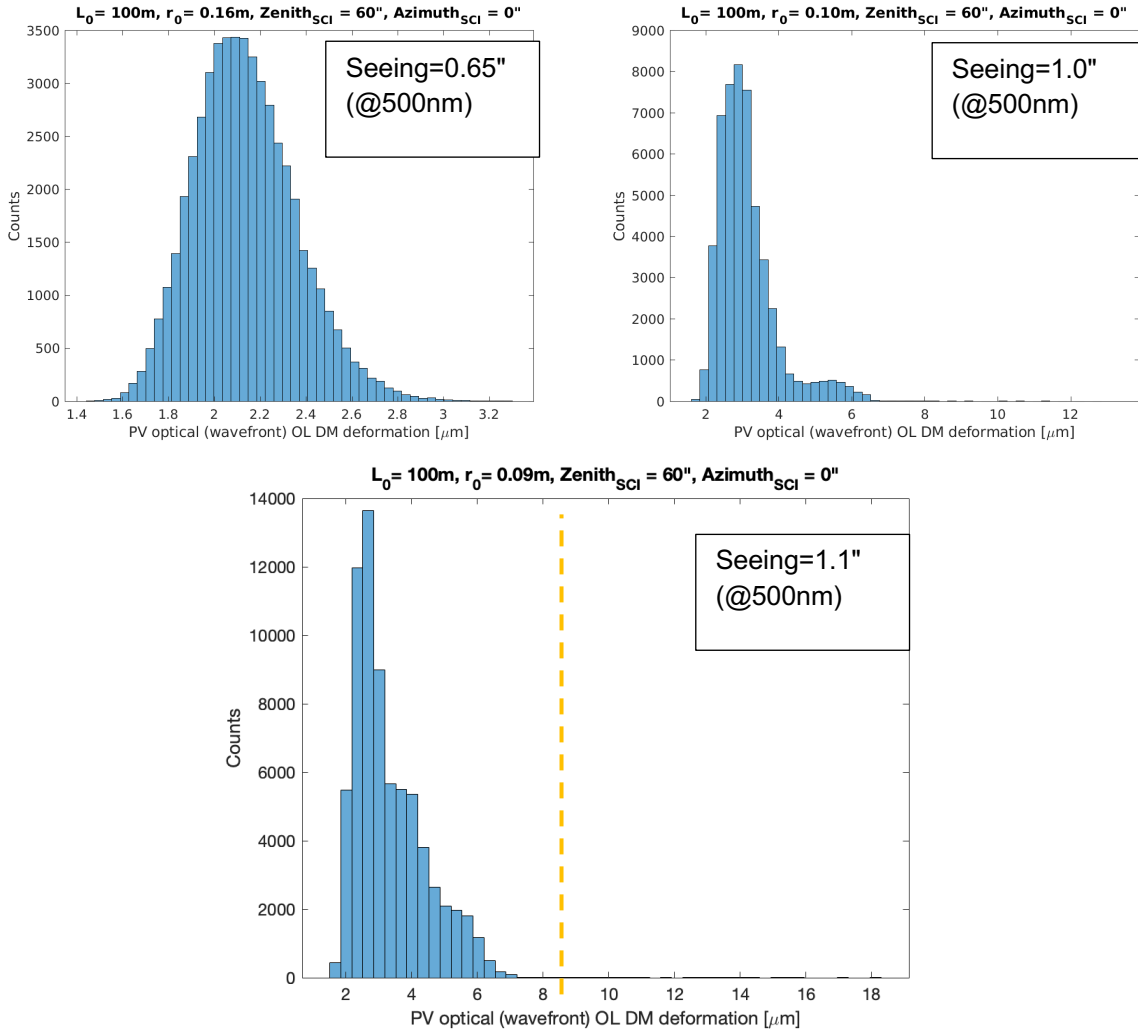


Figure 80: GIRMOS focal plane ensquared energy within 0.1" in function of AO system Order. From GIRMOS preliminary simulations presented in Chapman et al. 2018 [RD-07].

**Actuator stroke:**

The stroke needed for the open-loop DM is an important constraint for the choice of the DM manufacturer. From simulations, we extracted the OL DM stroke for different seeing ( $r_0$ ), external scale ( $L_0$ ) conditions as well as different zenith angles (0, 30" and 60") directions in the field. An OL DM order of 17 (same as GeMS) was considered here. Figure 81 shows the histogram of the OL DM actuators stroke for a  $r_0 = 0.09\text{m}$ ,  $L_0 = 100\text{m}$  and a zenith angle of 60", which are conditions where the OL DM requires a maximum stroke.

**The second GIRMOS OL DM requirement is to have a minimum of 8 $\mu\text{m}$  PV actuator stroke.**



**Figure 81: Histogram of GIRMOS open loop PV DM deformations recorded from simulations given in wavefront space, which is the one generally used by DM manufacturers.**

**Actuator pitch and pupil size:**

The actuator pitch is directly linked to the number of actuators and pupil size. At this level of the study, the GIRMOS optical design being not yet frozen, different actuators pitches and pupil size can be considered without affecting the EE performances.

**Settling time:**

The settling time will mainly affect the overall AO system delay. It has been shown that the delay doesn't strongly impact the EE performances, see Conod et al. 2016. Most of the DM actuators have now a settling time relatively short (<100µs), so, no simulation of the GIRMOS OL DMs settling time was performed and requirement derived.

**C.3 Manufacturers**

We present here the 3 main manufacturers on the DM market for astronomical applications: ALPAO, CILAS and BOSTON MICROMACHINES. More information on the different technologies (magnetic, piezoelectric, mems) used for the DMs can be find on the different manufacturer websites.

**ALPAO (Magnetic):**

		SIZING				QUALITY			STROKE			SPEED	
		Number of actuators	Pupil diameter (mm)	Pitch (mm)	Number of actuators across a diameter	Active best flat (nm RMS, mechanical)	Tip/tilt stroke (µm PV, wavefront)	Defocus/astig. stroke (µm PV, wavefront)	3x3 stroke (µm PV, wavefront)	Settling time (ms at +/-10%, any stroke)	First resonance of the membrane (Hz)	Frequency at phase lag of 45° (Hz)	Mechanical dimensions WxHxD (mm <sup>3</sup> )
DM69		69	10.5	1.5	9	7	60	40	25	0.8	800	700	52 x 74 x 22
DM97-08		97	7.2	0.8	11		80	40	25	1.5	400	300	52 x 74 x 32
DM97-15		97	13.5	1.5	11		60	40	25	0.8	800	700	52 x 74 x 22
DM97-25		97	22.5	2.5	11		40	30	25	1.5	600	500	70 x 90 x 30 <sup>3</sup>
DM97-50 <sup>3</sup>		97	45	5.0	11		40	30	25	1.5	600	500	120 x 120 x 40
DM192		192	21	1.5	16		15	10	10	0.5	2000	1500	70 x 100 x 80
DM241		241	37.5	2.5	17		40	30	25	1.5	600	500	91 x 113 x 27
DM292		292	27	1.5	20		15	10	10	0.5	2000	1500	70 x 100 x 80
DM468		468	33	1.5	24		12	10	10	0.5	2000	1500	90 x 110 x 120
DM820		820	45	1.5	32		12	10	10	0.5	2000	1500	100 x 120 x 120
DM3228 <sup>3</sup>		3228	93	1.5	64		10	8	8	0.5	2000	1500	150 x 180 x 180
LARGE SIZE DM <sup>3</sup>	DMX37	37	100	20	7		30	50	40	25	2	500	400
	DMX61	61	130	20	9	50		40	25	2	500	400	280 x 310 x 80
	DMX85	85	170	20	11	30		25	25	2	500	400	280 x 310 x 80

All ALPAO DMs feature non-linearity below 3%, hysteresis as low as 2% for DM and 6% for DMX.

Figure 82: ALPAO off-the-shelf DM characteristics (datasheet link: pdf).

**CILAS (Piezoelectric):**

CILAS actually doesn't provide off-the-shelf DMs. Here is the list of their DMs features:

- Maximum stroke for 3x3 actuators: from 10 µm to 20 µm PV wavefront
- Interactuator stroke: up to > 8 µm PV wavefront
- Low hysteresis: < 5 % over full range
- Actuator resonance frequency: from 10 kHz to 20 kHz
- No heat dissipation

Stack Array Mirror	Number of actuators	Pupil diameter
Woofer DM for Gemini Planet Imager	97	45 mm
DM for NAOS at VLT (ESO)	195	112 mm
High Order DM for Gregor Solar Telescope	256	50 mm
DM for AO at Gran Telescopio Canarias	373	140 mm
High Order DM for SPHERE at VLT (ESO)	1377	180 mm
Upcoming DM0 for TMT	3125	325 mm
Upcoming DM11 for TMT	4548	386 mm

Figure 83: CILAS references for astronomy (datasheet link: pdf).

On major issue with piezoelectric technology, is the dead or defective actuators. As example for the SPHERE instrument, a non-negligible number of actuators were defective since the procurement of the DM, thus affects the AO performances, the “dead” actuators being blocked at the same position, see Figure 84. Some others actuators are “slower” than others. Another potential issue with piezoelectric technology is the hysteresis which is relatively high (even if <5%) for open loop purposes.

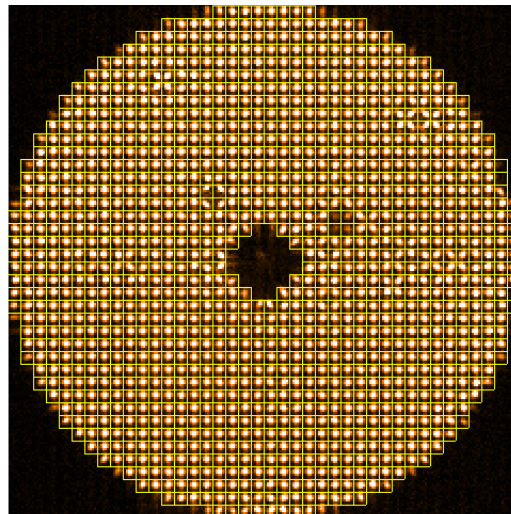


Figure 84: SPHERE Shack-Hartmann WFS image, we can distinguish the influence function of the SPHERE DM (made by CILAS with piezoelectric technology) dead actuators.

**Boston Micromachines (MEMS):**

## Low/Mid/High Actuator Count Deformable Mirrors

DM Specifications*	Total Actuator Count	Actuator Count Across Aperture	Stroke ( $\mu\text{m}$ )	Aperture (mm)	Pitch ( $\mu\text{m}$ )	Mechanical Response (10% - 90%)	Approximate Interactuator Coupling
Ultra-Compact Mini-1.5	25	5	1.5	1.2	300	<40 $\mu\text{s}$	15%
Mini-3.5	32	6	3.5	2.0	400	<75 $\mu\text{s}$	13%
Mini-5.5	32	6	5.5	2.25	450	<100 $\mu\text{s}$	22%
Multi-C-1.5	137	13	1.5	3.6	300	<40 $\mu\text{s}$	15%
Multi-3.5	140	12	3.5	4.4	400	<75 $\mu\text{s}$	13%
Multi-5.5	140	12	5.5	4.95	450	<100 $\mu\text{s}$	22%
Multi-SLM†	140	12	1.5	3.6	300	<35 $\mu\text{s}$	0%
492-1.5	492	24	1.5	6.9	300	<20 $\mu\text{s}$	15%
492-SLM†	492	24	1.5	10.2	300	<20 $\mu\text{s}$	0%
492-3.5	492	24	3.5	9.2	400	<80 $\mu\text{s}$	13%
492-5.5	492	24	5.5	10.35	450	<100 $\mu\text{s}$	22%
648-5.5	648	28	5.5	12.15	450	<100 $\mu\text{s}$	22%
Kilo-C-1.5	952	34	1.5	9.9	300	<20 $\mu\text{s}$	15%
Kilo-SLM†	1020	32	1.5	9.6	300	<20 $\mu\text{s}$	0%
Kilo-C-3.5	952	34	3.5	13.2	400	<80 $\mu\text{s}$	13%
2K-1.5	2048	50	1.5	19.6	400	<75 $\mu\text{s}$	15% ( $\pm 5\%$ )
2K-3.5	2048	50	3.5	19.6	400	<75 $\mu\text{s}$	15% ( $\pm 5\%$ )
2K-SLM	2048	50	1.5	19.6	300	<75 $\mu\text{s}$	0%
3K-1.5	3063	62	1.5	18.3	300	<75 $\mu\text{s}$	15% ( $\pm 5\%$ )
4K-3.5	4092	64	3.5	25.2	400	<100 $\mu\text{s}$	13% ( $\pm 5\%$ )

\*High speed driver options are available.

†Segmented surface mirror. All other configurations have continuous surfaces.

= Low     = Mid     = High

Figure 85: BOSTON off-the-shelf DM characteristics (datasheet link: [pdf](#))

## C.4 Conclusion

From the simulation performed and the previous study on the subject, we derived the main GIRMOS OL DM requirements:

- **Between 16 and 20 actuators across the pupil**
- **A minimum of 8 $\mu\text{m}$  PV actuator stroke**
- **Low hysteresis**
- **Low creeping**

Not all the manufacturers are reaching these requirements and especially BOSTON MICROMACHINES, their DMs have a maximum stroke of 5.5  $\mu\text{m}$ . Also, the number of actuators required for GIRMOS doesn't fit with the off-the-shelf BOSTON DMs list, see Figure 85.

Today, CILAS seems to meet the stroke requirement. However, CILAS doesn't deliver off-the-shelf DMs, which can delay significantly the procurement. Another issue is the dead or defective actuators which seems to append with such DMs technology as well as the hysteresis.

ALPAO DMs have enough stroke and seems well suited for open loop purpose. Previous characterization of these devices pointed out a creeping issue. We can notice that ALPAO is now using a new technology avoiding creep.

The Adaptive optics system of GIRMOS will be developed at HAA, which has a strong and long-time expertise in working with ALPAO DMs.

Moreover, the RAVEN project (Open loop demonstrator instrument on an 8m-class telescope) was developed with University of Victoria and HAA, and used ALPAO DMs (old technology with creeping!).

In addition, the use of off-the-shelf components proved to be a safe way to overcome an accident in the course of the project.

**ALPAO DM292 (new technology without creep) is therefore our baseline for the GIRMOS OL DMs.**

## Appendix D MOAO WFS trade study

### D.1 MOAO wavefront sensors requirements

We summarized here the MOAO WFS requirements extracted from the MOAO Level 2 Sub-System Requirements [AD-03] document.

**WFS order: [REQ-MOAO-0190]**

The WFS number of subapertures across the pupil shall be the same as the DM-1, i.e. 16 subapertures across the pupil diameter.

**WFS wavelength range sensitivity: [REQ-MOAO-0200]**

The WFS shall be sensitive to visible wavelength (0.78-0.95 $\mu$ m).

**WFS frame rate: [REQ-MOAO-0210]**

The WFS shall be able to acquire images at the GNAO AO speed loop, i.e. a 500Hz frame rate.

**WFS field of view: [REQ-MOAO-0220]**

The WFS lenslets FOV shall be at minimum 1.2+X", with X coming from simulations (including differential refractive index at MK and no GNAO correction)

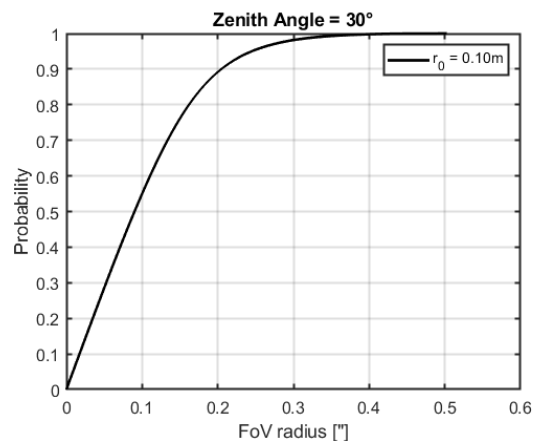


**Figure 86: Cumulative distribution photons from WFS spots as a function of field radius for  $r_0=10$  cm.**

**WFS spots sampling: [REQ-MOAO-0230]**

The WFS spots shall be sampled at a minimum of 2 pixels per FWHM (diffraction limited PSF) at  $\lambda=0.78\mu$ m. Note that this requirement is independent of the camera's choice and will mainly affect the lenslet array design.

**Truth-WFS mode (GLAO + MOAO Mode) : [REQ-MOAO-0330]**

When operating in GLAO+ MOAO, the MOAO shall provide an additional slow closed-loop using the MOAO WFS and the science target. **Note that this mode doesn't have any magnitude limit and frame rate requirement derived from the science requirements.**



## D.2 Cameras performances

We proposed here an overview of the different camera performances. In particular, we are interested in the sensitivity of the cameras for the truth sensing mode (see, section 0). For the figure source mode and the calibration of the system using the GNAO calibration light source, we are not concerned about a possible lack of photons, i.e. the sensitivity of the camera.

We first present the expected wavefront sensing performance of 2 EMCCD as well as 4 sCMOS based cameras allowing a 500Hz framerate for a 128x128 pixels region of interest (ROI). The advantages of using a sCMOS based cameras are essentially, the price, the size of the cameras, the lower power consumption, and the lower cooling compared to EMCCDs cameras, despite a lower QE and slightly higher readout noise (RON). Note that the dark current for some sCMOS models is comparable with EMCCD.

For each camera, we computed the signal to noise (SNR) obtained within one subaperture in one frame. We describe here how we computed the SNR. First, we have to determine the transmission of the system, and here we assumed a system including the atmosphere, telescopes mirrors, lenses, detector QE and an additional filter (0.80-0.95  $\mu\text{m}$ ). We can now compute the number of photo-electrons per subaperture per frame according to different object magnitude and integration time. Once we have the number of photo-electrons, we can finally compute the SNR according to the following equation:

$$SNR = \frac{n_{ph-e}}{\sqrt{\sigma_{shot}^2 + \sigma_{ron}^2 + \sigma_{dark}^2}} = \frac{n_{ph-e}}{\sqrt{(n_{ph-e} + n_{pix} * ron^2 + n_{pix} * t * dark)}}$$

Where  $n_{ph-e}$  is the number of photo-electrons,  $\sigma_{shot}$  is the shot noise,  $\sigma_{ron}$  is the readout noise,  $\sigma_{dark}$  is the dark current associated noise,  $n_{pix}=64$  is the number of pixels in a subaperture (8x8 pixels),  $t$  is the exposure time.

### **Andor: Ixon 860 (RAVEN)**

The initial idea was to refurbish the Ixon 860 cameras from RAVEN, for the cost, and also because these cameras are still well suited for the GIRMOS WFS. Note that these cameras are being deployed on the GIRMOS TESTBED with a 16x16 lenslet array. The Ixon 860 is an EMCCD (with the associated excess noise which is equivalent to double the shot noise) based camera with a very high QE, a very low RON and low dark current. The detector has 128x128 pixels.

**Table 8: Ixon 860 specifications**

Read noise (e-) Median	0.5
Dark current, (e-/pixel/sec)	0.002
Maximum power consumption (W)	26 + 30 (PCIe board)

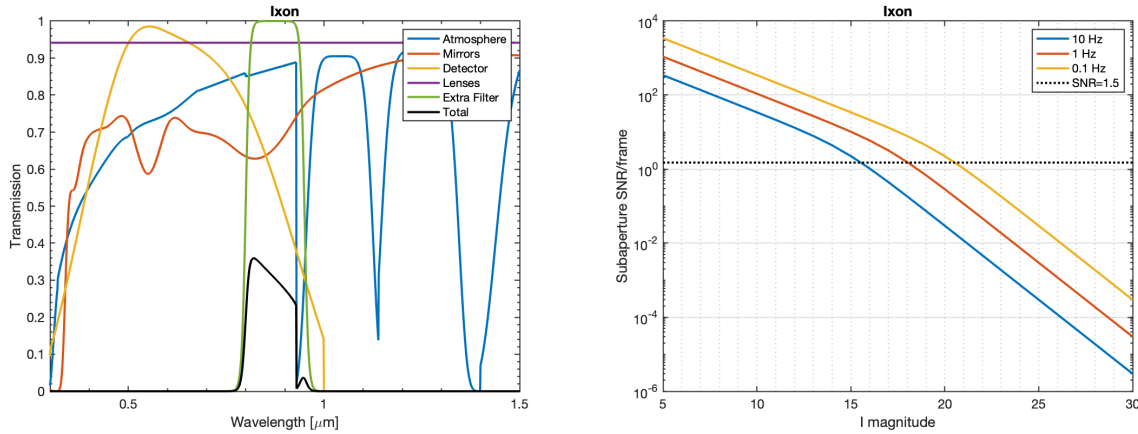


**Figure 87: Left: Transmission of the system including the Ixon 860 camera QE. Right: Subaperture SNR per frame for different object I magnitude. The colors represent different frame rate.**

**First Light: OCAM2K**

The OCAM2K is an EMCCD camera which is also well suited for the GIRMOS WFSs. The detector is 240x240 pixels.

**Table 9: OCAM2K specifications**

Read noise (e-) Median	0.5
Dark current, (e-/pixel/sec)	0.001
Maximum power consumption (W)	90

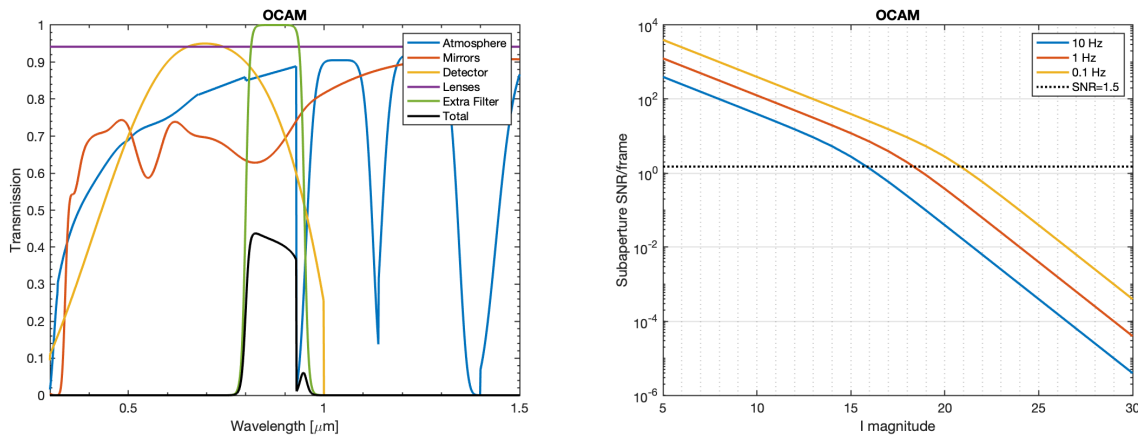


**Figure 88: Left: Transmission of the system including the OCAM2K camera QE. Right: Subaperture SNR per frame for different object I magnitude. The colors represent different frame rate.**

**Andor: Zyla 5.5**

**Table 10: Zyla 5.5 specifications**

Read noise (e-) Median	2.3
Dark current, (e-/pixel/sec)	0.019
Maximum power consumption (W)	60

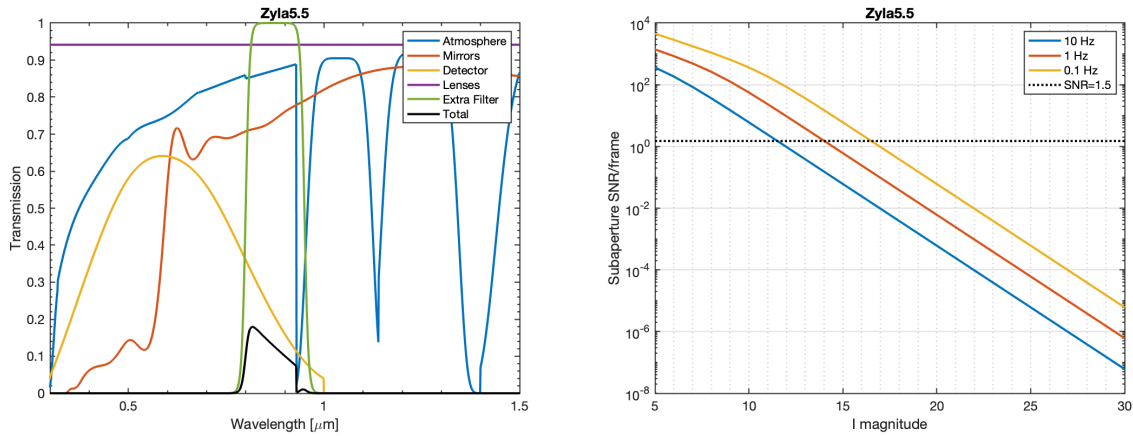


Figure 89: Left: Transmission of the system including the Zyla 5.5 camera QE. Right: Subaperture SNR per frame for different object I magnitude. The colors represent different frame rate.

**First light: C-BLUE**

**Table 11: C-BLUE specifications**

Read noise (e-) Median	3, is (2.3)
Dark current, (e-/pixel/sec)	0.6 (assuming a cooling down to 0°)
Maximum power consumption (W)	?

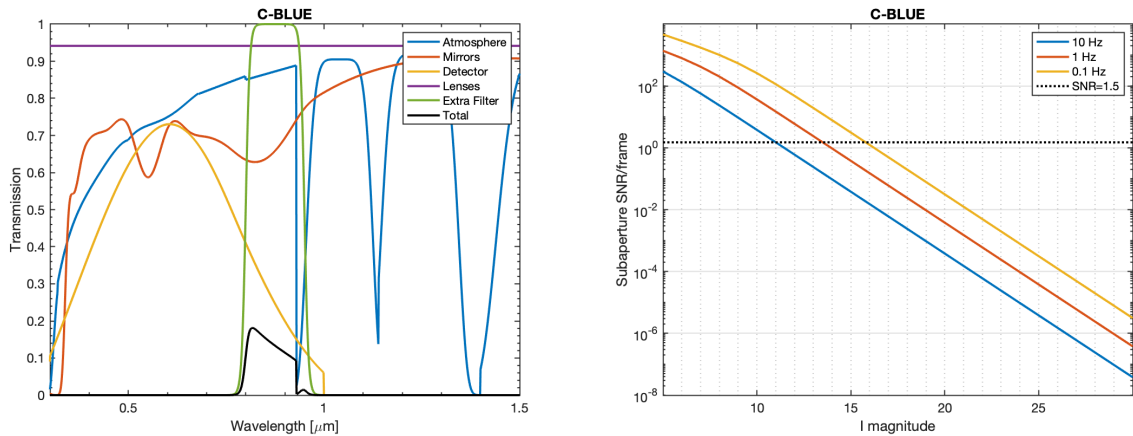


Figure 90: Left: Transmission of the system including the C-BLUE camera QE. Right: Subaperture SNR per frame for different object I magnitude. The colors represent different frame rate.

**Andor Zyla 4.2+**

For this model, we put a caution because the detector reading mode is only a rolling shutter, which can be problematic for the wavefront sensing. This have to be studied in details!

**Table 12: Zyla 4.2+ specifications**

Read noise (e-) Median	1.1
------------------------	-----

Dark current, (e-/pixel/sec)	0.019
Maximum power consumption (W)	60

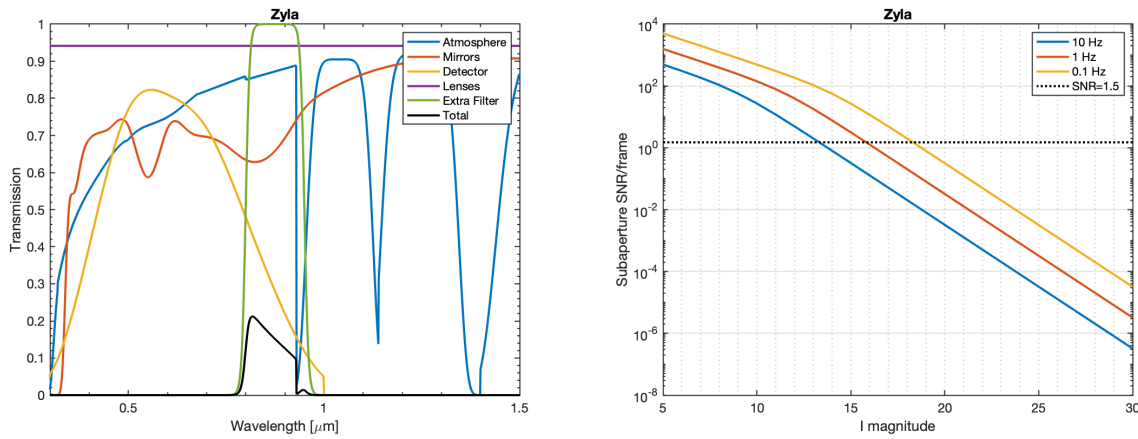


Figure 91: Left: Transmission of the system including the Zyla 4.2+ camera QE. Right: Subaperture SNR per frame for different object I magnitude. The colors represent different frame rate.

**Andor Marana 4.2**

For this model, we put a caution because the detector reading mode is only a rolling shutter, which can be problematic for the wavefront sensing. This have to be studied in details!

**Table 13: Marana 4.2 specifications**

Read noise (e-) Median	1.2
Dark current, (e-/pixel/sec)	0.1
Maximum power consumption (W)	120

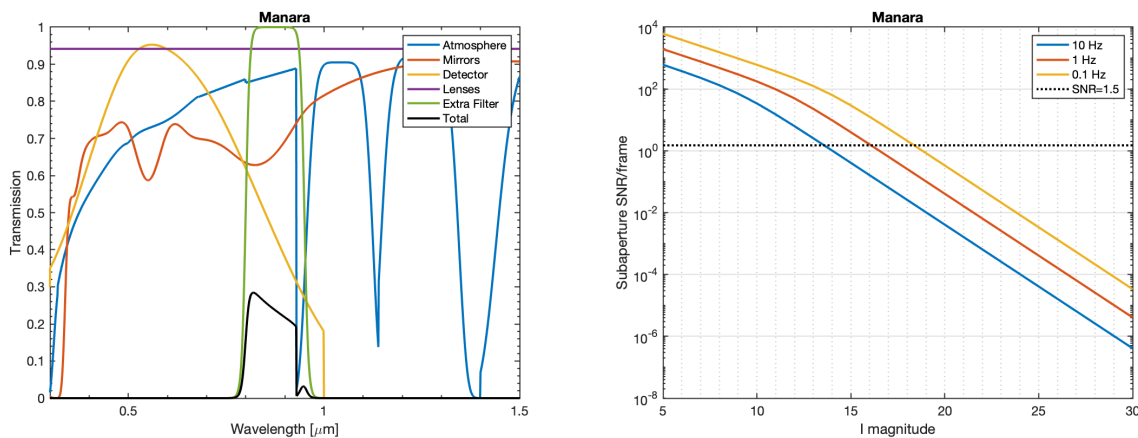


Figure 92: Left: Transmission of the system including the Marana 4.2 camera QE. Right: Subaperture SNR per frame for different object I magnitude. The colors represent different frame rate.

### D.3 Summary & Conclusion

Limiting magnitude

Camera	Magnitude limit for a SNR of 1.5 & framerate of 10Hz	Magnitude limit for a SNR of 1.5 & framerate of 1Hz	Magnitude limit for a SNR of 1.5 & framerate of 0.1Hz
Ixon 860	15.5	18	20.5
OCAM2K	15.8	18.2	21
Andor Zyla 5.5 (8x8 pixels)	12.5	14	16.5
Andor Zyla 5.5 (32x32 pixels)	8.5	11	13.5
Andor Zyla 5.5 (7 pixels)	14	16.5	19
C-Blue	11	13.5	15.9
Andor Zyla 4.2			
Marana	13.5	16	19.5

We find that the best low-power and small camera for the GIRMOS WFS is the Andor Zyla 5.5.

## Appendix E Real-time PSF estimation with GIRMOS

### Real-time PSF estimation with GIRMOS

Paolo Turri<sup>a,b</sup>, Scott C. Chapman<sup>b,a,c</sup>, Uriel Conod<sup>a,b</sup>, Kate Jackson<sup>b</sup>, Suresh Sivanandam<sup>d,e</sup>,  
and Masen Lamb<sup>e</sup>

<sup>a</sup>Department of Physics and Astronomy, University of British Columbia, 6224 Agricultural Rd,  
Vancouver, BC V6T 1Z1, Canada

<sup>b</sup>NRC - Herzberg Astronomy and Astrophysics Research Centre, 5071 W Saanich Rd, Victoria,  
BC V9E 2E7, Canada

<sup>c</sup>Department of Physics and Atmospheric Science, Dalhousie University, 6310 Coburg Rd,  
Halifax, NS B3H 4J5, Canada

<sup>d</sup>Department of Astronomy and Astrophysics, University of Toronto, 50 St George St, Toronto,  
ON M5S 3H4, Canada

<sup>e</sup>Dunlap Institute for Astronomy and Astrophysics, University of Toronto, 50 St George St,  
Toronto, ON M5S 3H4, Canada

#### ABSTRACT

GIRMOS is a multi-object adaptive optics spectrograph in the near-infrared currently being designed for the Gemini North telescope. It will allow to observe with high-quality adaptive optics correction multiple targets selected from a large field. To increase the efficiency of the nightly observations, it is important to provide a feedback in real time to operators and observers on the quality of the point-spread function, using intuitive metrics such as the full width at half maximum, the Strehl ratio and the encircled energy. In this paper we present a set of simple analytical expressions derived from other works that use the measurement of the wavefront residuals. We then compare the results to an end-to-end AO simulation of GIRMOS. We show that this approach works well with the estimation of the full width at half maximum and the Strehl ratio, while it is less successful with the encircled energy.

**Keywords:** GIRMOS, PSF

#### 1. INTRODUCTION

During this decade, telescopes like the Vera C. Rubin Observatory (formerly LSST), the Nancy Grace Roman Space Telescope (formerly WFIRST) and Euclid will survey the sky producing large amounts of data, some of which will require deep spectroscopic follow-ups. The current generation of 8-10 m ground-based telescopes can provide this capability thanks to their large apertures, which can be fully taken advantage of if the point-spread function (PSF) delivered to the spectrograph is diffraction-limited. In case of background dominated observations, the exposure time to reach a given signal-to-noise ratio (SNR) is reduced by  $t \propto D^{-4}$ , with  $D$  the telescope aperture diameter.

Adaptive optics (AO) allows for observations with large telescopes near their diffraction limit. With single-conjugate AO, the high quality correction is obtained in the direction of the guide star, quickly degrading beyond several arcseconds from it. With multi-conjugate AO, the multiple tip-tilt stars (TTS), laser guide stars (LGS) and deformable mirrors can measure and correct the turbulence over a larger field of view (FoV), although with a Strehl ratio (SR) not as high as in single-conjugate mode.

The solution to achieve high image quality on multiple targets at the same time is multi-object adaptive optics (MOAO), where separate AO channels are deployed at different position on the field of regard (FoR) of the instrument. Each path has its dedicated deformable mirror that can deliver a high-SR in their respective field of views. MOAO has been demonstrated on sky with the Raven<sup>1</sup> and CANARY<sup>2</sup> instruments. The multiplexing

P. Turri: E-mail: turri@astro.ubc.ca

Adaptive Optics Systems VII, edited by Laura Schreiber, Dirk Schmidt, Elise Vernet, Proc. of SPIE  
Vol. 11448, 1144856 · © 2020 SPIE · CCC code: 0277-786X/20/\$21 · doi: 10.1117/12.2562554

Proc. of SPIE Vol. 11448 1144856-1

Downloaded From: <https://www.spiedigitallibrary.org/conference-proceedings-of-spie> on 03 Feb 2021  
Terms of Use: <https://www.spiedigitallibrary.org/terms-of-use>

capability allows to observe multiple targets over a large FoR at the same time, making a survey with this instrument extremely efficient.

The Gemini Infrared Multi-Object Spectrograph<sup>3</sup> (GIRMOS) is a MOAO spectrograph being designed for the Gemini North telescope, fed by the Gemini North Adaptive Optics<sup>4</sup> (GNAO) system. The MOAO module<sup>5</sup> will have four deployable arms on a FoR of 2' diameter, each of them with a deformable mirror (17 actuators in diameter) delivering the corrected image to an integral field spectrograph of 30×30 spaxels. The spatial sampling can be chosen to be 25, 50 or 100 mas, corresponding to 0.75'', 1.5'', and 3'' of FoV, respectively. The near-infrared wavelength range of the spectrograph is 0.95-2.38  $\mu\text{m}$ , and the spectral resolutions can be either 3000 or 8000.

The PSF of a complex instrument like GIRMOS will have a complex shape depending on many factors, such as the seeing, the vertical distribution of the atmospheric turbulence, the telescope alt-az angle, the photon return from the laser, and the characteristics of the NGS asterism. One of the factors that can guarantee successful observations with GIRMOS is our ability to predict several basic characteristics of the PSF during the on-sky operation of the instrument. By allowing operators and observers to assess the quality of the data during the night, they would be able to judge if the instrument is working as expected, if the AO loop needs to be restarted, or if the image quality is insufficient and the exposure should be interrupted. The most common solution is to measure the profile of a bright point-like source on the focal plane. Although, this method is not easy and quick to perform with an integral-field spectrograph, since a laborious reduction of the raw data is required to reconstruct an image of the FoV. It might also not be possible to monitor the evolution of the PSF during a long exposure without interrupting it. And even probing the PSF right before or after an exposure is not feasible if there is no suitable bright star in the FoV of the scientific target.

PSF reconstruction (PSF-R) is a class of algorithms that can reproduce the long-exposure PSF of an AO observation using the telemetry of the system and the knowledge of the atmospheric turbulence.<sup>6</sup> Some of these techniques have been tested on sky, even with MOAO systems,<sup>7</sup> but they are not routinely used with scientific observations because of their complexity and unproved reliability in all conditions. PSF-R is also not suitable for monitoring the PSF in real time because of the long computational time required. Moreover, the amount of details about the profile provided by PSF-R is in excess of the few metrics that need to be monitored during operation.

The approach that we are exploring is to use simple and computationally fast analytic expressions to derive the most significant PSF metrics, such as the Strehl ratio, full width at half maximum (FWHM), and encircled energy (EE). In this paper we have tested the method summarized in [8] (hereafter G97) and [9]. We then compare the results to a set of GIRMOS PSFs generated with a simulation of the AO system, to determine if this procedure is suitable to be used on-sky with GIRMOS.

## 2. GIRMOS SIMULATION

We reproduced the GIRMOS adaptive optics loop with OOMAO,<sup>10</sup> a MATLAB program for end-to-end AO simulations. The Gemini North telescope is represented by a circular aperture with  $D = 8$  m of diameter, with a circular obstruction  $d = 1.14$  m. The sodium LGS asterism of magnitude 13 is on a square of 50'' with an additional laser at the center. The natural TTSs have magnitude 11 in R band and are positioned on an equilateral triangle inscribed in a circle of 60'' of diameter. The turbulence profile is the 7-layer median Mauna Kea profile,<sup>11</sup> with a Fried parameter of  $r_0 = 0.186$  m. More details on the GIRMOS simulations are presented by U. Connod in these proceedings.

We simulated a 5 s exposure at the zenith, at 500 Hz, with GNAO in ground layer mode. The performance was analyzed on a 11×11 grid covering a 2' field. For each position, we produced a stack of wavefront residual maps  $\Phi(u, v)$  defined on the pupil plane in radians, one for every step of the AO loop. Each map has 128×128 elements, corresponding to a resolution of 6.25 cm over the telescope aperture. In this paper we have used the H band (isophotal wavelength  $\lambda = 1.662$   $\mu\text{m}$ ) as representative of the instrument performance, since it is near the middle of the GIRMOS wavelength range (1.1-2.4  $\mu\text{m}$ ). This wavelength corresponds also to the GIRMOS requirement to deliver a EE at 100 mas in H band above 50% for all positions within the field of regard.

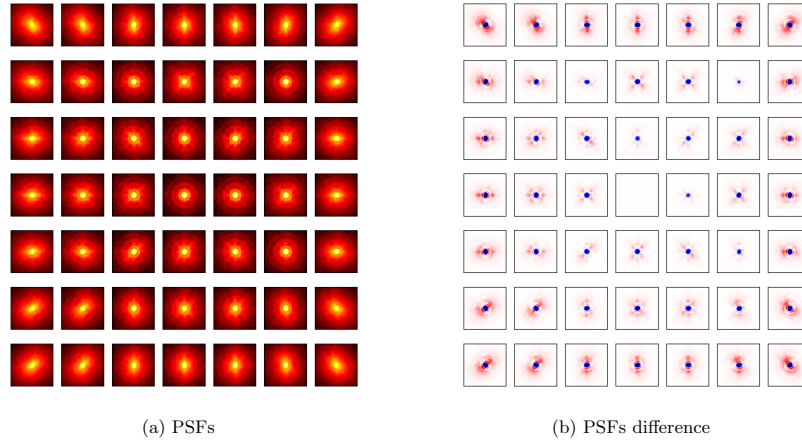


Figure 1: H band simulated grids of selected GIRMOS PSFs and their differences with the central PSF.

At every iteration of the AO loop, the instantaneous PSF produced on the image plane  $(x, y)$  is

$$PSF(x, y) = \left| \mathcal{F} \left( A(u, v) \cdot e^{-i\Phi(u, v)} \right) \right|^2, \quad (1)$$

where the wavefront amplitude  $A(u, v)$  is equal to 1 inside the pupil and 0 outside. To measure accurately the image quality, we simulated an oversampled version of the GIRMOS PSF with a pixel scale of 4 mas/px, by zero-padding the pupil plane  $(u, v)$ . All instantaneous PSFs in one direction are then stacked to form the long-exposure PSF.

As expected, the PSFs near the center of the field of regard have a high SR, indicated by the clear diffraction pattern (Figure 1a). Towards the edges of the FoR, the PSFs are radially elongated in the direction of the center of the field. This effect is more visible in the grid of the residuals respect to the central PSF (Figure 1b), and it is caused by the angular anisoplanatism.<sup>12</sup>

For each PSF on the grid, we measured several metrics as follows:

- **Full width at half maximum** – The PSF contour at half the the peak value was first fitted with an ellipse. The FWHM was then measured as the average between its major and minor axes.
- **FWHM ellipticity** – With the same ellipse used for the FWHM, the ellipticity was estimated as the ratio between the difference of the two axes and the major axis ( $e = (a - b)/a$ ).
- **FWHM angle** – It is the direction of the major axis of the FWHM ellipse.
- **Strehl ratio** – Using the same telescope aperture, the unaberrated oversampled PSF was calculated as

$$PSF_{diff}(x, y) = |\mathcal{F}(A(u, v))|^2. \quad (2)$$

The original and the diffraction-limited PSFs are normalized with the same area, therefore the SR was measured as the ratio of the two peak values.

- **Encircled energy** – It is the fraction of the PSF integrated within a given radius from the peak. We have chosen a radius of 100 mas to match the GIRMOS requirement.



- **Noise equivalent area (NEA)** – It is defined as<sup>13</sup>

$$NEA = \frac{1}{\int PSF^2(x, y) dx dy} . \quad (3)$$

The FWHM can determine the spatial resolution of an observation, particularly useful when observing crowded fields or extended objects. From Figures 2a, 2b, and 2c we see that the FWHM is homogeneous in size and shape within the GIRMOS FoR, being round and close to the diffraction limit (43 mas in H band). Only the PSFs outside the FoR deviate significantly from the diffraction profile. In this regime of good AO corrections, the FWHM is not very sensitive to changes in the AO performance.

The Strehl ratio is one of the metrics most used to describe the image quality in the design of adaptive optics instruments, since it is extremely sensitive to changes in the AO performance when the PSF is close to the diffraction limit. The SR can be used as a proxy for the SNR required to detect a source, because it indicates the quantity of signal concentrated in the peak of the profile that can rise above the noise. Although, the utility of the SR knowledge is limited, since it probes only one point of the PSF and it does not provide information on the rest of the profile. Figure 2d shows that its highest values (above 50%) are in the direction of the five LGS, where the MOAO tomographic reconstruction has less errors.

The encircled (or ensquared) energy is often a useful quantity for an observer, since it estimates the amount of light from a source falling within a region of the focal plane. This area can correspond to the one used to observe or analyze the target, such as the mask in aperture photometry, or the radius of the fitted PSF model in PSF-fitting astrometry, or the width of the slit in spectroscopy. As a consequence, the EE is a better estimator than the SR for the noise obtained in the measurement of astronomic quantities. The simulated encircled energy at 100 mas for GIRMOS (Figure 2e) has a map with a pattern similar to the SR because both correlate with the amount of light in the PSF core. All simulations inside the FoR have a EE at 100 mas above 50% in H band, satisfying the GIRMOS requirement.

The noise equivalent area represents the area of the focal plane over which the background introduces a noise equivalent to that of a point-like source dominated by it. In this case, the NEA is directly proportional to the exposure time required to reach a given SNR. Background-limited observations are common in the near-infrared, since the sky has numerous emission lines and bands, and the warm instrumentation contributes with thermal radiation. Several GIRMOS science cases<sup>3</sup> need background-limited observations of stars, like for the study of stellar populations of nearby galaxies, the dynamics in the core of Galactic globular clusters, or the extremely metal-poor stars in the Galactic Bulge. For them, the noise equivalent area is a useful metric to estimate the exposure time needed. Figure 2f shows very small values inside the FoR, which indicate a very compact PSF. These values, though, are double near the blue dashed circle than in the center of the field, indicating that a faint target observed at the edge would require double the exposure time that was calculated for a similar source in the center to reach the same SNR.

### 3. PSF ESTIMATION

To predict analytically the PSF metrics FWHM, SR and EE, we tested the method described in G97, which model the long-exposure on-axis PSF obtained from a single-conjugate adaptive optics system. This approach divides the statistical residual phase  $\sigma$  of a long exposure in two components,  $\sigma_t$  caused by the tilt jitter, and  $\sigma_{ho}$  caused by the other high-order aberrations. As a result,

$$\sigma^2 = \sigma_t^2 + \sigma_{ho}^2 . \quad (4)$$

The PSF model proposed in these works is simplified as the sum of two uni-variate Gaussian profiles. The first is the diffraction-limited sharp core convolved with the residual tilt jittering, the second is the diffuse extended halo caused by the high-order aberrations not corrected by the system. The analytic form of the profile is

$$I(\rho) = I_c \exp\left(-4 \ln(2) \left(\frac{\rho}{W_c}\right)^2\right) + I_h \exp\left(-4 \ln(2) \left(\frac{\rho}{W_h}\right)^2\right) . \quad (5)$$

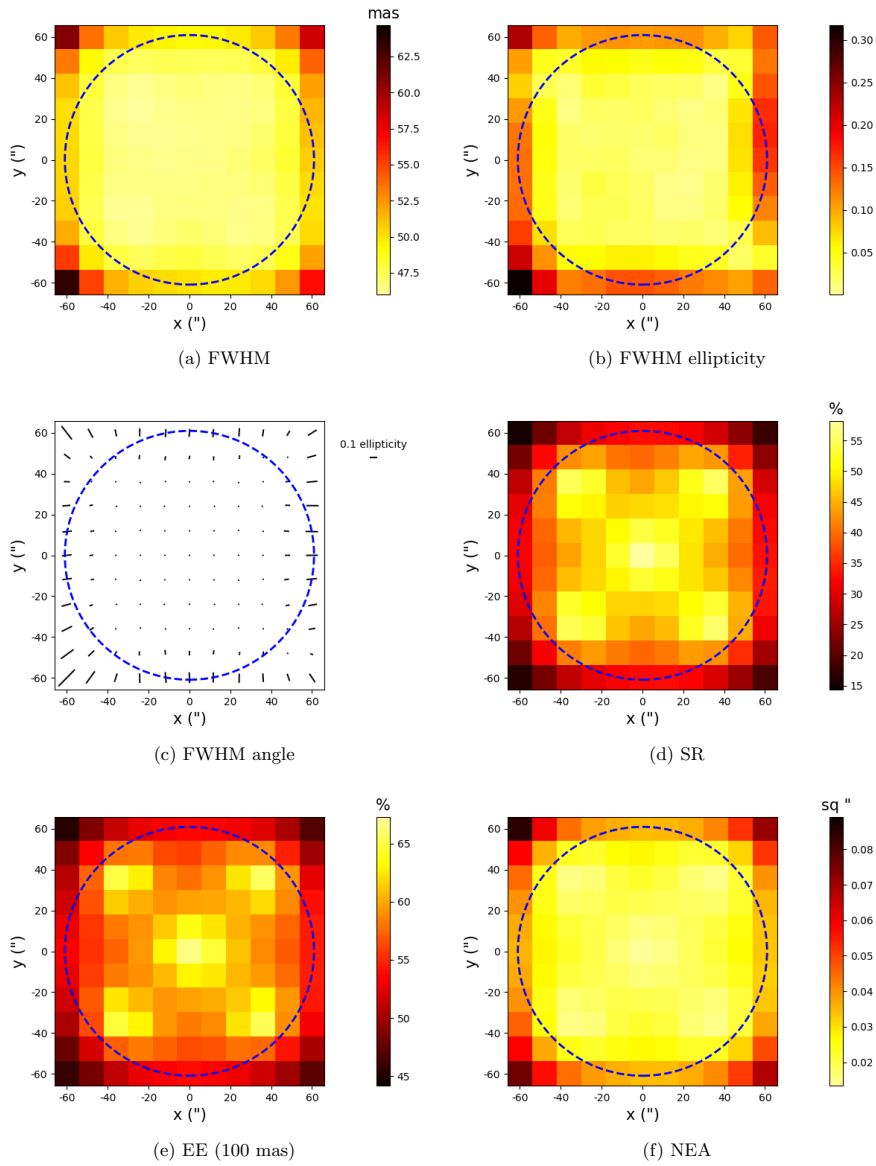


Figure 2: Grid of simulated GIRMOS PSF metrics in H band. The blue dashed circle indicates the limit of the GIRMOS 2' field of regard.

The full width at half maximum  $W$  and peak value  $I$  of the core and halo components are

$$W_c = \sqrt{\left(1.028 \frac{\lambda}{D} f_{co}\right)^2 + (2.35\sigma_t)^2}, \quad (6)$$

$$W_h = 0.98 \frac{\lambda}{r_0}, \quad (7)$$

$$I_c = \frac{\exp(-\sigma_{ho}^2)}{1 + 1.49 \left(\frac{D}{\lambda} \sigma_t\right)^2}, \quad (8)$$

$$I_h = \frac{1 - \exp(-\sigma_{ho}^2)}{1 + \left(\frac{D}{r_0}\right)^2}. \quad (9)$$

The coefficient  $f_{co} \approx 0.98$  accounts for the obstruction of the telescope aperture by the secondary mirror. In Appendix A we explain the adjustment that we made to the original equations in G97.

The profiles are normalized such that the diffraction limited PSF has a peak value  $I(0) = 1$ , therefore the Strehl ratio is  $SR = I_c + I_h$ . The encircled energy within an angle  $\alpha$  from the peak of the PSF is calculated with

$$EE(\alpha) = \frac{1}{W_c^2 I_c + W_h^2 I_h} \left[ W_c^2 I_c \left( 1 - \exp\left(-4 \ln(2) \left(\frac{\alpha}{W_c}\right)^2\right) \right) + W_h^2 I_h \left( 1 - \exp\left(-4 \ln(2) \left(\frac{\alpha}{W_h}\right)^2\right) \right) \right]. \quad (10)$$

We used the stacks of wavefront residuals simulated in Section 2 to measure  $\sigma_t$  and  $\sigma_{ho}$  for each direction of the  $11 \times 11$  grid. From those, we applied the equations of this section to estimate the PSF metrics. The results are shown in Figure 3 as a function of the distance  $r$  of the PSF from the center of the field of regard. The values calculated with the analytical expressions are compared to the measurements from the simulation (Figure 2). For the Strehl ratio, we show also the Maréchal approximation<sup>14</sup>  $SR = e^{-\sigma^2}$ .

The values of the analytic FWHM are very close to the simulated measurements within the field of regards (Figure 3a). They underestimate the real values at most by a couple of milliarcseconds, with larger errors only for the most distant and elongated PSFs (Figure 3b).

The estimated Strehl ratio has the same pattern of the simulated values (Figure 3c), with the best AO correction in the direction of the LGSs. The SR is overestimated by only 2-3% (Figure 3d), providing a closer prediction than the Maréchal approximation.

Despite both the analytic FWHM and SR being marginally better than in the simulation, the encircled energy at 100 mas is estimated to be significantly worse than the real values (Figure 3e). The two measurements are close in the center of the FoR, but they diverge at the edge, up to a value of 10% (Figure 3f).

#### 4. CONCLUSIONS

In this paper we have presented a comparison between three PSF metrics simulated for GIRMOS (FWHM, SR, and EE) and their values calculated analytically from the residual wavefront statistics. Our goal is to provide a simple yet accurate PSF estimation for nightly operations of the instrument, by updating and processing every few seconds the telemetry from the real-time controller. From Figure 3 we evaluate the FWHM and SR estimates to be very close to the correct values, while the EE has considerable errors, possibly caused by the substantial deviation of the PSF from the simplistic model of a double Gaussian profile.

In light of these results, we consider this approach promising. But before settling for this solution there are several more tests that we will perform:

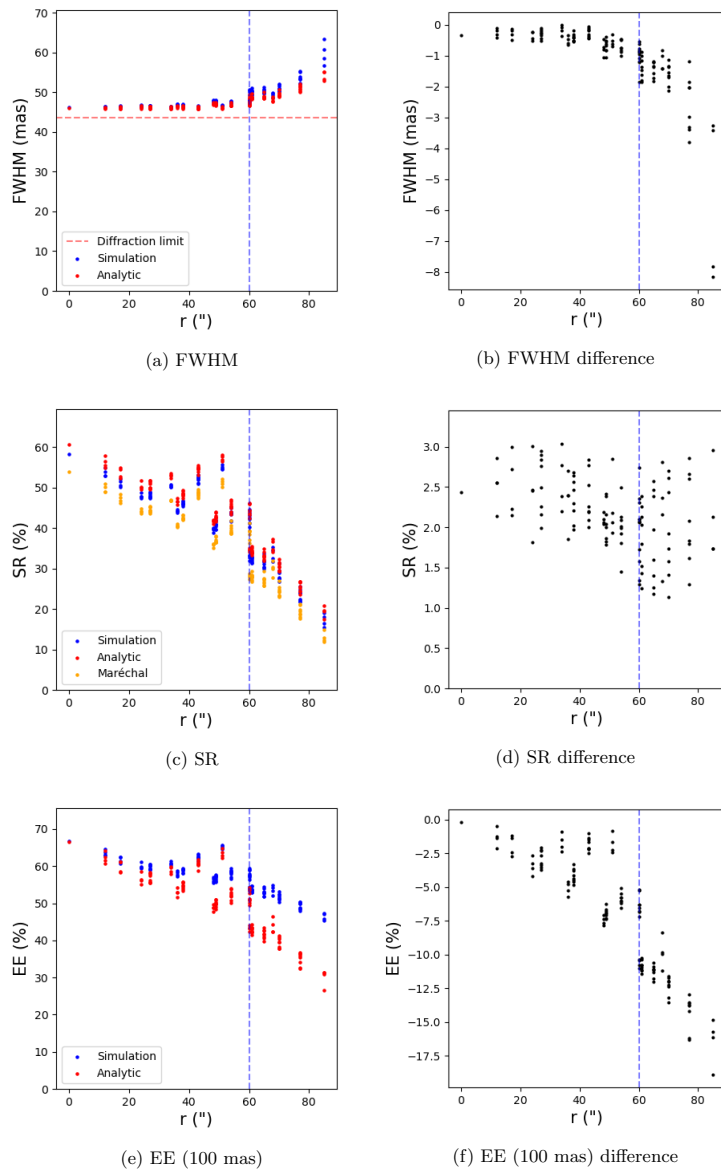


Figure 3: Simulated and analytic PSF metrics in H band, plotted as a function of their distance from the center of the field of regard. (*Right column*) Difference between the analytic and simulated values. The blue dashed vertical line indicates the limit of the GIRMOS 2' field of regard.

- Explore if the EE analytical expression could work by the addition of a few parameters to account in all conditions for the deviation of the model profile from the real.
- Probe if the equations hold in a larger parameter space, using different wavelengths, Fried parameters, turbulence distributions, asterisms, and zenith angles.
- Simulate the use of the tomographically reconstructed wavefronts produced by the real-time controller instead of the the true high-resolution wavefront residuals, which do not include the wavefront sensors' fitting and aliasing errors.<sup>15</sup>

### APPENDIX A. CHANGES TO THE EQUATIONS

Several equations presented in Section 3 have been changed respect to their form in G97, or we have redefined some of their variables to adapt them to our need.

- Equation 6 was originally

$$W_c = \sqrt{\left(1.22 \frac{\lambda}{D}\right)^2 + (2.7\sigma_t)^2} . \quad (11)$$

It should describe the FWHM of the core Gaussian as the sum in quadrature of the diffraction-limited profile of a circular aperture and the dispersion caused by the tilt jittering.

The FWHM of the Airy disk is actually  $1.028\lambda/D$ , while  $1.22\lambda/D$  is the radius of the first zero of the profile, often used as a measurement of the diffraction-limited angular resolution (Rayleigh criterion<sup>16</sup>). We have also added the factor  $f_{co}$  to account for the reduction in size of the FWHM caused by the telescope secondary mirror. We have calculated its value from the profile<sup>17</sup>

$$I(\rho) = \frac{1}{(1-\epsilon^2)^2} \left[ \frac{2J_1(\rho)}{\rho} - \frac{2\epsilon J_1(\epsilon\rho)}{\rho} \right]^2 , \quad (12)$$

where  $J_1$  is the Bessel function of the first kind of order one, and  $\epsilon = d/D = 1.14/8 = 0.1425$  is the relative central obscuration of the Gemini telescope.

The tilt jittering component of the core profile is derived in Equation 3 of [18] using the assumption that tip and tilt have a random Gaussian distribution, therefore with a FWHM equal to  $2\sqrt{2\ln(2)}\sigma_t \approx 2.35\sigma_t$ , instead of  $2.7\sigma_t$ . We have also modified the meaning of the  $\sigma_t$  variable, initially indicating the standard deviation of the combined tip-tilt vector. The two components are actually correlated, particularly at the edge of the FoR, where they produce the elongation of the PSF (Figure 1a). We have instead calculated the covariance matrix of the tip-tilt measurements and used its eigenvalues as the variances  $\sigma_{t,1}^2$  and  $\sigma_{t,2}^2$ , parallel and perpendicular to the elongation, from which

$$\sigma_t = \sqrt{\sigma_{t,1}^2 + \sigma_{t,2}^2} . \quad (13)$$

- Equation 7 is reported in G97 as

$$W_h = 1.22 \frac{\lambda}{r_0} . \quad (14)$$

As for Equation 11, the angular resolution (coefficient 1.22) was incorrectly used instead of the FWHM, which is 0.98 for a Kolmogorov turbulence.<sup>19</sup>

- The original version of Equation 8 was

$$I_c = \frac{\exp(-\sigma_{ho}^2)}{1 + 4.94 \left(\frac{D}{\lambda}\sigma_t\right)^2} . \quad (15)$$

From Equation 15 in [20], the coefficient for the variance of the tilt error should be  $1/0.82^2 \approx 1.49$  instead of 4.94.

## ACKNOWLEDGMENTS

We thank the National Research Council, the Gemini Observatory, and the the Dunlap Institute for Astronomy and Astrophysics for their support in this project. This project is funded by the Canada Foundation for Innovation, Ontario Research Fund, British Columbia Knowledge Development Fund, Fonds de Recherche du Québec, and Nova Scotia Research and Innovation Trust.

## REFERENCES

- [1] Lardière, O., Andersen, D., Blain, C., Bradley, C., Gamroth, D., Jackson, K., Lach, P., Nash, R., Venn, K., Véran, J.-P., Correia, C., Oya, S., Hayano, Y., Terada, H., Ono, Y., and Akiyama, M., “Multi-object adaptive optics on-sky results with Raven,” in [*Adaptive Optics Systems IV*], Marchetti, E., Close, L. M., and Véran, J.-P., eds., *Proc. SPIE* **9148**, 91481G (2014).
- [2] Gendron, E., Vidal, F., Brangier, M., Morris, T., Hubert, Z., Basden, A., Rousset, G., Myers, R., Chemla, F., Longmore, A., Butterley, T., Dipper, N., Dunlop, C., Geng, D., Gratadour, D., Henry, D., Laporte, P., Looker, N., Perret, D., Sevin, A., Talbot, G., and Younger, E., “MOAO first on-sky demonstration with CANARY,” *A&A* **529**, L2 (2011).
- [3] Sivanandam, S., Chapman, S., Simard, L., Hickson, P., Venn, K., Thibault, S., Sawicki, M., Muzzin, A., Erickson, D., Abraham, R., Akiyama, M., Andersen, D., Bradley, C., Carlberg, R., Chen, S., Correia, C., Davidge, T., Ellison, S., El-Sankary, K., Fahlman, G., Lamb, M., Lardière, O., Lemoine-Busserolle, M., Moon, D.-S., Murray, N., Peck, A., Shafai, C., Sivo, G., Véran, J.-P., and Yee, H., “Gemini Infrared Multi-Object Spectrograph: instrument overview,” in [*Ground-based and Airborne Instrumentation for Astronomy VII*], Evans, C. J., Simard, L., and Takami, H., eds., *Proc. SPIE* **10702**, 107021J (2018).
- [4] Sivo, G., Palmer, D., Scharwächter, J., Andersen, M., Provost, N., Marin, E., van Dam, M., Chinn, B., Chirre, E., Cavedoni, C., Schneider, T., Kang, S., Hirst, P., Rambold, W., Ebberts, A., Gigoux, P., Catala, L., Hayward, T., Blakeslee, J., Roe, H., Lotz, J., Kleinman, S., Sivanandam, S., Krause, A., Ammons, M., Trujillo, C., Packham, C., Marchis, F., Christou, J., Jee, J., Bally, J., Pierce, M., Puzia, T., Turri, P., Kim, H., Schwamb, M., Dupuy, T., Diaz, R., Carrasco, R., Neichel, B., Correia, C., Steinbring, E., Rigaut, F., Véran, J.-P., Chun, M., Lamb, M., Chapman, S., Esposito, S., and Fusco, T., “GNAO: an MCAO facility for Gemini North,” in [*Advances in Optical Astronomical Instrumentation*], Ellis, S. and d’Orgeville, C., eds., *Proc. SPIE* **11203**, 112030N (2020).
- [5] Chapman, S. C., Sivanadam, S., Andersen, D., Bradley, C., Correia, C., Lamb, M., Lardière, O., Ross, C., Sivo, G., and Véran, J.-P., “The multi-object adaptive optics system for the GIRMOS spectrograph on Gemini-South,” in [*Adaptive Optics Systems VI*], Close, L. M., Schreiber, L., and Schmidt, D., eds., *Proc. SPIE* **10703**, 107031K (2018).
- [6] Véran, J.-P., Rigaut, F. J., Maitre, H., and Rouan, D., “Estimation of the adaptive optics long-exposure point-spread function using control loop data,” *JOSAA* **14**, 3057 (1997).
- [7] Martin, O. A., Correia, C. M., Gendron, E., Rousset, G., Gratadour, D., Vidal, F., Morris, T. J., Basden, A. G., Myers, R. M., Neichel, B., and Fusco, T., “PSF reconstruction validated using on-sky CANARY data in MOAO mode,” in [*Adaptive Optics Systems V*], Marchetti, E., Close, L. M., and Véran, J.-P., eds., *Proc. SPIE* **99091Q**, 9909 (2016).
- [8] Ge, J., Angel, J. R. P., Sandler, D. G., Shelton, J. C., McCarthy, D. W., and Burge, J. H., “Adaptive optics spectroscopy: preliminary theoretical results,” in [*Adaptive Optics and Applications*], Tyson, R. K. and Q.Fugate, R., eds., *Proc. SPIE* **3126**, 343 (1997).
- [9] Parenti, R. R., “Adaptive optics for astronomy,” *LLabJ* **5**, 93 (1992).
- [10] Conan, R. and Correia, C., “Object-oriented Matlab adaptive optics toolbox,” in [*Adaptive Optics Systems IV*], Marchetti, E., Close, L. M., and Véran, J.-P., eds., *Proc. SPIE* **9148**, 91486C (2014).
- [11] Mieda, E., Véran, J.-P., Rosensteiner, M., Turri, P., Andersen, D., Herriot, G., Lardière, O., and Spanò, P., “Multiconjugate adaptive optics simulator for the Thirty Meter Telescope: design, implementation, and results,” *JATIS* **4**, 049002 (2018).
- [12] Fried, D. L., “Anisoplanatism in adaptive optics,” *JOSA* **72**, 52 (1982).
- [13] King, I. R., “Accuracy of measurement of star images on a pixel array,” *PASP* **95**, 163 (1983).

- 
- [14] Maréchal, A., “Étude des effets combinés de la diffraction et des aberrations géométriques sur l’image d’un point lumineux,” *Rev. Opt. Theor. Instrum.* **26**, 257 (1947).
  - [15] Ellerbroek, B. L., “Linear systems modeling of adaptive optics in the spatial-frequency domain,” *JOSAA* **22**, 310 (2005).
  - [16] Lord Rayleigh, “Investigations in optics, with special reference to the spectroscope,” *PMag* **5**, 261 (1879).
  - [17] Born, M. and Wolf, E., [*Principles of optics*], Cambridge University Press, University Printing House, Cambridge CB2 8BS, United Kingdom, 60th anniversary ed. (2019).
  - [18] Olivier, S. S., Max, C. E., Gavel, D. T., and Brase, J. M., “Tip-tilt compensation: resolution limits for ground-based telescopes using laser guide star adaptive optics,” *ApJ* **407**, 428 (1993).
  - [19] Kolb, J., “Turbulence characterization at the Nasmyth focal plane of the VLT Melipal,” in [*Adaptive Optics Systems*], Hubin, N., Max, C. E., and Wizinowich, P. L., eds., *Proc. SPIE* **7015**, 70154O (2008).
  - [20] Gavel, D. T. and Olivier, S. S., “Simulation and analysis of laser guide star adaptive optics systems for the eight to ten meter class telescopes,” in [*Adaptive Optics in Astronomy*], Ealey, M. A. and Merkle, F., eds., *Proc. SPIE* **2201**, 295 (1994).

## **Appendix F      RTC Design**

The details of the RTC design documents can be find in [AD-08].